DEMONSTRATION AND INTEGRATION OF SYSTEMS FOR FIRE REMOTE SENSING, GROUND-BASED FIRE MEASUREMENT, AND FIRE MODELING

PROJECT FINAL REPORT

Study #JFSP-03-S-01

Principal investigators:

COLIN C. HARDY – USDA Forest Service, Rocky Mountain Research Station
Missoula Fire Science Laboratory, 5775 US Highway 10 West, Missoula, MT 59808
Office: (406) 329 4978; Fax: (406) 329-4825; Email chardy01@fs.fed.us

PHILIP J. RIGGAN – USDA Forest Service, Pacific Southwest Research Station

Contributors:

BRET BUTLER, PATRICK FREEBORN, SHARON HOOD, DAN JIMENEZ,
ROBERT KREMENS, LEE MACHOLZ, BRYCE NORDGREN, LLOYD P. QUEEN,

Rocky Mountain Research Station
Missoula Fire Sciences Laboratory

Pacific Southwest Research Station
Riverside Forest Fire Laboratory

University of Montana
National Center for Landscape Fire Analysis

Rochester Institute of Technology
Center for Imaging Science

CONTENTS

EXECUTIVE SUMMARY

This JFSP study emphasizes the development and evaluation of new systems for *in situ* and remote sensing-based measurements of fire that can provide direct, real- or near-realtime observations of many of the thermodynamic processes associated with fire. The charter proposal authorized by JFSP for this study comprised a consolidation of two separate, but complementary preliminary proposals: the first (Hardy et al.), was submitted from the Missoula Fire Sciences Laboratory, and addressed the development and deployment of oblique thermal infrared cameras and in situ instrumentation; the second (Riggan et al.) was specific to airborne remote sensing in support of operational fire management. Significant and complementary linkages with two other JFSP studies were addressed in the 2003 study plan: Finney and others (*Modeling surface winds in complex terrain for wildland fire incident support*); and Morgan and others (*Assessing the causes, consequences and spatial variability of burn severity: a rapid response proposal*). The combined study was initiated in 2003 as a one-year "proof-of-concept" effort. Following successes in 2003, an amended study agreement was approved to "provide the opportunity for two additional full deployments of the Rapid Response Team." This amended study was subsequently extended through December, 2006 to facilitate completion and analysis of data several more deployments accomplished in 2006.

The study was implemented in the JFSP's "Rapid Response" model, whereby personnel and resources were dispatched to ongoing wildland fire incidents. General measurement categories included space-based remote sensing, airborne remote sensing, surface-based oblique radiometry, *in situ* remote sensing, and plot-based site characterization. Following mobilization to an incident and identification of acceptable study site(s) within the incident, the team proceeded with pre-burn deployment of *in situ* instrumentation, coincident vegetation and site characterization at the study site, installation of offsite (surface-based) thermal infrared (TIR) systems, and preparation of logistics to support air operations for airborne data collections. Following burnover of the study site, post-burn measurements of fuel, vegetation, and site characteristics were made. In addition to *in situ* instrumentation, three scales of thermal infrared radiometric measurements were made for the period of time in which fire was present on the site: TIR sensor systems were installed at a nearby viewpoint; an aircraft-borne remote sensing system was utilized; and, when available, data were acquired from the space-borne MODIS sensor. A comprehensive spatial geodatabase was developed for this study, into which all post-processed instrumentation data as well as plot-based site characterization data, documentation, photographs, and imagery were uploaded to the Geodatabase for subsequent access and analysis by the researchers.

Although the agreements for this study proposed mobilization to only four incidents, the Rapid Response Team mobilized to seven individual wildland fire incidents during the period 2003 through 2006. These incidents included one prescribed burn in Central Montana, two wildland fires and one wildland fire use incident in western Montana, a wildland fire in eastern Idaho, a wildland fire in north-central Washington, and a wildland fire use incident near the North Rim, Grand Canyon, Arizona. Ten instrument deployments were achieved at these seven incidents; five of these ten deployments are presented in this report. The only mobilization for which airborne remote sensing data

are presented in this report was the Cooney Ridge incident—the Pacific Southwest Research Station's FireMapper system successfully acquired and processed time-series thermal infrared imagery for the full extent of this deployment. A more extensive report on additional FireMapper acquisitions is provided by Co-PI Riggan under separate cover.

New technologies and deployment protocols resulting directly from this study include: highly-portable, multi-sensor Autonomous Environmental Sentry systems; third-generation *in situ* Fire Behavior Flux sampling packages capable of remote triggering; fire-proof video enclosures linked with the flux packages for remote triggering; prototyped wireless video acquisition and broadcasting systems for *in situ* video; procedures for installation, acquisition, georegistration, and analysis of data from paired, oblique-looking thermal infrared camera systems; exploration of MODIS fire detection and buffering algorithms; protocols for each one of a three-tiered (three hierarchical levels-of-effort) rapid response characterization of pre- and post-burn vegetation, fuels, and site attributes; a comprehensive geodatabase architecture, operational system, and development protocol (now fully populated with all available data from the Cooney Ridge (one deployment) and Tripod Complex (two deployments) incidents).

Comparisons between total and radiant heat flux, and between hemispherical and narrow angle acceptance angles, were conducted with the *in situ* measurements. The potential for estimating first-order fire effects was examined by comparing the total radiant energy measured over the duration of the fire to the total fuel consumed obtained through pre- and post-burn fuel surveys. Finally, the advantages and disadvantages of each measurement method are addressed with recommendations for proper field applications in the future.

A critical aspect of any Rapid Response field campaign is the operational and logistical model under which field crews are mobilized. For this study, we developed a comprehensive Field Operations Plan, addressing crew qualifications, Job Hazard Analyses, air operations, safety and medical plans, transportation, and a command-and control structure enabling the Team to safely and effectively embed within both the operational and the cultural environment of a wildland fire incident.

The primary customer for this "demonstration and integration" study is the cohort of fire behavior and fire effects modelers who are anxious for better quantification of the energy and heat flux from fires. Resource managers will then benefit from this research after models are updated and new models are developed on the basis of this state-of-science study.

INTRODUCTION

JUSTIFICATION AND IMPERATIVE FOR THIS WORK

This JFSP study emphasizes the development and evaluation of new systems for *in situ* and remote sensing-based measurements of fire that can provide direct, real- or near-realtime observations of many of the thermodynamic processes associated with fire. These can then be linked to observed fire effects, resulting in one-to-one linkages with which models both for fire behavior and fire effects can be developed. When assessments of the bio-geo-chemical effects of a wildland fire are made—either during or after an incident—linkages to the characteristics of the fire that caused the effects are made using anecdotal evidence, post-fire reconstruction of the fire event, and inference from adjacent unburned areas. Often, these inferences become circular; that is, fire effects models are developed using inferences of fire behavior based on observations of the effects. This research and development is important because deliverables include specifications for new instruments, methods, and protocols for measurements of fire processes. In addition, this study provides validation and quantification of the implications of scaling between various spatial hierarchies of instrumentation—from in situ, to oblique surface observations, to aircraft platforms, and to satellite systems.

In addition to development of new instrumentation, measurement protocols, and analytical methods, a spatial database architecture (geodatabase) has been developed and implemented to accommodate all of the extremely diverse data elements from the study—point data (plot-based), line data (transect sampling), polygons (area-based sample data), gridded spatial data (raster imagery), photographs, videos, and metadata. Many of these data elements are not only multi-spatial, but are also multi-temporal, expressed as time series data. The Rapid Response Geodatabase is a model for other interdisciplinary studies to exploit, where multiple investigators need to organize, analyze, and share diverse data elements in a common (shared) database environment.

This work applies to any wildland fire situation in the world. The instrumentation, methods, field protocols, and analytical deliverables are independent of biomes, culture, or geography. Ultimately, the energy from fires drives most, if not all, fire effects modeling and predictive systems; e.g. for air resources (plume rise, emissions source strength), soils (heat pulse/flux), stem and bole damage to living vegetation (convective and radiative heating). The primary customer for this "demonstration and integration" study is the cohort of fire behavior and fire effects modelers who are anxious for better quantification of the energy and heat flux from fires. Resource managers will then benefit from this research after new models based on the research are developed. Practitioners will be able to relate measured energy fluxes with expected impacts on various resources, and will be able to develop both fire management and rehabilitation strategies and tactics as the fire develops and burns, rather than after the fire.

STUDY OBJECTIVES

- Conduct proof-of-concept research to compare state-of-science space-borne, airborne, and ground-based fire measurement systems.

- Begin evaluation of two fire-behavior simulation models with these data.
- Test approaches to incorporating improved weather data in these models.
- Test the utility of the airborne remote sensing for incident management.
- Investigate the development of a common database architecture.

GENERAL STUDY APPROACH

This study was implemented in the JFSP's "Rapid Response" model, whereby personnel and resources were dispatched to ongoing wildland fire incidents. The rapid response team then worked with the Incident Management Team to select unburned candidate study sites within the incident and with the potential for subsequent burnover or possible manual ignition. With one or more candidate study sites identified, the team proceeded with pre-burn deployment of *in situ* instrumentation, coincident vegetation and site characterization at the study site, installation of offsite (surface-based) thermal infrared systems, and preparation of logistics to support air operations for airborne data collections. Following burnover of the study site, post-burn measurements of fuel, vegetation, and site characteristics were made.

All post-processed instrumentation data as well as plot-based site characterization data, documentation, photographs, and imagery were uploaded to the Geodatabase for subsequent access and analysis by the researchers.

In addition to *in situ* instrumentation, three scales of thermal infrared radiometric measurements were made for the period of time in which fire was present on the site: TIR sensor systems were installed at a nearby viewpoint; an aircraft-borne remote sensing system was utilized; and, when available, data were acquired from the space-borne MODIS sensor.

The hierarchical-scale design of this study facilitated intercomparisons of methods and results between instrumentation approaches, and also provided quasi-redundancy in data collections for situations where not all systems could be simultaneously installed or operated.

In many regards, the methods and protocols developed for this project are as important and relevant as are the results—a primary focus of the study was "demonstration and integration." In this report, we first present the methods of measurement and observation for each of six respective sub-teams (described below). Results are then presented for each of the individual sub-teams; we then present cross-team comparisons and integration of results.

STUDY COMPONENTS AND SUB-TEAMS

General measurement categories included space-based remote sensing, airborne remote sensing, surface-based oblique radiometry, *in situ* remote sensing, and plot-based site characterization. Therefore, operations were partitioned into five sub-teams, each with a Team Leader and dedicated personnel. A sixth, laboratory-based team was responsible for design and implementation of the geodatabase. These six, under the logistical leadership of an operations command team, are presented in Table 1.

Table 1. Rapid Response sub-teams and team leaders.

Rapid Response Sub-Team	Team Leader/Affiliation*
Operations & Command	Colin Hardy (FiSL)
1. Site Characterization	Sharon Hood (FiSL)
2. In Situ Instrumentation	Bret Butler (FiSL), Robert Kremens (RIT)
3. Oblique Thermal IR	Patrick Freeborn (FiSL)
4. Airborne Remote Sensing	Phil Riggan (PSW)
5. MODIS Satellite Sensor	Bryce Nordgren (FiSL)
6. GeoDatabase	Lee Macholz (NCLFA)

* **FiSL**—Missoula Fire Sciences Laboratory, Rocky Mountain Research Station, USDA FS;
RIT—Rochester Institute of Technology, Rochester, NY;
PSW—Riverside Fire Laboratory, Pacific Southwest Research Station, USDA FS;
NCLFA—National Center for Landscape Fire Analysis, University of Montana

The Operations and Command sub-team for this Rapid Response Project has overall responsibility and authority for all operational aspects of the field campaigns. In the "Command and Staff" paradigm, the sub-teams listed above are considered "staff" positions. The Command Team is comprised of the following positions:

Operations Chief—Lead scientist responsible for overall field campaign; typically the Principal Investigator for this study.
Primary Assignment: Colin C. Hardy (FiSL)

Logistics Coordinator—Prepares daily shift plan; has responsibility for coordination of field activities and communications during field activities.
Primary Assignment: LLoyd P. Queen (NCLFA)

IMT Liaison and Communications—The Rapid Response Team provides, when possible, a Team member qualified as single resource or higher as liaison dedicated to the incident Management Team. This individual is selected on a per incident basis from among the highest qualified members of the Team.
Primary Assignment: Edward Mathews (FiSL)

The IMT Liaison functions as an ex-officio member of the IMT by.:

- Communicating with IMT prior to deployment to incident
- Reporting to IMT upon arrival at incident
- Providing rosters/manifest of Team members deployed at the incident and each individual's function
- Attending daily briefings
- Managing communications with and among Team members and the IMT

The IMT liaison has full authority for dispatch, management, and stand-down orders for the Team. The liaison works with the Rapid Response sub-team leaders to ensure compliance with IMT guidelines, policies, and orders.

Sub-teams #1, #2, and #3, shown in Table 1, are field-based and typically operate within the uncontrolled perimeter of wildland fire incidents. Responsibilities and functions for leaders of the field-based sub-teams include the following:

> **Team Leader: Site Characterization**—Supervises and directs all field activities related to pre- and post-burn on-site vegetation and fuels inventory. Team is comprised of Team Leader and 1-3 crew persons.
> Primary Assignment: Sharon Hood (FiSL)
>
> **Team Leader: *In Situ* Instrumentation**— Supervises and directs all field activities related to installation, operation, and retrieval of all on-site instrumentation.
> Primary Assignment: Bret Butler (FiSL)
>
> **Team Leader: Oblique Thermal IR**— Supervises and directs all field activities related to installation, operation, and retrieval of two thermal infrared radiometers, including power management, QA/QC, and on-site registration of data.
> Primary Assignment: Patrick Freeborn (FiSL)

MEASUREMENTS AND OBSERVATIONS

TEAM #1—SITE CHARACTERIZATION (VEG AND FUELS)—SHARON HOOD

The site characterization and fuels team is responsible for collecting pre- and post-fire site, fuels, vegetation data as well as during-fire weather data. The fuels and vegetation data allow the site to be matched to an existing fire behavior fuel model or, alternatively, provide input to creation of a customized fuel model or fuelbed description. These data and the associated fuel model are used to predict expected fire behavior and effects based on weather and fuel moistures. We can use the collected data to compare predicted versus actual fire behavior and effects to validate the current fire behavior and effects models.

When the specified conditions for selecting a sample site and plot location are met (discussed on p.26 in “Study Site and TIR Camera Vantage Point Selection”), we establish a 0.10-acre circular plot coincident with the centroid of *in situ* instrument deployment (Figure 1). At this plot, the Fuels Team begins sampling and the other teams set up fire behavior sensor packages and weather stations.

The Fuels Team uses a hierarchical sampling approach—based on available time before the area is expected to burn—to determine the feasible intensity of sampling and the number of plots within the sample area. The appropriate intensity for sampling is classified and described by three “sampling levels:”

Level I: Minimal— Accomplished in less than thirty minutes, by 1-2 people;

Level II: Nominal— Accomplished in 30-60 minutes, by 2-3 people; and

Level III: Extended— Greater than 60 minutes are required, with 3-4 people.

The Fuels Team consists of 1-4 people, depending on sampling level. If significant time or logistical constraints exist, Level I sampling is utilized and only one person is required. Level II and III require a 2-4 person team. At Levels II and III, one person measures fuels and 2-3 people complete the plot and tree measurements. Fuel moisture sampling is completed by all members of the team before leaving the plot and moving to a safety zone. In the cases of sampling levels II and III, additional plots may be established around the main instrument plot if time allows. We follow FIREMON sampling procedures as closely as possible for all data collection (Lutes et al. 2006, http://www.fire.org/index.php?option=content&task=section&id=5&Itemid=42). We also use FIREMON to archive the Fuels Team sample data, estimate fuel loadings, and summarize tree plot data.

Level I Plot-Sampling Details

Level I Pre-fire

Site characterization.— We use the FIREMON "plot description" data form (PD) to characterize the plot. For this minimum level, plot center is monumented with rebar and a numbered tag. We record plot location (UTM), slope, slope position, aspect, and dominant understory species. Four plot pictures are taken in the cardinal directions, approximately 10 feet away from plot center, facing plot center. We sample trees with a variable radius plot using a 20 basal area factor prism. Trees are recorded as encountered starting from due north and moving clockwise. Tree species and status are recorded for each tree. Layout of the sampling plot is illustrated in Figure 1.

Fuel loading estimates.— Two 75 foot planar intercept fuel transects are established, beginning at plot center and radiating out north and east (Figure 1)(Brown et al. 1982). Each transect is monumented by placing rebar at the end and middle to aid in transect relocation. Fuels are sampled along each transect using the FIREMON "fuel loading" form (FL) (Figure 2). In addition to measuring dead and down woody fuels, we measure duff and litter depths and average fuel bed depth at two locations for each transect. Lastly, we collect three fuel moisture samples for each of the following components: 1, 10, and 100 hour fuel classes, duff, litter, and live fuels (Figure 3). These samples are weighed within 12 hours and then taken to the Fire Sciences Lab for drying and weighing to calculate oven-dry fuel moisture content.

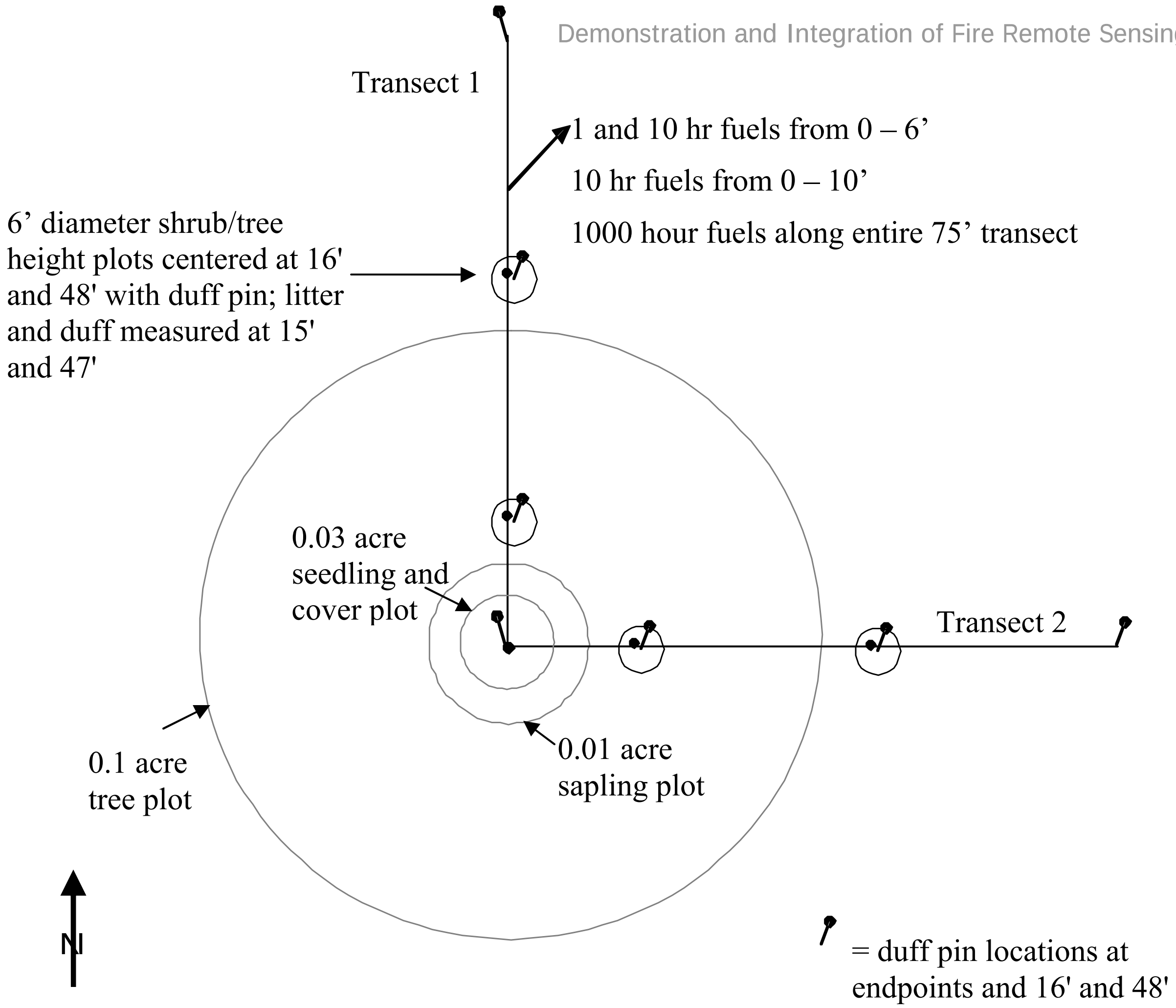

Figure 1. Layout of site characterization sampling plot, with 0.03-acre seedling and cover plot, 0.01-acre sampling plot, 0.1-acre tree plot, 6' diameter shrub/tree height plots, duff reduction pin locations, and two litter/duff and woody fuel inventory transects.

<u>IMT weather intelligence</u>.— Standard weather intelligence acquired by the Incident Management Team (IMT) is recorded. The Fuels Team also records on-site weather conditions using a sling psychrometer and wind gauge (Figure 3).

Figure 2. Establishing fuel transects.

Figure 3. Taking weather observations with sling psychrometer and measuring fuels along a transect.

Level I Post-fire

Site characterization.— Post-fire sampling is conducted as soon as we can safely re-enter the burned area. This can occur from 2 days to several months post-fire. Once the plot is located, we take post-burn pictures using the same techniques as described in the pre-fire section, using care to match post-fire pictures with pre-fire pictures as closely as possible (Figure 4). For the trees recorded during pre-fire sampling, we measure status, diameter at breast height (DBH), tree height, pre-fire crown base height, post-fire crown base height, and percent crown volume scorched.

Figure 4. Photopoint showing plot before fire (left photo) and after fire (right photo) at the Dragon WFU Incident, deployment #2.

Fuel loading estimates.— The two fuel transects are relocated and are re-sampled using the same techniques described in the pre-fire section.

Level II Plot-Sampling Details

Level II Pre-fire

Site characterization.— The plot description and photo-point sampling is the same as Level I. For the Level II tree plot we follow the tree plot description in FIREMON. All trees above a breakpoint diameter are sampled within a 0.10 acre fixed area plot, beginning at due north and continuing clockwise. Breakpoint diameter is dependent on the ecosystem, but is usually 5.0 inches. For each tree, status, species, and DBH are recorded (Figure 5). Tree height and crown base height are measured on approximately 2-3 trees per quadrant. Saplings are recorded by species, status, and diameter class on a 0.01 microplot using the same plot center as the 0.1 acre macroplot. Seedlings are counted by species, status, and height class on the microplot. We then estimate percent cover and average height by life form following the "species composition" (SC) description in FIREMON on the microplot.

Figure 5. Measuring DBH on a tree plot. Orange and white plot pole indicates plot center.

Fuel loading estimates.— Fuel loading measurements and fuel moisture sample collection are the same as described for the Level I sampling. In addition, duff spikes are installed at two points along each transect, flush with the top of the litter layer. These are used to determine fire-caused reduction in duff depths.

IMT weather intelligence.— Same as Level I, but on-site weather is recorded every 30 minutes.

Level II Post-fire

Site characterization.— Post-fire plot photos are sampled the same as described for Level I. For the tree plot, we measure status, post-fire crown base height, and percent crown volume scorched on all trees. We also measure tree height and pre-fire crown base height on the trees not measured pre-fire. The post-fire sapling, seedling, and cover microplot sampling is redone using the same protocols described for Level II pre-fire sampling.

Fuel loading estimates.— The two fuel transects are relocated and are re-sampled using the same techniques described in the Level I pre-fire section. The duff spikes are relocated and the length of the spike exposed and the length from the top of the duff or litter to mineral soil are recorded for calculating forest floor consumption (Figure 6).

Figure 6. Exposed post-fire duff spike along a fuel transect. This spike was level with the top of the litter layer prior to burning. The length of exposed spike indicates the amount (depth) of duff and litter consumed during the fire.

Level III Plot-Sampling Details

Level III Pre-fire

Site characterization.— Same as Level II, except that tree height and crown base height are measured on all trees within the 0.10-acre circular plot that above the breakpoint diameter. Also, additional plots around the instrument plot are established and sampled using the Level II protocol.

Fuel loading estimates and IMT weather intelligence.— Same as Level II.

Level III Post-fire

Site characterization and Fuel loading estimates.— Same as Level II.

TEAM #2—IN SITU INSTRUMENTATION—BRET BUTLER, PATRICK FREEBORN, ROBERT KREMENS

One unique aspect of this study has been the development of a field deployable ground based sensor package that provides *in situ*, time-resolved measurements of radiant and convective energy transfer from the fire, horizontal and vertical air flow, air temperature, and digital video footage of the fire behavior. Previously, arrays of thermocouples and radiometers have been utilized in laboratory controlled experiments to measure flame temperatures and heat fluxes. For example such experiments have been conducted in a wind tunnel to investigate the effects of ambient air conditions and windspeed on fire spread rate and intensity. Although thermocouples and radiometers have demonstrated their utility in the laboratory, by the nature of the experimental design these instruments have generally been subjected to simulated, homogeneous, and repeatable fire behavior. Rather than recreating the natural variability of fuel arrangements and environmental conditions in the laboratory, instruments strategically positioned in the path of an oncoming wildland fire provide an opportunity to collect *in situ* measurements of combustion reactions that occur on the landscape.

Research efforts have provided the opportunity to improve these sensors through a series of Rapid Response field trials. The result is a system suite that is not only robust, but also easy to operate, simple to deploy, fire proof, and light weight. Three independent but complementary instrumentation packages comprise the suite of *in situ* measurement equipment: 1. Fire Behavior Flux Package; 2. Video Acquisition Box; 3. Autonomous Environmental Sensor.

Fire Behavior Flux Package (FBP)

Four fire behavior packages were designed and manufactured to collect *in-situ* measurements of wildland fire environments. Specifications for the fire behavior packages, including the spectral and spatial characteristics of the hemispherical and narrow angle radiometers are summarized in Table 2. Each autonomous package contained the following instruments: (1) a total heat flux sensor, (2) a nearly hemispherical radiometer with a field of view (FOV) of $\angle 130^{\circ}$, (3) a narrow angle radiometer (NAR) with a FOV of $\angle 4.5^{\circ}$, (4) a type-K (chromel/alumel) thermocouple exposed to the ambient, and (5) a pair of pitot-static type velocity probes. Both the total heat flux sensor and the hemispherical radiometer were Schmidt-Boelter type thermopiles (Medtherm Co.[*1]), however the surface of the latter was isolated from conductive and convective heat transfer by a sapphire window transparent to infrared wavelengths. Although the NAR also incorporated a thermopile detector with a wide FOV (Meggett Avionics) the aperture cavity in the radiometer housing limited irradiance from an external source to a narrow solid angle. Small-gauge shielded thermocouples measured flame, gas, and air temperatures, while pressure sensors measured horizontal and vertical components of the airflow. All instruments were connected to an internal data logger

[1] The use of trade, firm, or corporation names in this publication is for the information and convenience of the reader. Such use does not constitute an official endorsement or approval by the U.S. Department of Agriculture of any product or service to the exclusion of others which may be suitable.

powered by a rechargeable battery. The FBPs are typically deployed so that the sensors are directed towards the oncoming fire front. The data loggers are capable of logging over one million samples which translates to a maximum logging duration of 30 hours at a 1 hertz sampling rate. The most recent version of the FBPs includes a wireless transmitter which allows the datalogger to send a signal to turn on a nearby video camera (discussed below).

Currently, four of the latest-generation fire behavior packages have been fabricated to collect *in situ* measurements in wildland fire environments. Details on package size, sensor layout and datalogger location are can be seen in Figures 7, 8, and 9. Table 2 provides details about individual sensors and their engineering specifications.

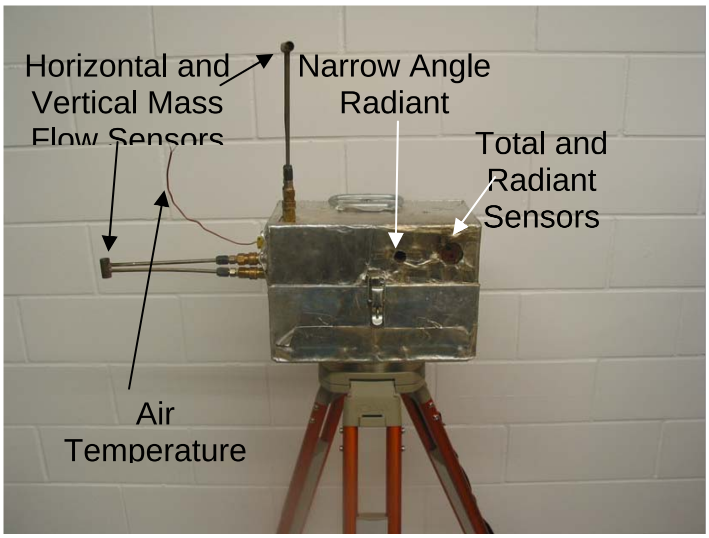

Figure 7—View of Fire Behavior Package with sensors labeled.

Figure 8—View of Fire Behavior Package datalogger. Logger is accessed through hinged door on package face.

Figure 9—View of Fire Behavior Package battery and electronics, accessed through hinged panel on rear of box. Note aluminum heat sinks for thermal sensors.

The total heat flux transducers and hemispherical radiometers were factory calibrated by Medtherm Co. according to ISO 10012-1, ANSI/NCSL Z540-1 and MIL-STD-45662A with traceability to the National Institute of Standards and Technology (all calibration relationships and regressions are provided in Appendix A). The NAR's were calibrated in-house against a Mikron M300 blackbody cavity with an emissivity of 0.999 ±0.0005. Source temperatures ranged from 373 K to 1423 K. The NAR's were positioned flush with the faceplate so that the blackbody cavity filled their entire FOV, and a continuous output voltage was recorded at 1 hz for a minimum of 15 seconds. The objective of calibration was to relate the output of an individual detector to the total radiant flux density emitted by the source object inducing the response. Configuration factors (i.e. view factors) were not determined since (1) the actual flux across the detector was not calculated, and (2) it was assumed that the FOV, or IFOV, was completely filled by an isothermal and diffuse emitter. At 19 blackbody temperature setpoints, the NAR output voltage (mV) was averaged over the exposure interval. For the four NAR's, the output signal was linearly related (Appendix A) to the total blackbody exitance, M_b, calculated using the setpoint temperature of the blackbody and Stefan Boltzmann's Law:

$$M_b = \sigma T_b^4 \qquad \text{Eq [1]}$$

where σ is Stefan Boltzmann's constant of 5.67 x 10^{-9} $Wm^{-2}K^{-1}$, and T_b is the setpoint temperature of the blackbody in Kelvin. Irradiance due to thermal emission from the radiometer housing outside of the 4.5° aperture, but within the detector FOV, was considered negligible and assumed constant regardless of operating condition.

Table 2. In-situ Fire Behavior Package (FBP) Specifications

Sensor/component	**Specification**
Narrow Angle Radiometer	
Sensor	Thermopile (Meggett Avionics)
Spectral Band of Sensor	0.15 – 7.0 µm with sapphire window
Field of View	~4.5º controlled by aperature in sensor housing
Transient Response	Time constant of sensor nominally 30msec
Units of Measurement	Calibrated to provide emissive power of volume in FOV in $kW\text{-}m^{-2}$
Total Energy Sensor	
Sensor	Schmidt-Boelter Thermopile
Spectral Band of Sensor	All incident thermal energy
Field of View	~130º controlled by aperature in sensor housing
Transient Response	< 290msec
Units of Measurement	Total heat flux incident on sensor face in $kW\text{-}m^{-2}$
Hemispherical Radiometer	
Sensor	Schmidt-Boelter Thermopile
Spectral Band of Sensor	0.15 – 7.0 µm with sapphire window
Field of View	~130º controlled by window aperature
Transient Response	< 290msec
Units of Measurement	Radiant energy incident on sensor face in $kW\text{-}m^{-2}$
Air Temperature	
Sensor	Type K bare wire thermocouple, new, shiny, connected to 27ga lead wire
Wire Diameter	0.13mm
Bead Diameter	~0.16-0.20mm
Units of Measurement	Degrees Celsius
Air Mass Flow	
Sensor	SDXL005D4 temperature compensated differential pressure sensor
Pressure Range	0-5 in H_2O
Sensor Design	Pressure sensor is coupled to custom designed bidirectional probe with ±60º directional sensitivity.
Units of Measurement	Calibrated to convert dynamic pressure to velocity in $m\text{-}s^{-1}$ assuming incompressible flow
Sensor Housing Dimensions	150× 180 × 270 (mm)
Housing Weight	7.7 kg
Power Requirements	12V DC
Power Supply	Rechargeable Internal Battery
Data Logging	Campbell Scientific Model CR10X
Sampling Frequency	Variable but generally set at 1 Hz
File Format	ASCII

Video Acquisition Box (VID)

Digital video imagery is an integral component of our field campaigns. Although the *in situ* sensor packages are capable of detailed measurements in real time, the researcher's ability to understand and interpret the data is greatly enhanced when digital video footage of the specific fire behavior at the sensor location is provided. Therefore, each FBP sensor pack is typically coupled with a digital video recorder for simultaneous recording of video and in-situ measurements. Collecting video imagery not only allows us to observe the actually footage of the fire behavior, but also provides insight into our data analysis. Digital video is acquired by camera(s) housed within 10cm by 18cm by 19cm fireproof enclosures. The camera boxes are designed to be lightweight and compact in order to minimize bulk; they are constructed of 1.6 mm aluminum, weigh approximately 1.0 kg. The boxes have a double lens configuration of high temperature Pyrex glass and a second lens of hot mirror coated glass (Edmund Optics). This multi-layer dielectric coating reflects harmful infrared radiation (heat), while allowing visible light to pass through. The cameras can either be turned on manually or can be set to trigger and record through a wireless link to the FBP dataloggers. The system has been used extensively in full scale crown fires. Analysis of the visual video images provides an objective method for measuring flame height, flame length, flame depth, flame angle and fire rate of spread. See Figure 10 for details of the video housing.

Figure 10—View of digital camera enclosure (10cm X 18cm insulated aluminum) and camera mounting plate.

FBP/VID Remote Triggering

The coupling of FBP and VID systems allows researchers to see actual video footage of the fire behavior as flames approach, envelope, and disperse past individual sensor packs. However, the limiting factor in this process has been the amount of recordable video tape—typically 60-90 minutes of record time. This requires researchers to remain in close proximity to the advancing fire in order to activate the fire behavior sensor and video packages within 60 minutes of the approaching fire front, which raises both tactical and safety-related concerns.

Recognizing the need to reduce risk to research team members and improve utility and reliability of the instrument system, efforts were directed at developing a safe, ruggedized low cost datalogger/camera triggering system. The development of this technology was not trivial and required a constant level of effort over a significant amount of time to develop, construct, and test various trigger methods and designs. Some of the options considered included radio frequency, infrared technology, and handheld remote and automatic systems.

The end result was a wireless trigger design based on the SONY proprietary LANC connector technology (thus the system is only compatible with SONY cameras). While any digital video camera that meets the size requirements can be used in the VID boxes, only SONY cameras are compatible with the automatic trigger system. The preferred model is the SONY PC-1000 HandyCam digital video camera. These cameras were chosen for their relatively high quality construction and image capability and the availability and variety of cameras and associated hardware (i.e. batteries, cables, etc). The system allows users to trigger the recording mechanism of the camcorder remotely by using its own unique internal computer source code. Although the LANC connector is wired directly to the camcorder, by reverse engineering the signals within the LANC system we were able to differentiate the source code and determine how to remotely trigger the on/off switch using Radio Frequency (RF), much like a remote garage door opener. Radio frequency was chosen over Infra Red (IR) technology due primarily to line-of-sight and interfering reflectance issues. In order to incorporate the wireless technology into our FBP design each package needed to be fitted with a RF transmitter and likewise the video boxes needed to be fitted with a RF receiver. This equipment was designed and assembled in-house using over-the-counter RF supplies (Figure 11, Figure 12). The transmitter and receiver operate off the internal battery power sources available in the FBP and VID cases. Once the FBP and VID boxes are deployed, the trigger system is armed from readily accessible switches in the respective enclosures.

This new trigger system allows the fire behavior and video packages to stay in "sleep" mode until a measurable rise in heat flux or air temperature is detected. The detection activates the fire behavior sensor package to begin logging data which then sends a wireless signal to activate the video camera package. The unique capability and hardware have been tested for range and interference over wide ranges of fire intensities and fuel types in open and densely-treed plots as well as in fire and non-fire settings. In all the cases, the system effectively and consistently activated the equipment at distances up to 100 yards. The result is a system that is reliable, able to withstand the high temperatures of fires and provides researchers and managers with the capability to quantify fire intensity and behavior safely and effectively. The components required for this conversion cost approximately $100. Schematics for the layout of the system and components can be obtained from Jim Reardon at the Fire Sciences Laboratory in Missoula, MT.

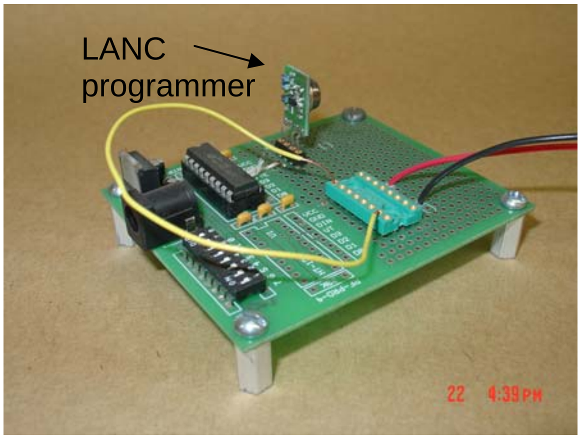

Figure 11—View of RF electronics for automatic camera trigger. Power and antennae are red/black and yellow wires, respectively.

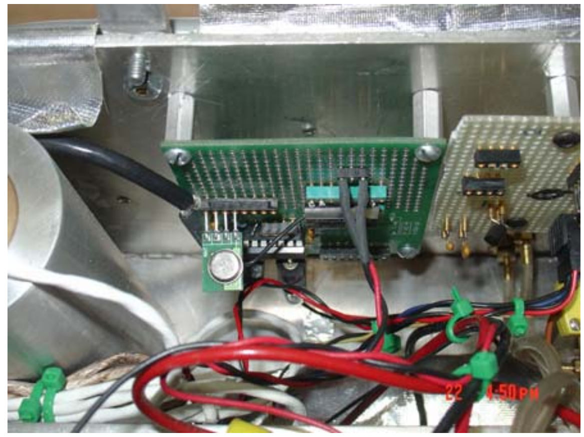

Figure 12—View of trigger electronics mounted in Fire Behavior Package.

As a result of these efforts—engineering, design, and testing—we have eliminated the need for human interaction to activate data collection hardware and video recording equipment. This new trigger system allows the fire behavior and video packages to stay in "sleep" mode until a measurable rise in heat flux or air temperature is detected. The detection activates the fire behavior sensor package to begin logging data which then sends a wireless signal to activate the video camera package. The unique capability and hardware have been tested for range and interference over wide range of fire intensities, and fuel types in open and densely-treed plots as well as in fire and non-fire settings; in all the cases, the system effectively and consistently activated the equipment at distances up to 100 yards. They provide managers with the capability to quantify fire intensity and behavior safely and effectively[2].

These systems have been used to collect quantitative fire information for support of fire-induced plant and tree studies, firefighter safety zone studies, crown fire transition studies, and for comparing ecosystem management methods and techniques. The systems have been deployed on prescribed and natural fires from Alaska to Florida, Europe, and Australia (Figure 13). The designs can be adapted to fit other sensors and data loggers. The FBP enclosures can be constructed for approximately $300 per box plus cost of data loggers, and sensors. The VID enclosures can be constructed for $450 per box plus cost of cameras. Users of the hardware and designs include JoAnn Fites-

[2] A checklist for a rapid response deployment of the *in situ* instrumentation is provided in Appendix B.

Kaufman (manager of the U.S. Forest Service Adaptive Management Services Enterprise Team, Dr. Matthew Dickinson (research Ecologist with the US Forest Service Northeastern Research Station), and Dr. Miguel Cruz (research Ecologist with Australian CSIRO Forestry Research Group in Canberra, Australia), Jason Simmons (BLM Fire Ecologist for experiments at Knife-River Village in North Dakota). Many others have proposed cooperative studies that have not yet occurred due to either scheduling or weather-related delays in prescribed burns.

Figure 13—Rapid Response *in situ* instrumentation team installing the digital camera system on the Dragon WFU Incident.

Autonomous Environmental Sensor (AES) — Robert Kremens

Autonomous Environmental Sensors (AES) are instrument packages consisting of a versatile data logger, a suite of sensors that can measure various aspects of the fire environment, and the associated packaging and battery power supplies to enable portable, remote operation. Special attention was paid to input signal versatility, the ability to accept GPS signals from conventional GPS receivers for time synchronization and location determination, portability and long battery life.

During the course of this Rapid Response project, the autonomous environmental sensors have evolved to be smaller, easier to deploy rapidly and more capable. There are now four models (MODs), each of which are discussed in this section. The number and type of sensors that can be used with the AES has been increased, and additional custom circuit boards with conditioning electronics have been designed for thermocouples, infrared thermopile sensors, silicon (visible/near-infrared) diode detectors, and electro-chemical gas detectors. In addition, the battery lifetime has been extended from roughly one day to more than 7 days with the standard 8-cell battery pack. This performance increase has come from the development of new sensors, redesign of the main circuit board, and improvements in software. The AED units can also relay information to a distant receiver (1-30 km, depending on terrain) via secure radio (Maxstream Inc. radio modems), but with slightly reduced battery life.

AES$_{MOD1}$. — The initial AES instrument (MOD1), deployed on Cooney Ridge Complex, had the following specifications:

AES$_{MOD1}$ Measurement Suite

- Wind speed and direction measured at ~ 1.5 m (5 feet) above ground
- Wind Speed (average over 10 seconds)
- Wind Direction (sampled once per 10 seconds)
- Temperature
- Relative Humidity
- Long Wave Infrared flux, sampled over a 2 m^2 area at a slant angle of 45^o
- Battery Life (6 X AA Alkaline) ~1.5 days
- Weight ~ 21 pounds
- Records are taken with GPS position and GPS time synchronized
- Deployment time ~ 15 minutes
- All units sample simultaneously

AES$_{MOD2}$. — Following initial deployment of the AES$_{MOD1}$ configuration, we implemented numerous improvements to existing system design, and also added significant functionality and measurement capabilities. Specifications for this newer version (AES$_{MOD2}$), deployed at both the Dragon WFU and the Tripod Complex, are presented in the following tabulation:

AES$_{MOD2}$ Measurement Suite

- Wind speed and direction measured at ~ 2.44 m (8 feet) above ground (corresponds to RAWS low position)
- Wind Speed (average over 10 seconds)
- Peak Wind Speed
- Direction of Peak Wind
- Wind Direction (moment, averaged over 10 seconds)
- Long Wave Infrared flux, sampled over an 8m^2 area at vertical incidence
- Temperature
- Relative Humidity
- Carbon monoxide concentration (sampled with 20 seconds response time, 0 -500 ppm)
- Records are taken with GPS position and GPS time synchronized
- Weight ~ 11 pounds
- Deployment time ~ less than 5 minutes
- Battery Life (8 X AA Alkaline) ~ 7 days
- Mid Wave Infrared flux, sampled over an 8m^2 area at vertical incidence
- All units sample simultaneously

These MOD2 improvements resulted in five overall improvements and efficiencies contributing to improved scientific consequences:

1. Dual band infrared measurement corresponds very closely to aircraft wavelength pass bands for FireMapper and WASP airborne IR camera systems.

2. Infrared sampled area corresponds more closely to aircraft system ground spatial resolution.
3. Can now field deploy (one man) 4 units instead of 2 increasing spatial sampling.
4. Rapid deployment using only one driven stake for instrument mounting.
5. The weather measurements are now taken in compliance with standard weather temporal sampling and averaging practices.

A diagram of the AES_{MOD2} instrument configuration, as deployed on the later (Tripod fire, 2006) experiments is shown in Figure 14.

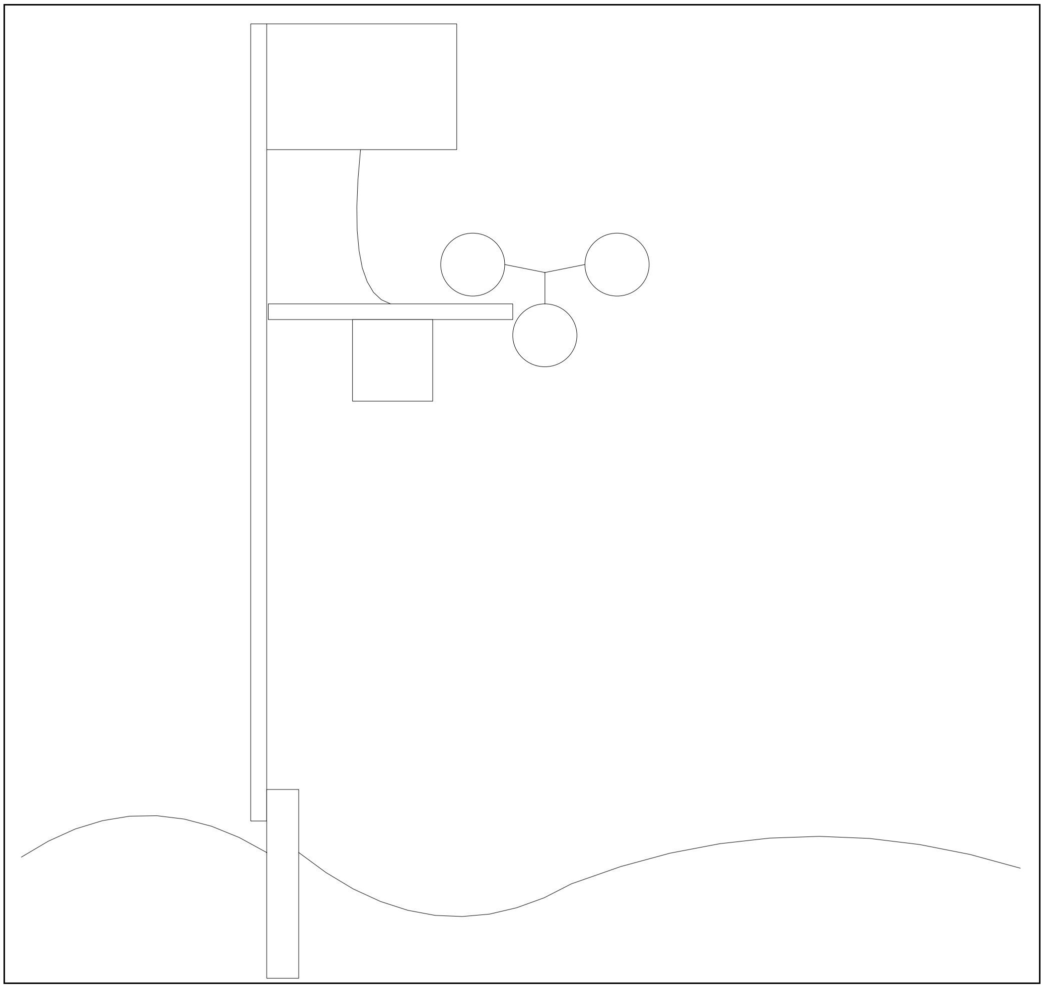

Figure 14—Configuration of AES_{MOD2} for JFSP Rapid Response projects.

AES_{MOD3}. — Using the same basic design developed under this JFSP Rapid Response project, the instrument has since been further developed utilizing funding from another JFSP project (Dickinson, et al) into a more complex version (AES_{MOD3}), with enhanced capabilities, as specified in the tabulation below:

AES_{MOD3} Measurement Suite

- Wind speed and direction measured at ~ 2.44 m (8 feet) *and* 6.1 m (20 feet) above ground (corresponds to RAWS upper and lower positions)
- Wind Speed (average over 10 seconds)
- Wind Direction (moment, averaged over 10 seconds)
- Direction of Peak Wind
- Peak Wind Speed
- Temperature at 2.44 and 6.1 m
- Air temperature range extended from 200 C to 740 C
- Relative Humidity
- Carbon monoxide concentration measured at 2.44 and 6.1 m (sampled with 20 seconds response time, 0 -500 ppm)
- Mid Wave Infrared flux, sampled over a 30m^2 area at vertical incidence
- Long Wave Infrared flux, sampled over a 30m^2 area at vertical incidence
- Battery Life (8 X AA Alkaline) ~ 7 days
- Deployment time ~ less than 10 minutes
- Weight ~ 18 pounds
- Records are taken with GPS position and GPS time synchronized
- All units sample simultaneously

A schematic of the AES_{MOD3} system, as installed on a site, is shown in Figure 15, and a photograph of the instrument package installed on the Tripod Complex is shown in Figure 16.

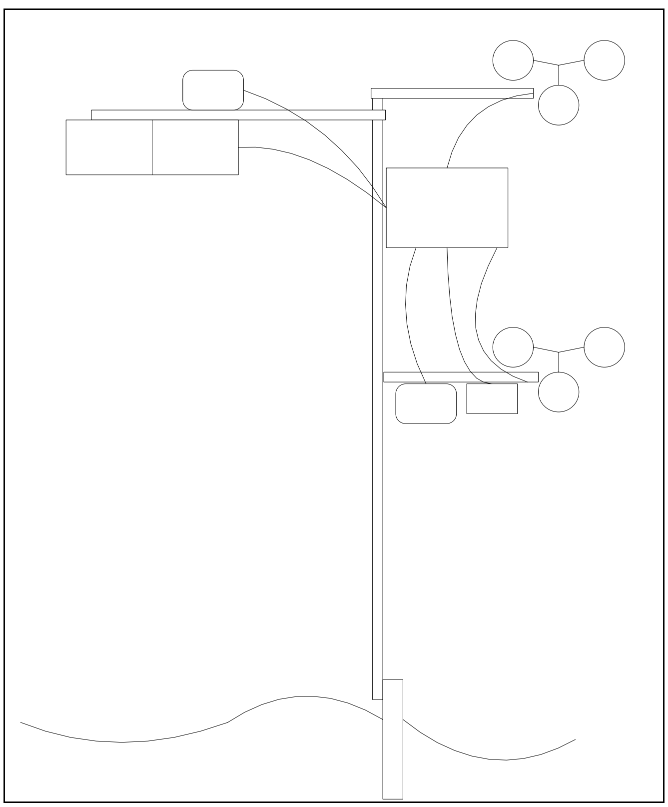

Figure 15—Enhanced-capability AES_{MOD3} deployed on 6.1 m (20 foot) portable tower.

Figure 16— Photograph of an AES_{MOD3} package deployment on the Tripod Fire in Washington (2006). The two units shown have been burned over by the fire but are still functional. The data logger package is buried a small distance beneath the surface to shield it from the effects of the fire.

The AES_{MOD3} uses an Atmel ATMega 128 8-bit microcontroller that has 4 kbytes of RAM and 128 kbytes of program storage (Figure 17). Also on the circuit board is a National LM4120 precision voltage reference, Dallas DS1302 real time clock, Linear Technology LTC1598 8 channel 12 bit high speed A/D converter, a downconverting switching power supply using the NationalLM2594, a Linear Technology LT1180 dual channel (2 X Tx, 2 X Rx) RS232 driver circuit and a TI TPS2024 analog switch that supplies a computer controlled source of regulated 5V, 100 mA power for peripherals. Data is stored locally in standard Microsoft-readable .csv file format on a removable Compact Flash memory card. In the configuration used for these experiments, the card can store about 256 thousand weather records (about 2 months at 10 second sampling rate).

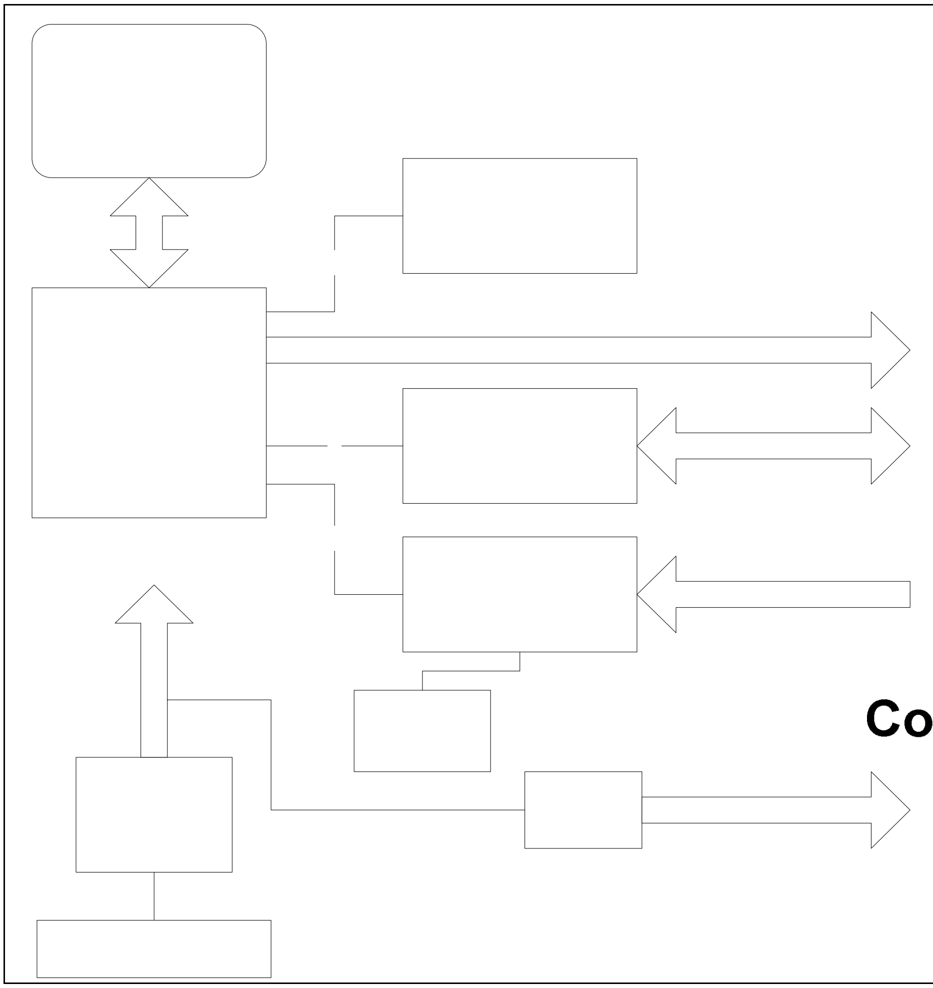

Figure 17— Block diagram of the AES_{MOD3} data logger.

An advantage of this data logger over commercially available units is the ability to accept a number of digital and analog inputs of practically any type and mixture. For example, in the configuration used in Figure 15 there are 8 analog 12 bit channels for the infrared and carbon monoxide sensors, two 'One-Wire' interface channels for the weather head units (wind vane/anemometer/temperature), a I^2C interface for the humidity sensor, and several RS232 serial channels for GPS synchronization and monitoring and control functions. Additional sensors with digital output can be added easily. The development package (MCS Electronics BASCOM-AVR) used to program the microprocessor on the logger fully supports the following interfaces:

- IEEE RS-232
- One-Wire
- LCD Displays
- PC-style keyboards
- X-10
- I2C
- SPI
- IR Remote Control

With the addition of a low cost auxiliary microprocessor and radio unit, the AES_{MOD3} units may even be reprogrammed remotely via a radio link.

AES_{MOD4}. — We have also developed an alternate AES system (AES_{MOD4}) with limited capability but having the advantage of very small size (3" X 2 X 2") and even longer battery life (~ 4 weeks). . The specifications of the simplified AES_{MOD4} are tabulated below, followed by a detailed diagram for the AES_{MOD4} logger shown in Figure 18.

AES_{MOD4} Measurement Suite

- 4 X 10 bit analog-to-digital conversion channels
- Up to 36,000 stored samples (192K storage)
- One-wire ready for weather head use
- Battery life ~ 4 weeks with 3 X AA cells and 10 second sampling
- RS-232 input/output for GPS synchronization, data downloading and 'monitor' mode
- 1.75" X 2.25" circuit board size (mates to 3 X 'AA' battery pack)
- Sample time of 10, 30 or 60 seconds standard
- Precision voltage reference
- 'Sleep' mode for unlimited battery life (depending on sample rate)
- Crystal controlled real time clock

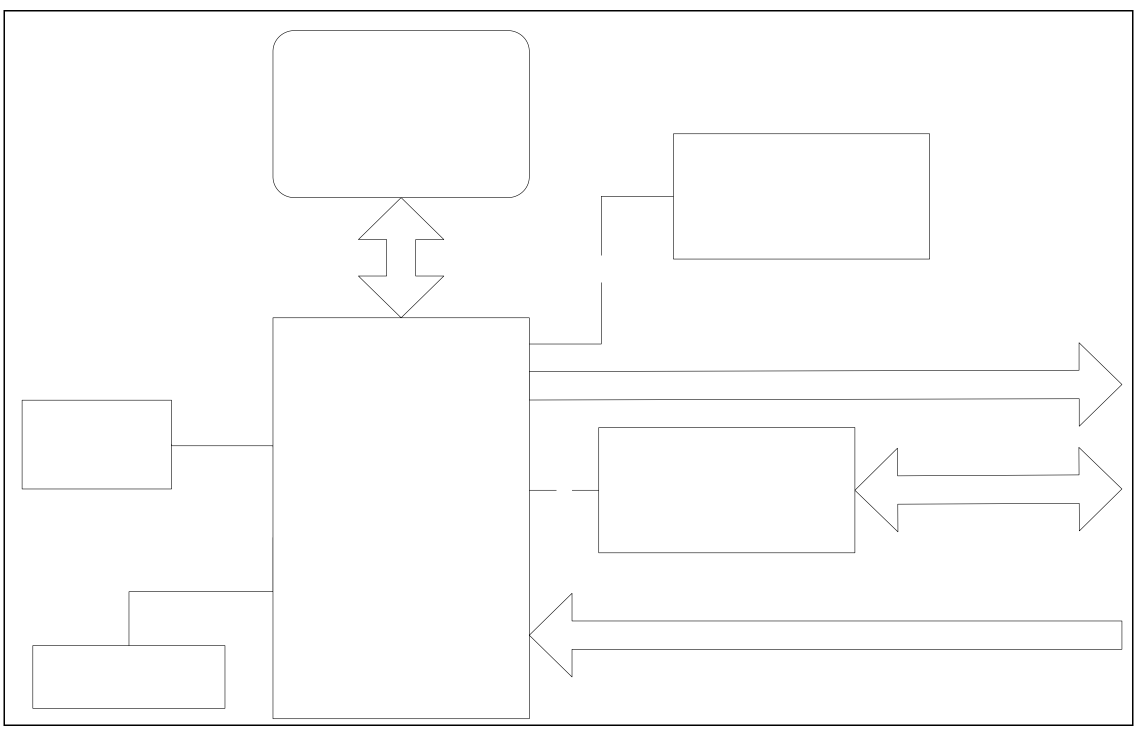

Figure 18— Block diagram of the limited-functionality AES_{MOD4} data logger.

Instrument Layout for All-systems Deployment

A fully-instrumented ("rich") deployment of the three systems (FBP, VID, AES) is depicted in Figure 19. Installation involves distribution and orientation of the systems whereby the viewing geometry can capture as much of the energy as possible from both the approaching fire-front and the post-frontal combustion process across the plot.

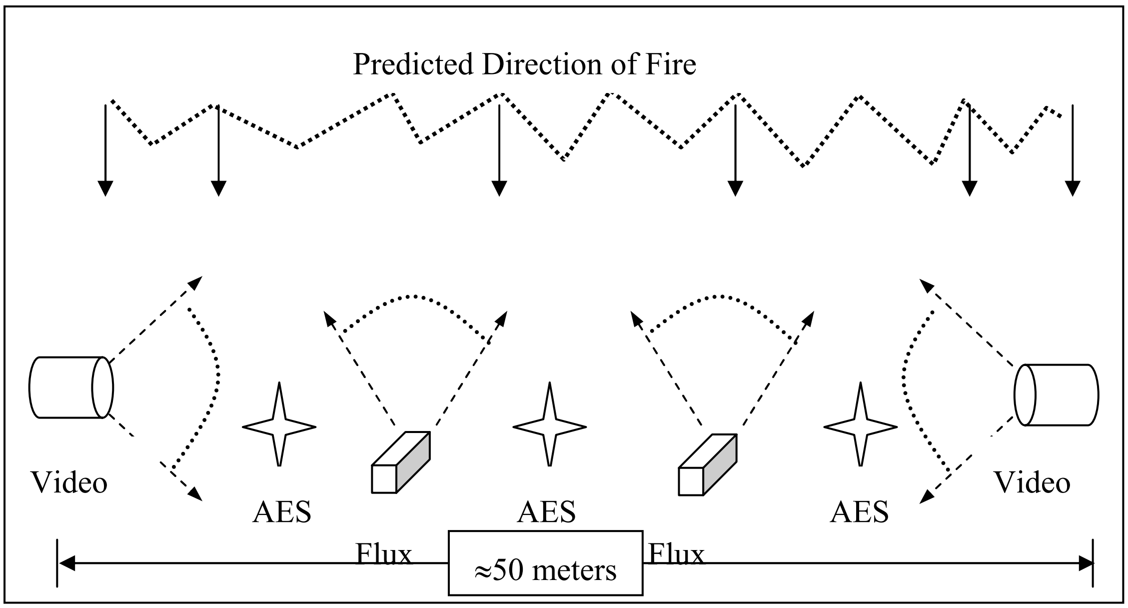

Figure 19. Primary plot area instrumentation layout.
Note: AES=Autonomous Environmental Sensor; Flux=Fire behavior flux package (FBP).

TEAM #3—OBLIQUE THERMAL INFRARED—PATRICK FREEBORN

Thermal Infrared Camera Specifications and Calibration

Similar to thermocouples and radiometers, thermal imaging systems have demonstrated their utility in the past, however this demonstration project expands upon a relatively new application. Thermal infrared (TIR) cameras stationed at a ground-based vantage point offer spatially explicit radiometric temperatures of wildland fires at a relatively high temporal and spatial resolution (Freeborn et al. 2004). The purposes of collecting thermal images from an oblique vantage point were (1) to provide an intermediate level of resolution between the site and aircraft measurements, (2) to compliment *in-situ* and aircraft measurements with respect to interpreting fire behavior and estimating first-order fire effects, and (3) to fully exploit the capabilities of stand-alone TIR cameras and their unique viewing arrangement. Compared to *in-situ* measurements of radiant heat flux collected at a point location within a study site, a thermal image characterizes the thermal distribution across the landscape. Compared to thermal images captured from an airborne platform, the sampling frequency of a ground-based observation is not limited to the overpass or loiter times of the aircraft.

Two commercial thermal infrared (TIR) cameras were also utilized during field campaigns. Specifications for the CMC Electronics Cincinnati TVS-8500 and the Mikron Infrared Inc. MikroScan 7200 are also provided in Table 3. To eliminate molecular band radiation due to CO_2 emission centered at approximately 4.3 μm, a "twin peaks" spectral response for the TVS-8500 was sensitive to two narrow bands of middle infrared wavelengths (3.4 – 4.1 μm and 4.5 –5.1 μm). In contrast, the MikroScan 7200 has a flat spectral response in the long-wave atmospheric window (~7.5 – 14.0 μm). Bandpass radiance, or the mean spectral radiance, for each camera was theoretically calculated as a function of brightness temperature using Plancks Law (Incropera and DeWitt 1996) and the spectral response of the system. As a midwave sensor, the TVS-8500 required four overlapping dynamic ranges to span brightness temperatures from 293 K to 923 K. The MikroScan 7200, however, required only one dynamic range to span brightness temperatures from 273 K to 773 K. At a sensor-to-target distance of 1000 meters the TVS-8500 and MikroScan 7200 provided ground cell resolutions of 1.0 m^2 and 2.5 m^2, respectively. Each unit had the ability to save 14-bit images to a compact flash card in a proprietary file format, or to stream data continuously via an IEEE1394 Firewire® interface.

Table 3. Thermal infrared (TIR) camera specifications.

Component	**TIR Camera**	
	CMC Electronics Cincinnati TVS-8500	**Mikron Inc. MikroScan 7200**
Detector	256 × 236 InSb Focal Plane Array (FPA)	320 × 240 VOX Microbolometer Focal Plane Array (FPA)
Spectral Band	3.4 – 4.1 μm & 4.5 – 5.1 μm	7.5 – 14.0 μm
(Instantaneous) Field of View	1 mrad IFOV (14.6º FOV)	1.58 mrad IFOV (28.9º FOV)
Dimensions	152 × 178× 279 (mm)	97 × 109 × 170 (mm)
Weight	5.0 kg	1.6 kg
Power Requirements	100-240V AC (40W)	7.2V DC (6W)
Power Supply	• Solar Panel • Power generator • Marine battery • 12V car adaptor	Rechargeable Li-ion Battery
Data Logging	• CompactFlash Card • IEEE 1394 Firewire® • Internal Memory	• CompactFlash Card • IEEE 1394 Firewire®
Sampling Frequency	• 0.2 Hz (maximum) • 30 Hz (maximum) • 120 Hz (maximum)	• 0.2 Hz (maximum) • 30 Hz (maximum)
File Format	14 bit proprietary image	14 bit proprietary image

The TIR cameras were calibrated in-house against a Mikron M300 blackbody cavity with an emissivity of 0.999 ±0.0005. Source temperatures ranged from 373 K to 1423 K. Both thermal cameras were positioned approximately 0.6 m from the faceplate and aligned so that the entrance tube extending into the cavity appeared as concentric rings. Thermal images were captured in every dynamic range capable of detecting an IR signal above the background noise, but below saturation. At 22 blackbody temperature setpoints, the center of the cavity was subset from the thermal images using circular areas of interest (AOI's) composed of 1025 and 889 pixels for the TVS-8500 and MikroScan 7200, respectively. For the four dynamic ranges of the TVS-8500, the average digital number (DN) within the AOI was linearly related to bandpass radiance, which was then converted to brightness temperature using a look up table (LUT) with a resolution of 0.5 K. In turn, brightness temperature was used to calculate total blackbody exitance using Eq 1 such that DN and blackbody exitance were related according to Appendix B, figure c. For the single range of the MikroScan 7200, the average DN within the AOI was linearly related to the blackbody setpoint temperature, and again, total blackbody exitance was calculated via Eq. 1.

Study Site and TIR Camera Vantage Point Selection

Once a wildland fire was selected as a candidate for measurement, the first priority was to identify locations on the landscape suitable for instrument installation. Given adequate preparation time, publicly available spatial data was gathered prior to arrival on-scene. Elevation data was downloaded with a 3 km buffer around current fire perimeters, and an individual digital elevation model (DEM) was subset for each separate fire within a greater complex. Thirty meter (1 arc second) DEM's were sufficient, but where available, 10 m (1/3 arc second) DEM's were utilized. Digital raster graphics (DRG) of 7.5-minute topographic maps served as base layers, and provided additional, non-topographic information. Point and line features in cartographic feature file (CFF) format supplemented the information interpreted from the DRG's, and as an independent layer, further enhanced the flexibility of the GIS analysis. Although the CFF extents overlapped the DRG's, the CFF features were considered more reliable since field units provided updates for this dataset. Upon arrival at an incident, immediate integration with the incident management team (IMT) and further coordination with the GIS specialist facilitated the transfer of time-sensitive spatial data, such as completed hand line, division breaks, and daily fire perimeters.

Depending on the situation, potential study sites with companion vantage points were evaluated within a geographical information systems (GIS) framework. Viewshed analyses were performed in two directions: either the viewshed at a study site was used to identify potential vantage points, or conversely, the viewshed from a TIR camera location was used to identify potential study sites (Figure 20). Regardless if pre-work was conducted in a GIS, reconnaissance of both the study site and camera location was absolutely necessary to verify an unobstructed line of site, and to establish escape routes and safety zones. Ultimately, the following criteria dictated the spatial coupling of a study site with an oblique vantage point: (1) proximity to the fire perimeter, (2) reasonable access and safe egress, (3) viewing geometry, (4) fuel loadings and vegetation, and (5) timing. Considerations for the viewing geometry included the viewshed as well as the observation angle, or the planar angle between the line of site and the surface normal of the intersecting ground cell. Furthermore, in relation to the 4th criteria, fuels at the study site needed to be able to support fire without damaging the *in situ* instruments, and vegetation outside of the plot area that obscured the line-of site of the TIR cameras was avoided.

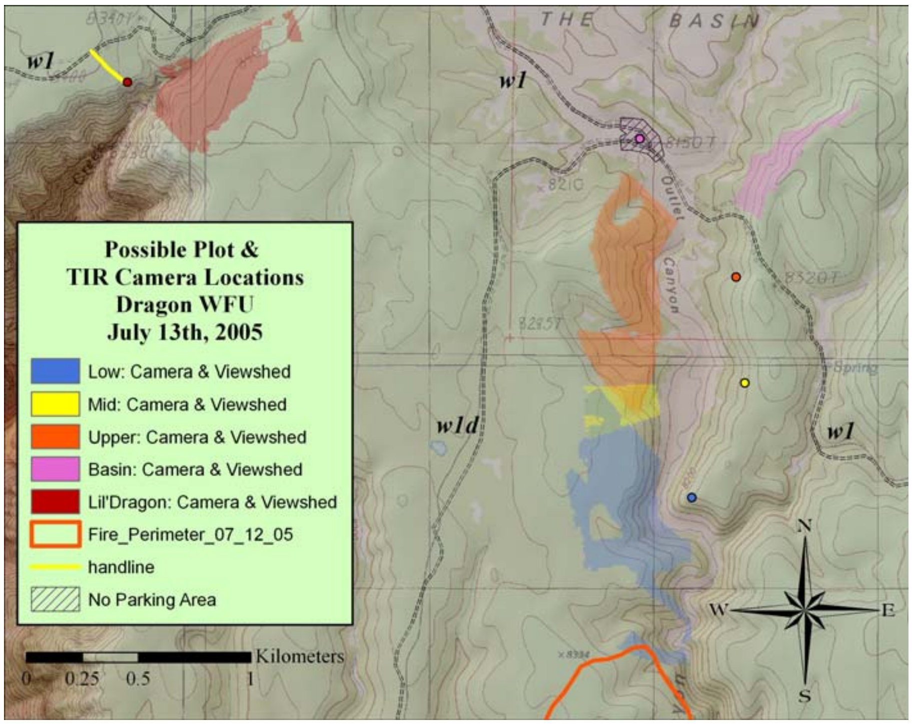

Figure 20. Preliminary GIS analysis for five potential sensor deployment scenarios on the Dragon WFU Fire, 13 July 2005. Viewsheds are color coded to represent the ground area visible from a particular exposure station in the absence of non-topographic obstructions.

Equipment Installation, Image Georegistration, and Data Collection

Once the study site and corresponding vantage point were selected, and after the equipment was packed to their respective locations, sensors were installed on the landscape. Ideally, two fire behavior packages were deployed per study plot, and each package required one person approximately 15 minutes to assemble. Instruments were protected from the harsh environment by wrapping the boxes with insulation and fire shelter material. Packages were positioned on the circumference of the study site, leveled atop a 1 m surveyor's tripod, and oriented towards plot center. Data loggers were pre-programmed to begin recording when the heat flux measured by the hemispherical radiometer exceeded a minimum threshold. Using the output signal, and the corresponding sensor-specific linear calibration, transformations between voltage and heat flux were performed as part of a real-time processing chain. Heat flux (kW/m2), the ambient temperature (ºC), and the output voltage of the velocity probes (mV) were stored in memory as raw data with a timestamp. Data was collected at 1 hz for 3 hours or until the unit was manually shut down.

It also took approximately 15 minutes at the vantage point for two personnel to connect the power supply, and mount, level, and orient the TIR cameras on their tripods. Cameras were synchronized to GPS time. Anticipating the fire's progression and behavior, the study site was framed within the FOV, and tripods were locked in place to maintain a fixed viewing geometry. A flameless propane heater measuring 20 cm in diameter was used as a thermal marker during field georegistration procedures. The heater was held facing the camera at several gaps in the canopy surrounding the study site. Tie points were then generated by coupling the ground control coordinates recorded by a GPS receiver to the pixel coordinates associated with an elevated thermal signal (Figure 21).

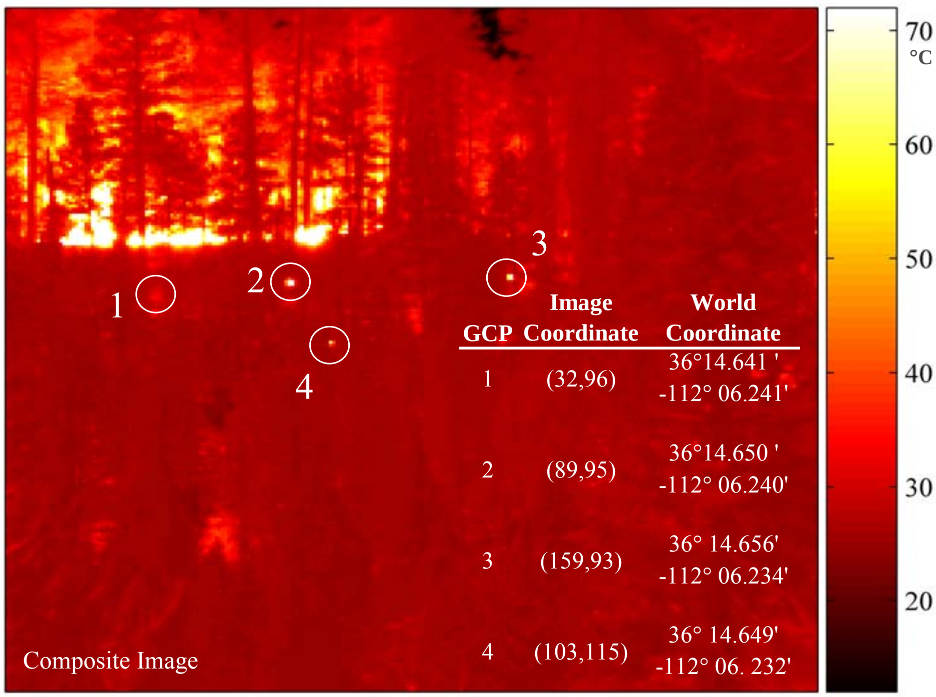

Figure 21. Composite of four images collected during field georegistration procedures. Thermal ground control points (GCP's) are identified by their image and geographic coordinates.

Unlike the autonomous, *in situ* instruments, the TIR cameras required constant attention. Shared responsibilities at the camera location included logistics and communication, however one person was strictly dedicated to the operation of the cameras while the second person kept a lookout, and maintained good situational awareness. Data collection was manually initiated based upon the proximity of the fire front to the study site. Sampling frequencies varied depending on the model of the TIR camera, the duration of the experiment, limitations of storage media, and current fire behavior. Sampling frequencies ranged from 2 frames per minute (.033 Hz) during smoldering processes to 8 second bursts at 120 Hz during crown fire activity. Given the spatial and spectral characteristics of each TIR camera, and the sensor-to target distances achieved during these field experiments, a single dynamic range for the longwave camera was sufficient to fully capture background brightness temperatures without saturating over pixels containing fire. In contrast, it was necessary to subjectively increment, and decrement, the dynamic range of the midwave camera to prevent pixel saturation as the flaming front occupied a greater, and lesser, portion of the tenth-acre plot area. Sampling was terminated at the end of the operational burning period or when the majority of pixels in the study site exhibited relatively cool brightness temperatures, whichever came first.

A review of the location and attitude of each sensor (both the in situ FBP [A] and the TIR camera [B]) with respect to the wildland fire is presented in Figure 22. The differential element of area, *dA*, representing the surface of a radiometer within an *in situ* package is oriented vertically (i.e., along the z-direction), but never perfectly orthogonal to the ground cell beneath it (i.e., the x-y plane), as illustrated in Figure 22a. When the *in situ* package is overcome by fire, radiation emitted from a hemisphere surrounding the face of the thermopile is truncated to an acceptance angle of either ∠130° or ∠4.5° depending on the style of the radiometer housing. In contrast, radiative heat transfer involving a ground cell in the study plot and a detector in a focal plane array can be represented as an interaction between two solid surfaces (Figure 22b). Radiant energy traverses the line of sight along a ray traced from the center of a ground cell to a detector, also referred to as the observation vector.

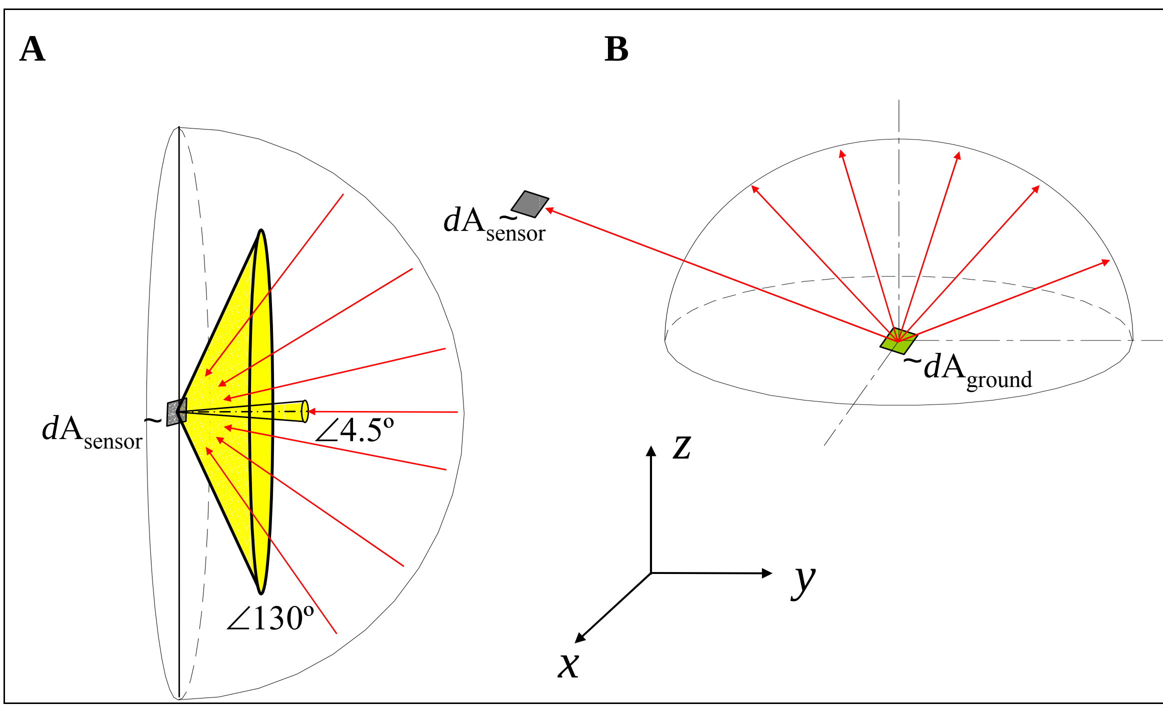

Figure 22. Illustration of spatial relationship between detectors in the (A) fire behavior packages, and (B) ground-based thermal imaging systems. The hemisphere only illustrates the 3-dimensional nature of an emitting object and does not necessarily indicate an isotropic emitter.

Analysis of Thermal Imagery on a Per-pixel Basis

Thermal infrared imagery was analyzed using custom software designed to read proprietary image file formats. Since the orientation of TIR cameras remained constant, images collected by an individual camera were inherently coregistered. Formal translations between the two TIR camera coordinate reference systems were not established. Instead, pixel to pixel mapping between midwave and longwave image coordinates was accomplished manually, and on an individual basis. Pixels of unobstructed ground cells that did not saturate in the midwave band were matched to counterpart pixels in the longwave imagery.

Digital numbers in each image file format were converted to radiant heat flux using the sensor and range specific calibration relationships. No atmospheric corrections were applied. Since background brightness temperatures were within the dynamic range of the longwave camera, a pixel adjacent to the fire perimeter was selected and tracked over the entire duration of the burn to characterize background emission. Background contributions in the midwave spectral band were determined by linearly interpreting between pixel brightness temperatures measured sporadically during the burn in a suitable dynamic range. For both TIR cameras, the time-dependent radiant heat flux (i.e., exitance) from individual fire pixel, M_f, was calculated again using Stefan Boltzmann's Law:

$$M_f = \sigma(T_f^4 - T_{back}^4) \qquad \text{Eq [2]}$$

where T_f and T_{back} were the brightness temperatures of the fire pixel and the background, respectively. Though other derivations of fire radiative heat flux are permissible for midwave measurements [Kaufman et al., 1998; Wooster et al., 2003], Stefan Boltzmann's Law was applied to facilitate comparisons between thermal imagery and *in situ* measurements (comparisons are presented in the Results section).

Analysis of Thermal Imagery on an Areal Basis

Expanding beyond a single, radiant heat flux profile for an isolated ground location, thermal imagery also offered an opportunity to measure the rate of radiative energy emitted from a collection of pixels representing an entire study area. Two additional spatial constructs were required to perform this calculation. First, the line-of-site (LOS) distance between the camera and each ground cell on the landscape was determined, and second, the perimeter of a tenth-acre circular area surrounding plot center was identified within the thermal imagery. Although transects for Brown's planar intersect method extended to 22 m to quantify fuel loadings for coarse woody debris (1000 hr), the experimental unit subset within the thermal imagery was limited to a radius of 11 m since all fuel size classes, including duff and litter layers, were sampled inside this core area. The LOS distance and plot perimeters were obtained through a georegistration procedure in which geographic coordinates were related to image coordinates via a mapping transform that remained constant for a given viewing geometry (Freeborn, et. al. 2004). Georegistration was accomplished within a GIS framework using a DEM (re-sampled to a 1m spatial resolution) in conjunction with the known geographic coordinates of the thermal camera, and the geographic and image coordinates of the pre-established ground control points. Positional accuracy for each georegistered sequence was assessed as stipulated by the National Standard for Spatial Data Accuracy (NSSDA). Horizontal accuracies were evaluated using the root mean square error (RMSE) statistic:

$$RMSE = \sqrt{\frac{\sum (X_{ind} - X_{test})^2 + (Y_{ind} - Y_{test})^2}{n}} \qquad \text{Eq [3]}$$

where X and Y were coordinate values, the subscripts *ind* and *test* identifed the independent and test data, and *n* was the number of established ground control points. The RMSE was then multiplied by 1.7308 to obtain the horizontal accuracy at a 95% confidence interval.

Straight line distances and elevational displacements relative to the camera location were used to calculate the line-of-site distance, or slant distance, at each raster element in the DEM. Also, at the same resolution as the DEM, a tenth-acre circular area was generated by imposing an 11 m buffer around plot center. The mapping transform was implemented, and these geographic grids of line-of-site (type double) and plot extent (type boolean) were converted to a pair of matrices corresponding to the dimensions of the FPA.

As with point trends, all areal calculations of fire radiative energy were performed using calibrated brightness temperatures. Given the limitations of extrapolating total radiative energy from longwave brightness temperatures, and since longwave thermal imagery was never fully georegistered, areal calculations were only performed using midwave thermal imagery. Rather than selecting a pixel outside of the burn area, the ambient temperature measured at the camera location was selected as an alternative method of characterizing the background radiant contributions.

A detection algorithm was applied to every thermal pixel within the plot region of interest to distinguish fire pixels from the non-fire background. An absolute threshold, T_{abs}, was subjectively assigned based upon the dynamic range setting of the camera during the second deployment on the Dragon WFU: 333 K for Range 2, 359 K for Range 3, 373 K for Range 4, and 425 for Ranges 5 and above. These criteria were subsequently enforced during the processing of all sequences regardless of viewing geometry. Any pixel within the study plot with a brightness temperature greater than the absolute threshold was unconditionally classified as containing fire. The purpose of the absolute threshold was to minimize the probability of a false detection (e.g., avoiding the detection of thermal anomalies such as pixels affected by solar reflection, or pixels composed of barren rock or hot gasses and water vapor). A statistical analysis was then conducted to retrieve the mean (μ_{back}) and standard deviation (σ_{back}) of the non-fire background pixels within the study plot. Three relative filters were calculated such that $T_1 = \mu_{back} + 3\sigma_{back}$, $T_2 = \mu_{back} + 2.5\sigma_{back}$, and $T_3 = \mu_{back} + 2\sigma_{back}$. A 3 × 3 relative detection filter was then passed over the absolute detects, and any pixel with a brightness temperature greater than T_1 was classified as a fire pixel. Similarly, any pixel within a 3 × 3 window centered on a first, or second, relative detect with a brightness temperature greater than T_2, or T_3, was classified as a fire pixel, respectively. In essence, the relative criteria permitted temperature thresholds to vary with changes in the dynamic range setting of the camera, and the adjacency criteria prohibited ambiguous pixels from being classified as fire in the absence of a well defined thermal gradient.

The total radiant heat transfer rate, or fire radiative power expressed in units of Watts (W), associated with each fire pixel (frp_f) within the study area was determined by multiplying the pixel area projected onto the FPA, a_f, by the radiant heat flux calculated via Stefan Boltzmann's Law:

$$frp_f = a_f \sigma (T_f^4 - T_{back}^4) \qquad \text{Eq [4]}$$

where the lower case expressions of *frp* and *a* emphasize that Eq. 2 is performed on a per pixel basis, the subscript *f* indicates that the pixel is classified as a fire pixel, *T* is the brightness temperature of the fire pixel (in Kelvin), and T_{back} is the ambient temperature measured at the camera location. The area of a fire pixel projected onto the FPA is related to the line-of-site distance and the optical system of the camera accordingly:

$$a_f = a_{j,k} = LOS_{j,k}{}^2 \times IFOV^2 \qquad \text{Eq [5]}$$

where *j* and *k* are image coordinates, and IFOV is the instantaneous field of view of each detector in the FPA. Again, the IFOV for the mid-wave thermal imaging system is 1 mrad. For each thermal image, *i*, captured at an instant in time the fire radiative power emitted from the plot, and detected by the sensor, was calculated by summing contributions from individual fire pixels:

$$FRP_i = \sum_{f=1}^{n_f} frp_f \qquad \text{Eq [6]}$$

where n_f is the total number of fire pixels detected in the study plot. The instantaneous fire area within the study plot was similarly calculated as follows:

$$A_i = \sum_{f=1}^{n_f} a_f \qquad \text{Eq [7]}$$

The total fire radiative energy (FRE) emitted from the plot, and detected by the sensor, was then calculated by integrating the temporal profile of FRP via a time-discrete summation:

$$FRE = \sum_{i=1}^{n_i} FRP_i \Delta t_i \qquad \text{Eq [8]}$$

where n_i is the total number of thermal images collected during the sequence, and Δt is the sampling interval, or the time between sequential images. Fire radiative energy is expressed in the same units as energy (i.e., Joules, J). The time-integrated fire area (i.e., m^2sec) was similarly calculated as follows:

$$\Sigma A = \sum_{i=1}^{n_i} A_i \Delta t_i \qquad \text{Eq [9]}$$

Since *FRE* and ΣA serve to reduce fire behavior within a study site to a single quantity, contributions of power, area, or duration cannot be resolved from time-integrated results.

By comparison, Brown's planar intersect method can only quantify the total, homogeneous fuel consumed per unit area and cannot resolve spatially explicit rates of fuel consumption. Therefore, time-integrated measures of FRE were more appropriately related to field surveys of total fuel consumption. Here, radiant energy density (i.e., MJ/m^2) was calculated by dividing FRE by the area of the plot projected onto the focal plane array. Rather than using the average estimate for all study plots in a deployment, the amount of fuel consumed per unit area (i.e., Kg/m^2) was quantified for only the study plots within the field of view of the thermal imager. The radiant heat yield (i.e., MJ/Kg) was thereby obtained by taking the ratio of the radiant energy density and total fuel consumption per unit area, each unit being associated within 22m of plot center.

TEAM #4—AIRBORNE REMOTE SENSING ACTIVITIES—PHIL RIGGAN

A companion report to this Final Report, prepared by Dr. Phillip Riggan, provides comprehensive details on the remote sensing platform, missions flown, and results. Included in the companion report are results from missions flown over numerous incidents not concurrently studied by the Rapid Response field campaign. These additional missions have provided opportunities for achieving significant progress and successes related to the future of airborne thermal infrared acquisitions.

Synopsis of Airborne Thermal Image Acquisition

The airborne FireMapper imagery system is flown from a fixed-wing aircraft over the incident. Although imagery was acquired for various areas of interest—interesting both to the Rapid Response Team and to the IMT—repeat imagery was acquired specifically for the Cooney Ridge sampling site during the periods for which combustion occurred[3].

The aircraft.—FireMapper imaging system is deployed on a twin engine Piper Navajo, **tail number N70Z**. The aircraft is owned and operated by the USDA Forest Service, Pacific Southwest Research Station, and both the aircraft and pilot (Bob Lamar) are FS-carded.

Air Operations.—FireMapper missions were planned, deployed, and monitored in full compliance with local/area incident aviation safety protocols. The Team apprised all levels of incident management prior to mobilizing the aircraft—these levels included the National Incident Coordination Center (NICC), the local Geographic Area Coordination Center (GACC), the Incident Management Team, and local air operations. Missions were typically flown at above-ground altitudes exceeding 5,000' (AGL), enabling effective coordination with local Temporary Flight Restrictions (TFRs) or other restrictions. The aircraft is equipped with both AM and FM frequency radios, and communicated with incident air operations and/or air attack manager(s) as required by the IMT. The mission pilot and/or lead investigator for flight activities attended pilot briefings as directed by the IMT.

Logistical Challenges.—The single-most challenging aspect of this Rapid Response project was coordination of the airborne remote sensing assets with field research

[3] See www.fireimaging.com for examples of previous and current fire imaging projects.

operations. Crew and aircraft availability were exacerbated by agency-invoked aircraft maintenance schedules, crew health, system maintenance and elective improvements, and the tactical challenges of rapid deployment.

Cooney Ridge Complex Case Study.—The first wildland fire incident studied by the Rapid Response Team was the Cooney Ridge Incident in 2003. FireMapper airborne remote sensing data were acquired throughout the period of study on this incident, and we present here a case study of those data as they relate to our other observations. The case study provided below was performed by the National Center for Landscape Fire Analysis.

Cooney Ridge Thermal Image Exploratory Analysis —Casey Teske and LLoyd Queen

Airborne thermal images and ground-based thermal images were collected coincident with ground (*in situ*) measurements during a burnout operation on the Cooney Ridge incident. In this section we present a preliminary analysis of the thermal image data, assessing both airborne and ground-based oblique imagery. The goal of this exploratory analysis is to use the results to inform further research using thermal images in wildfire settings. The objectives of this analysis are to:

- Geo-locate the data sets
- Define the area of interest within the data sets
- Calibrate temperature and energy flux within the data sets
- Assess the change of these two variables over time within data sets
- Cross-tabulate the data sets
- Determine the value of information obtained from ground-based images for enhancing or validating airborne measurements.

Data Specifications.—Thermal images for the Cooney Ridge Fire were collected on 03 September 2003 between the hours of 1500 and 1730 MST using the PSW airborne system (FireMapper™ Thermal Imaging Radiometer) and a ground-based system (Cincinnati TVS-8500). The airborne instrument was mounted on a Piper Navajo (N70Z) aircraft and overhead images were acquired in the 11.9µm wavelength region of the spectrum.[4] The ground-based instrument was placed on an opposing hill-slope, and oblique images were collected at a look-angle of 215° using the Cincinnati TVS-8500 thermal imaging camera in the 3.4µm wavelength region of the spectrum.[5] Instrument specifications for both imaging instruments are shown in Table 4.

Table 4. Instrument Specifications of the Thermal Imaging Systems used on the Cooney Ridge Fire.

[4] A companion report to this Final Report, prepared by Dr. Phillip Riggan, provides comprehensive details on the remote sensing platform, missions flown, and results.

[5] The ground-based, oblique thermal infrared system, installation, and data preparation are described in the previous section "*Team #3—Oblique Thermal Infrared.*"

	Camera Model	
	FireMapper™	**Cincinnati TVS-8500**
Manufacturer	Space Instruments	CMC Electronics
Spectral Bands	8.1 – 9.0 µm 11.4 – 12.4 µm	3.4 – 4.1 µm 4.5 – 5.1 µm
Image Dimensions	327 x 205 pixels	
Image Size	0.134 Mbytes (Uncompressed)	
Image Encoding	16 bits	14 bit
Instantaneous Field of View	1.85 milliradians	1 milliradian
Field of View	35° (Crosstrack)	14.6°
Other	11,500' AGL flight altitude	785m horizontal distance & 215° look-angle between camera & fire site
Sampling Frequency		2 frames/minute

Data Analysis and Processing.— Eleven Cincinnati TVS-8500 images (referred to as TVS from here on) were acquired from the Rocky Mountain Research Station Fire Sciences Laboratory in ESRI GRID format. The images had been projected from an oblique angle to the orthographic UTM Zone 12N projection (NAD83, GRS 1980).

Sixteen FireMapper images (referred to as PSW from here on) were downloaded during collection in near real time via satellite communications. Processed, geo-registered IMAGINE *.img* format images were acquired from the Pacific Southwest Research Station (USDA Forest Service) website (http://www.fireimaging.com/fires/2003/montana/cooneyridge/jd246/index.html) [visited online 09 January 2007].

The PSW images were then converted to grids and re-projected into UTM Zone 12N (NAD83, GRS 1980) from State Plane (Montana FIPS Zone 2500, NAD83, GRS 1980) in order to geographically "match" the images collected from the Cincinnati TVS-8500 and to determine an area of interest for further analysis.

If images from each system were coincident in time, and if the entire burnout area was captured on the PSW image, the image-pairs were used in the exploratory analysis. Although multiple images were collected, only six from each data set were ultimately used. Table 5 shows the images that were collected from each system; the shaded rows indicate image pairs excluded from the analysis.

Table 5. Image collection times for each system.

Image Pair#	PSW	TVS	TVS Temperature Specification Range	Notes
	1546		-	PSW Image ultimately not used in analysis
1	1550	15 50 05	5	
2	1554	15 54 05	5	
	1556	15 57 05	5	PSW Image does not contain entire fire; neither image ultimately used in analysis
3	1600	16 00 35	5	
4	1605	16 05 05	5	
5	1615	16 15 05	5	
6	1620	16 20 35	5	
	1626	Cannot copy this file		PSW Image ultimately not used in analysis
	1632	Cannot copy this file		PSW Image ultimately not used in analysis
	1637		5	PSW Image ultimately not used in analysis
	1643		5	PSW Image ultimately not used in analysis
	1649	16 49 13	6	Neither image ultimately used in analysis
	1655	16 55 54	4	Neither image ultimately used in analysis
	1700	17 00 28	4	Neither image ultimately used in analysis
	1712	17 11 58	4	Neither image ultimately used in analysis

Fire Masking.— A fire mask was applied to each data set. Masking was done in order to reduce the dimensionality of each data set; by setting a threshold based on temperature values, the number of pixels analyzed was constrained. Thus, only those pixels with high enough temperature values to cause selection were analyzed.

Pixels for each image were selected to be fire pixels (FIRE = True) or non-fire pixels (FIRE = False) based on two different algorithms: 1. an absolute algorithm; and 2. a relative algorithm.

1. The absolute algorithm was based solely on temperatures being greater than or equal to the lowest maximum temperature recorded for each data set for the entire time period, and ensured that the hottest pixels in the image were being analyzed.
2. The relative algorithm filtered out background radiance due to solar heating, saturation, and obstruction, and was derived by subsetting an area of the coolest background from each image and determining the mean.

The logic for the algorithms is shown in Table 6. For example, masking the TVS image captured at 1605 (TVS Range 5) with the relative algorithm resulted in a mask where only those pixels whose value was greater than or equal to 135°C were retained as "Fire Pixels" for analysis.

Table 6. Absolute and relative algorithm logic used to derive FIRE pixels from each data set. Pixels were determined to be fire pixels if these temperature conditions were true.

Algorithm	Temperature threshold	
	PSW Data Set	**TVS Data Set**
1. Absolute	$T_C \geq 300°C$	$T_C \geq 367°C$
2. Relative	$T_C \geq 50°C$	***for TVS Range 5 images (Alternative A):*** $T_C \geq 135°C$
		for TVS Range 6 images (Alternative B): $T_C \geq 106°C$
		for TVS Range 4 images (Alternative C): $T_C \geq 56°C$

Figures 23 through 28 show the results of masking algorithms on images taken at 1605 MDT of the Cooney Ridge Fire. Figure 23 shows temperatures and the area of interest in the PSW image. Results of the Relative Algorithm on the same PSW image can be seen in Figure 24 while Figure 25 shows the results of the Absolute Algorithm. In both cases, the number of pixels of interest is reduced from the image as seen in Figure 23. Figures 26 through 28 show similar results when the masking algorithms are applied to the TVS image taken at 1605 MDT (Figure 26). Figure 27 is the result of masking with the Relative Algorithm and Figure 28 is the result of masking with the Absolute Algorithm.

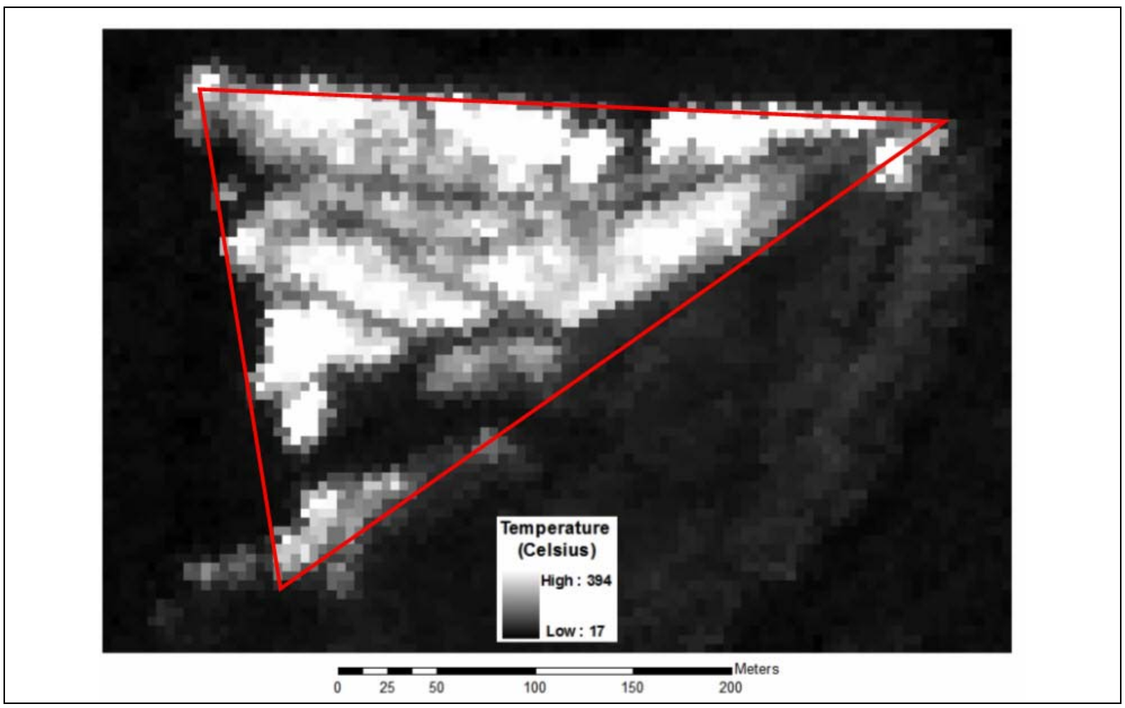

Figure 23. PSW Image showing the temperature range in degrees Celsius of the burnout operation on the Cooney Ridge Fire, acquired at 1605 MDT on 03 September 2003. The area within the Red Triangle is the approximate area of interest for the analysis.

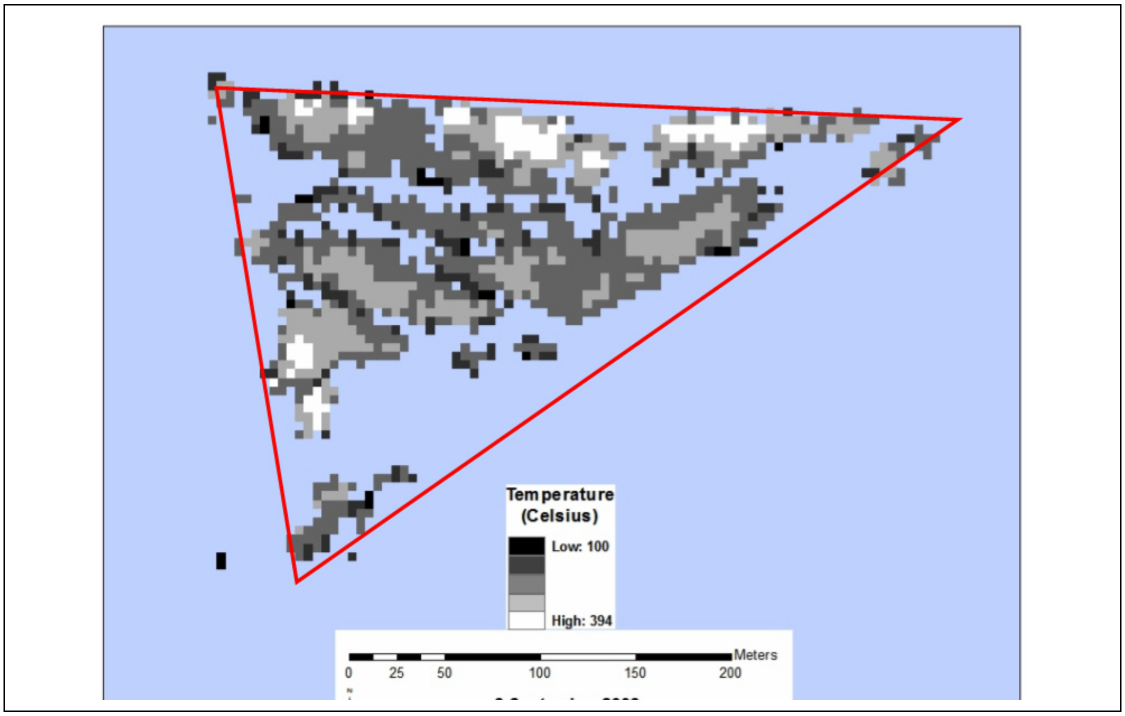

Figure 24. PSW Image as a result of masking using the Relative Algorithm.

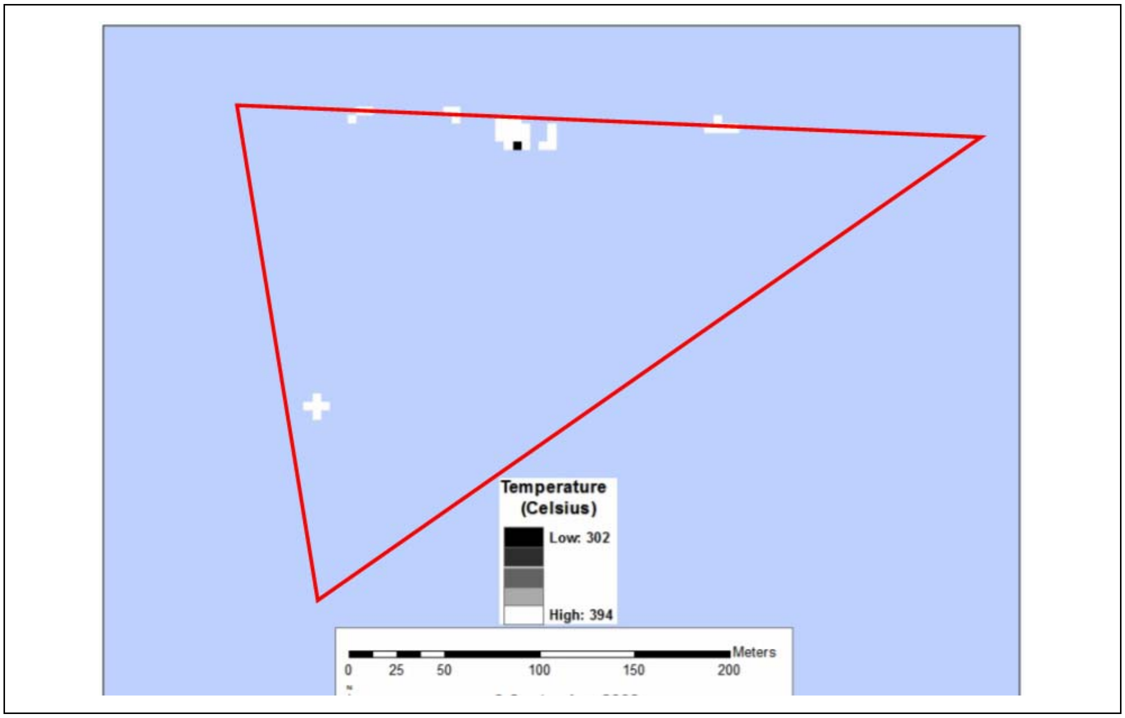

Figure 25. PSW Image as a result of masking using the Absolute Algorithm.

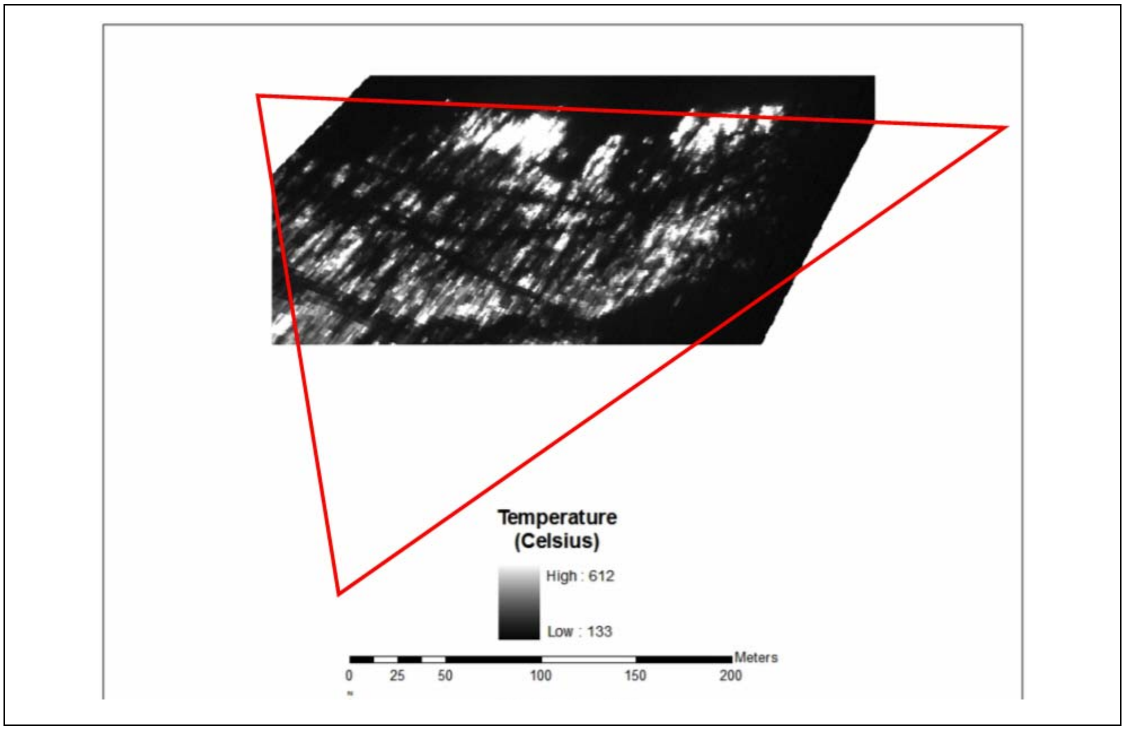

Figure 26. TVS geo-registered image showing the temperature range in degrees Celsius The area within the Red Triangle is the approximate area of interest for the analysis, and encompasses the same area as shown in Figures 23-25.

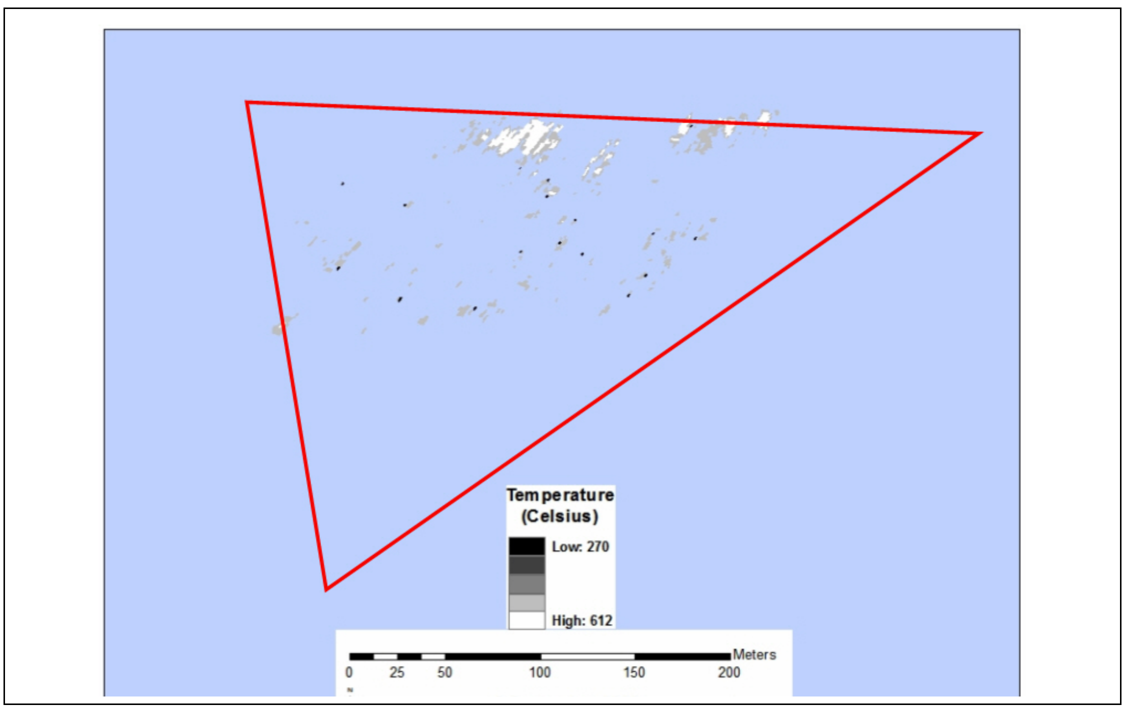

Figure 27. TVS geo-registered image as a result of masking using the Relative Algorithm.

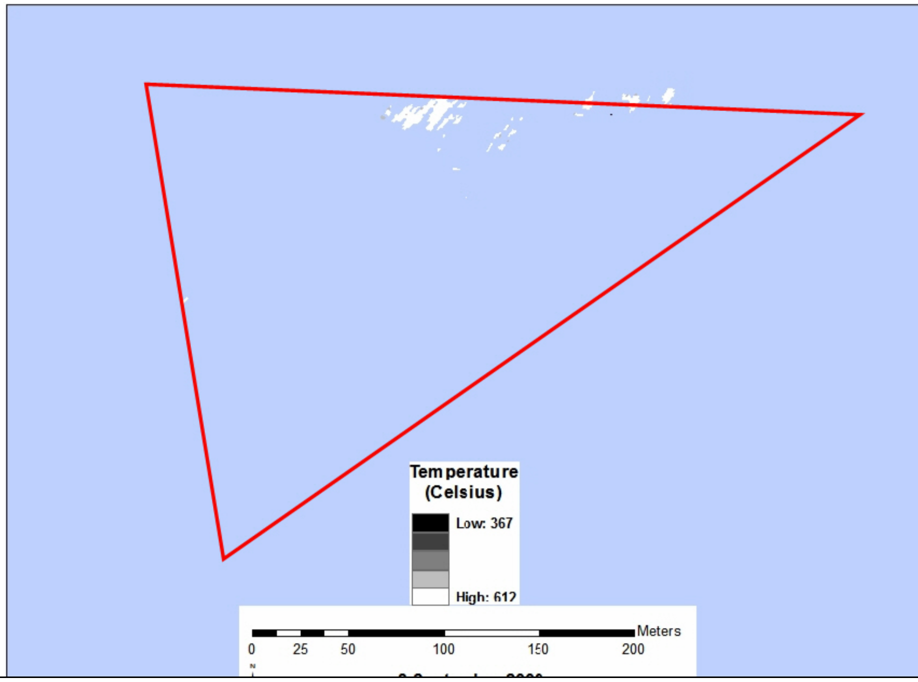

Figure 28. TVS geo-registered image as a result of masking using the Absolute Algorithm.

Thermal Calibration.— The TVS data set had three possible relative algorithms applied (as noted in Table 6), depending on the range setting for the camera at the time of image acquisition(s). The camera settings for minimum and maximum temperature specification ranges were changed during image acquisition according to the following:

Range 4: 200 - 450°C (Time: 1650 – 1711)

Range 5: 300 - 600°C (Time: 1550 -- 1620)

Range 6: 500 - 900°C (Time: 1649)

The values in each data set represented temperature in degrees Celsius and ultimately needed to be converted into energy equivalents in Watts per square meter (W/m^2). The following equations were used to convert the Celsius temperature values to energy equivalents:

$$T_K = T_C + 273.15 \qquad \text{Eq [10]}$$

$$W_\lambda = \sigma T_K^4 \qquad \text{Eq [11]}$$

where T_C is temperature in °C, T_K is temperature in Kelvin (K), σ is the Stefan-Boltzmann constant (5.67 x 10^{-8} $Wm^{-2}K^{-4}$), and W_λ is the energy equivalent in W/m^2.

Equations 10 and 11 were used on both the PSW and the TVS data and follow flux formulations used by other members of the project science team.[6]

Exploratory Statistics.— Minimum, maximum, mean, range, standard deviation, and variance were calculated for all "masked" images in each data set individually to show variability (Table 7). Because not all TVS images had the same camera range specifications, all but the initial seven TVS images collected in TVS Range 5 between 1550 and 1620 were dropped from further analysis (see Table 5). This was ultimately reduced to six images as the PSW image collected at 1556 did not contain the whole fire. The "*A*", "*B*", and "*C*" in the TVS Relative section correspond to the "Alternatives," as labeled in Table 6.

Box plots of temperature statistics grouped by time (Figure 29), as well as energy equivalent statistics grouped by time (Figure 30) were created in order to show the variability through time of the masked data sets. As can be seen in Figure 29, independent of the masking algorithm, mean temperature within a data set through time does not appear to change significantly. Likewise, the mean energy equivalent calculated using Equation 11 does not appear to change significantly within a data set (Figure 30). In all cases, the TVS data had a larger range of temperature values, as well as higher temperature values in general.

Because the temperature ranges were so different between the two data sets, a cross-tabulation between them has not been done, nor has a complete analysis as to the value of using the ground-based imagery to validate or enhance the airborne imagery been done.

Future Work.— Some questions that may direct future research in wildfire using thermal imagery are:

- Can ground-based thermal infrared images in a mid-wave infrared wavelength be used to validate or enhance airborne thermal infrared image acquisitions in long-wave infrared?
- How does the timing of the image acquisition affect the ultimate temperature values?
- How does distance from the heat source affect the ultimate temperature values?
- How does angle of acquisition affect the ultimate temperature values?
- How does pixel resolution affect the ultimate temperature values?
- How does projecting an oblique image into an orthographic projection affect the ultimate temperature values?
- Can thermal imagery be used to determine fuel consumption?

[6] See section on ***"Team #3—Oblique Thermal Infrared."***

Table 7. Descriptive statistics of temperature (°C) values in each data set for all "masked" images.

Data			Descriptive Statistic						
Data	**Algorithm**	**Time**	**N**	**Range**	**Min.**	**Max.**	**Mean**	**Std. Dev.**	**Variance**
PSW	**Absolute**	***1546 - 1712***	*240*	*250*	*300*	*550*	*347.091*	*43.23953*	*1869.657*
		1546	11	46	301	347	319.454	17.13688	293.673
		1550	18	151	305	456	350.277	46.8487	2194.801
		1554	27	188	301	489	383.074	57.36853	3291.148
		1600	17	107	301	408	350.705	33.19594	1101.971
		1605	21	92	302	394	333	26.94068	725.8
		1615	17	67	300	367	327.235	19.75958	390.441
		1620	13	105	307	412	335.615	32.00401	1024.256
		1626	2	34	312	346	329	24.04163	578
		1632	1	0	306	306	306	-	-
		1637	5	25	309	334	323	11.97915	143.5
		1643	25	247	303	550	384.84	62.11326	3858.057
		1649	37	107	302	409	352.837	34.75351	1207.806
		1655	30	61	300	361	329.133	18.17488	330.326
		1700	15	47	302	349	322	16.39251	268.714
		1712	1	0	300	300	300	-	-
PSW	**Relative**	***1546 - 1712***	*2743*	*450*	*100*	*550*	*197.444*	*69.84438*	*4878.238*
		1546	344	247	100	347	192.011	60.58105	3670.064
		1550	176	356	100	456	200.306	73.09256	5342.522
		1554	195	389	100	489	213.671	86.69127	7515.376
		1600	180	308	100	408	200.922	70.76118	5007.145
		1605	174	294	100	394	200.413	70.84307	5018.741
		1615	179	267	100	367	198.139	65.54437	4296.065
		1620	178	312	100	412	196.584	64.81705	4201.25
		1626	152	246	100	346	181.190	52.73132	2780.592
		1632	139	206	100	306	173.741	48.16282	2319.657
		1637	148	234	100	334	180.810	54.97363	3022.1
		1643	175	450	100	550	209.897	89.71795	8049.311
		1649	193	309	100	409	215.471	83.79713	7021.959
		1655	191	261	100	361	209.691	73.24892	5365.404
		1700	171	249	100	349	197.380	65.72556	4319.849
		1712	148	200	100	300	179.391	50.2977	2529.859
TVS	**Absolute**	***1550-1711***	*1144*	*327*	*367*	*694*	*469.579*	*75.19225*	*5653.875*
		1550	115	327	367	694	479.939	91.17934	8313.672
		1554	180	321	367	688	488.372	84.3885	7121.419
		1557	205	298	367	665	488.448	78.13992	6105.847
		1600	163	297	367	664	468.098	66.11393	4371.052
		1605	157	245	367	612	457.394	60.05497	3606.599
		1615	146	257	367	624	456.013	63.41369	4021.296
		1620	128	256	367	623	464.632	70.71256	5000.266
		1649	29	116	368	484	404.517	28.70244	823.83
		1655	13	41	368	409	386.384	14.06259	197.756
		1700	7	50	368	418	383.428	19.18208	367.952
		1711	1	0	367	367	367	-	-
TVS	**Relative**	***1550-1711***	*2788*	*582*	*112*	*694*	*348.854*	*123.91179*	*15354.133*
	A	**1550**	210	424	270	694	406.361	107.10855	11472.242
	A	**1554**	277	418	270	688	428.711	107.34623	11523.213
	A	**1557**	302	395	270	665	433.702	103.66383	10746.19
	A	**1600**	259	394	270	664	412.351	91.28614	8333.159
	A	**1605**	254	342	270	612	404.161	84.4347	7129.219
	A	**1615**	243	354	270	624	400.921	85.50379	7310.899
	A	**1620**	283	411	212	623	368.438	104.98051	11020.907
	B	**1649**	273	372	112	484	252.153	86.13378	7419.028
	C	**1655**	243	297	112	409	236.728	76.32564	5825.604
	C	**1700**	231	306	112	418	230.108	72.17389	5209.071
	C	**1711**	213	255	112	367	220.056	65.17195	4247.384

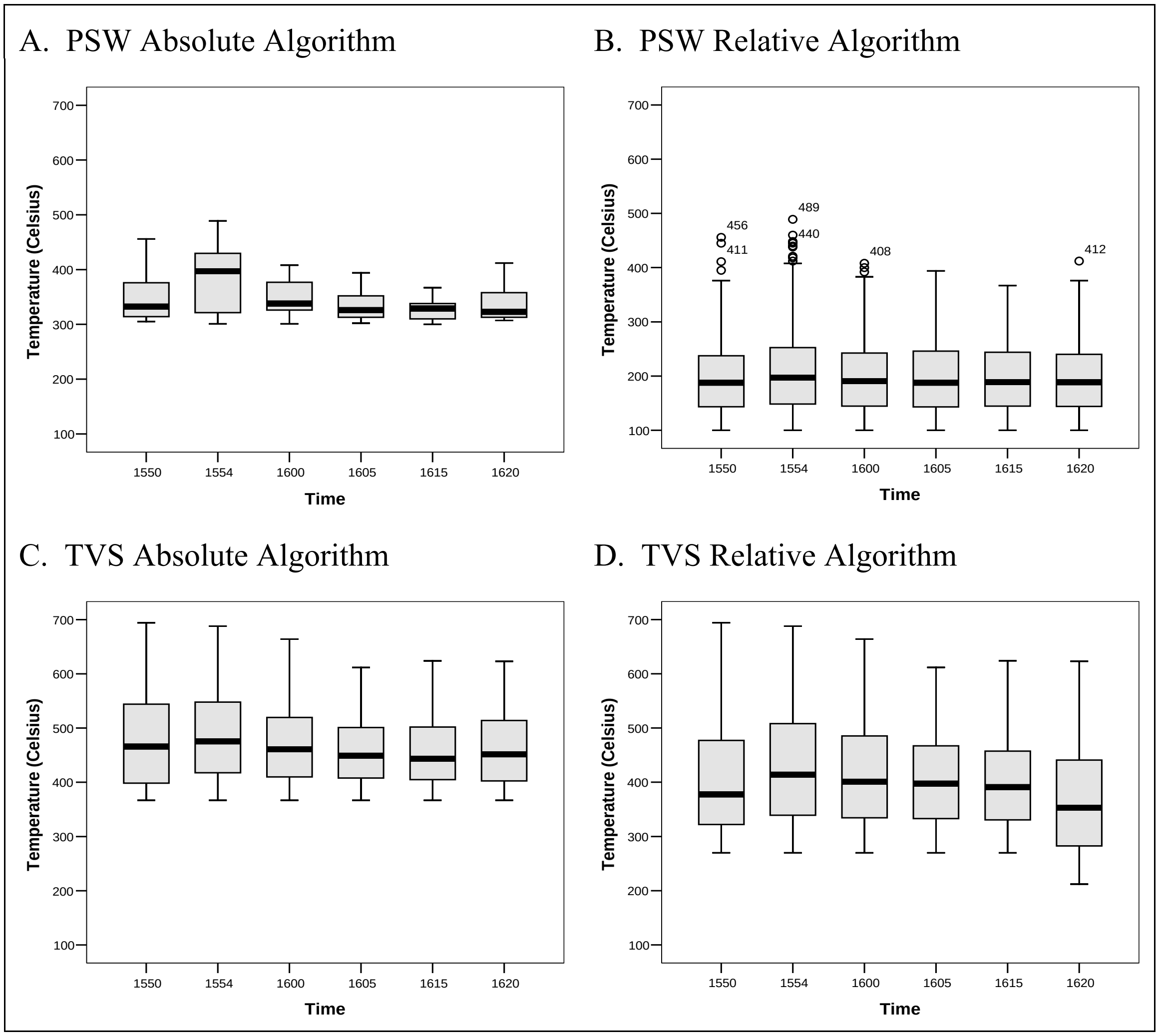

Figure 29. Box plots of **temperature statistics**, grouped by time. Plots indicate the median, 25th and 75th percentiles, and minimum and maximum values that are not statistical outliers. Extreme values are marked with asterisks, and outliers are marked with circles. Box plots are given for the PSW absolute algorithm (A), PSW relative algorithm (B), TVS absolute algorithm (C), and TVS relative algorithm (D).

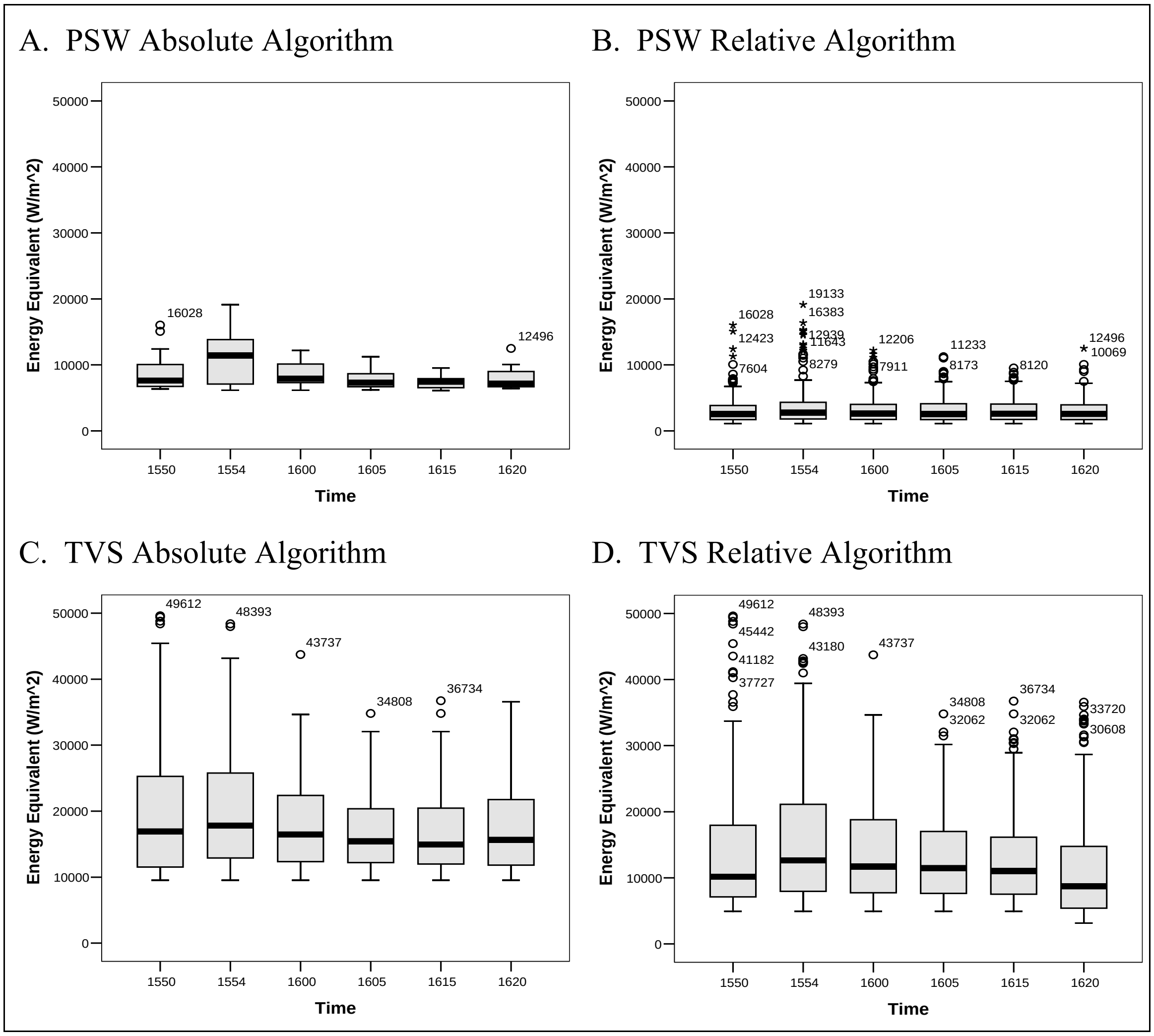

Figure 30. Box plots of **energy equivalent statistics**, grouped by time. Plots indicate the median, 25th and 75th percentiles, and minimum and maximum values that are not statistical outliers. Extreme values are marked with asterisks, and outliers are marked with circles. Box plots are given for the PSW absolute algorithm (A), PSW relative algorithm (B), TVS absolute algorithm (C), and TVS relative algorithm (D).

TEAM #5—MODIS (SATELLITE) FIRE DETECTION AND MAPPING—BRYCE NORDGREN

The MODIS instrument is operating on both the Terra and Aqua spacecraft. It has a viewing swath width of 2,330 km and views the entire surface of the Earth every one to two days. Its detectors measure 36 spectral bands between 0.405 and 14.385 µm, and it acquires data at three spatial resolutions -- 250m, 500m, and 1,000m. Band configurations as well as derived products have been chosen to support fire-detection and fire-related applications. MODIS is an instrument which operates at an entirely different scale than plot-level and aircraft measurements. It is designed to cover the entire globe twice daily, whereas aircraft and *in-situ* measurements trade off the synoptic view for higher spatial or temporal resolution.

The Missoula Fire Sciences Laboratory operates a direct-broadcast receiving station with which they acquire and analyze MODIS data directly from the satellite. The inclusion of MODIS in this study was predicated on concurrent observations of the same fire phenomenon at multiple spatial scales. Comparisons would then be made between *in-situ* instruments, radiometrically calibrated ground and airborne thermal imagers, and MODIS. The intention was to generate a multi-stage data set where spatially coarse measurements leverage simultaneous measurements of greater detail in order to determine the relationship of uncertainty to spatial resolution.

For reasons of safety and logistics, the execution of the field component of this project revolved around relatively small portions of larger fires, often coincident with "burnout" operations which were to occur at known locations and times. This allowed the safe and efficient collection of data for all components except MODIS. MODIS is not capable of fully resolving the burns incorporated in this study either temporally or spatially. Availability of ground crews dictated the time of ignition, the small size of the burn severely limited the duration, and MODIS was not overhead coincident with the time that complementary ground measurements were being taken. Therefore, data from the MODIS instrument were not available to contribute directly to this rapid response investigation, due largely to the fact that its inflexible schedule would not adapt to constraints imposed by safety and logistics.

Two indirect contributions to this Rapid Response Project relating to the development of new MODIS fire products are presented in the Results section of this report. The first is development of a method to aggregate individual pixels into a fire perimeter—this development effort was shared with JFSP Project 01-1-5-03. We also present (in the Findings section of this report) lessons learned about the attempt to include a polar orbiter are presented as advice for future research efforts.

TEAM #6—GEODATABASE DESIGN AND IMPLEMENTATION—LEE MACHOLZ

The Rapid Response Geodatabase Project has direct and immediate relevance to any multi-team or multi-disciplinary study for which data and observations are made and must be shared. The geodatabase developed for this project was intended as a model from which other researchers can benefit. An independent, comprehensive "Final

Deliverables Package" has been prepared by the National Center for Landscape Fire Analysis. This package includes an executive summary and 23 appendices. The appendices present all phases and intermediate products from the project as well as several published manuscripts. Of particular significance to future developers of geodatabases is Appendix H of the Final Deliverables Package —"Geodatabase use in fire sciences research: a protocol for development."

This "Final Deliverables Package" accompanies this final report under separate cover. The following is excerpted from the executive summary as brief synopsis of the geodatabase project objectives, evolution, and methods. Additional results and recommendations are provided in the Results section of this report.

Rapid Response Geodatabase Project Executive Summary

A specific objective of this Rapid Response project was the development of a database that would be common to several associated rapid response projects, thus exploiting the linkages between the projects and allowing researchers to share data. The JFSP BOG requested that the database be designed to include the following rapid response projects: Hardy and Riggan, (*Demonstration and Integration of Systems for Fire Remote Sensing, Ground-Based Measurement, and Fire Modeling*); and Morgan and others (*Assessing the Causes, Consequences and Spatial Variability of Burn Severity: A Rapid Response Approach*). Principal Investigator Hardy approached the National Center for Landscape Fire Analysis (NCLFA) at the University of Montana's College of Forestry and Conservation to lead the effort of designing a centralized database. The NCLFA undertook this project as an opportunity to demonstrate recent advancements in geospatial database design and GIS technology and the advantages of a shared data architecture for fire sciences research.

The rapid response geodatabase project proceeded through two phases. The primary goal of phase I was to demonstrate the design, development, and implementation of a centralized geodatabase that incorporated all data supporting the rapid response research projects identified by the JFSP board of governors. An additional goal of phase I was to document the design and development lifecycle of this geodatabase as a protocol that could be used as a guide for this type of work in the future.

Phase I of the rapid response geodatabase project was initiated in September of 2003 and concluded in August of 2004. During phase I of the rapid response geodatabase project, staff at the NCLFA worked with the rapid response project investigators, their staff, and consultants from ESRI to design, develop, and implement an enterprise geodatabase based on ESRI's ArcSDE technology. The decision to use ESRI technology as the foundation for the project was made for two primary reasons: First, because the rapid response projects had both spatial and tabular data components it was desirable to store all of the data in one data structure and ESRI is the industry leader in geospatial database technology. Second, ESRI applications were determined to be available to all project participants, thus the resulting geodatabase would be accessible by all project participants.

The rapid response geodatabase design process continued with the NCLFA hosting a data committee workshop with the intent of determining the data elements to be included in the geodatabase and the functionality required of the final system. During this workshop, all of the project investigators and their associated research teams gathered at the USFS Missoula Fire Sciences Laboratory for two days of discussion about their data and the concept of a centralized geodatabase. The workshop was a success in several ways:

- It allowed the researchers to meet face-to-face and describe their data and collection methods to each other.
- It allowed the NCLFA staff to determine the data that would need to be included in the geodatabase.
- It allowed the NCLFA staff to determine the functionality that the researchers would require in order to utilize the data within the geodatabase for their project work.
- It allowed the NCLFA to communicate the intent of the rapid response geodatabase project and get the researchers to buy into the concept.

One of the most notable outcomes of the data committee workshop was the increased level of communication between the various research teams. Prior to the workshop, the teams had a general idea that their peers were collecting this or that type of data and that they could maybe use each others' data in the future. During the workshop, the researchers had the opportunity to describe their datasets to each other, really talk about how they could collaborate to further their research efforts, and understand how a shared geodatabase would support that collaboration.

After the data committee workshop, the rapid response geodatabase project moved into the development stage. The geodatabase development process included a series of modeling efforts in which the geodatabase structure was refined from a conceptual model to the final geodatabase implemented within ESRI's ArcSDE and Microsoft's SQL Server. The geodatabase was initially populated with the rapid response dataset collected in 2003 at the Cooney Ridge fire. The ArcSDE platform allowed the viewing, editing, and dissemination of data from the geodatabase through several ESRI desktop applications. However, once the rapid response geodatabase was implemented, several issues arose with the researcher's ability to access the geodatabase.

The rapid response geodatabase was hosted on servers located at the offices of the NCFLA. In theory, researchers could connect to the geodatabase from remote locations using ESRI's ArcGIS Desktop applications. In reality, due to network speeds and firewalls, remote connections to the geodatabase were exceedingly slow if they could be made at all. Thus, at the end of phase I of the rapid response geodatabase project, the NCLFA had successfully demonstrated the design and development of a centralized geodatabase structure for multiple research teams, but the implementation of that geodatabase was essentially limited to the NCLFA's local computing network.

Phase II of the rapid response geodatabase project was initiated in June of 2005 and concluded in November of 2006. The primary goal of phase II was to remedy the implementation issues encountered in phase I of the project and provide the participating researchers with a custom web-based user interface to the rapid response geodatabase.

Staff at the NCLFA began phase II by performing user assessments with each research team in order to better understand the user's needs for data entry, viewing, and retrieval. The geodatabase structure was then evaluated to ensure that it still met all the data and functionality requirements of the users. The user assessments were then used to inform the design and development of an application that would provide data entry, data viewing, and data retrieval functionality via the Internet. Upon completion of development, the rapid response geodatabase web application consisted of a data entry module for the Primary Investigators and a data viewing module for the researchers and the public through which they could view and retrieve both spatial and tabular data. In addition, a desktop application was developed with data entry modules for four of the seven participating research teams.

PROJECT RESULTS

FIELD CAMPAIGNS

The Rapid Response Team mobilized to seven individual wildland fire incidents during the period 2003 through 2006. Eleven instrument deployments were achieved at those incidents (Table 8). Our initial 2003 proposal for a one-year “proof-of-concept” exploration proposed mobilization to “two or three wildland fire incidents in different ecosystems or regions.” Two were accomplished in 2003. A proposal to extend the study for two additional years was funded by JFSP, with the objective to complete “two additional deployments of the Rapid Response Team…” No mobilizations were accomplished during the 2004 fire season, resulting in a no-cost extension through December, 2006, which authorized “two additional full deployments of the Rapid Response Team.”

Of the seven mobilizations, this final report addresses three: Cooney Ridge, Dragon (two deployments), and Tripod (two deployments). As shown in Table 8, logistics varied such that the “richness” of instrumentation, observations, and data acquisition varied among the seven mobilizations, and those reported here were the most complete and have the best quality control.

Table 8. The Rapid Response Team mobilized to seven individual wildland fire incidents during the period 2003 through 2006. Ten instrument deployments were achieved at these incidents.

Measurement Activity		Incident Name Location, Deployment #, Date											
		Cooney Ridge (MT)	*TCEF Rx* (MT)	*Dragon WFU* (AZ)		*I90 Complex* (MT)			*Selway-Salmon* (MT)		*Valley Road* (ID)	*Tripod Complex* (WA)	
		#1 (9/03)	#1 (10/03)	#1 (7/05)	#2 (7/05)	#1 (8/05)	#2 (8/05)	#3 (8/05)	#1 (9/05)	#2 (9/05)	n/a (9/05)	#1 (8/06)	#2 (8/06)
In-situ plot instruments	Auto.Envir.Sentry	X	X	X	X	- -	- -	X	X	- -	- -	X	X
	Fire Behavior Flux	X	X	X	X	X	X	X	X	X	- -	X	X
	Video	X	X	X	X	X	X	X	X	X	- -	X	X
Site characterization		X	X	X	X	- -	- -	X	X	- -	- -	X	X
Oblique thermal infrared	3-5 µm	X	X	X	X	X	X	X	X	X	- -	X	X
	8-12 µm	- -	- -	X	X	X	X	X	X	X	- -	X	X
Airborne imagery *		PSW	PSW	- -	- -	- -	- -	- -	RIT	RIT	- -	- -	- -
MODIS		X	X	- - - - - - - - - - - - - - - - Archived - - - - - - - - - - - - - - - -									
GeoDatabase Implementation		X	- - - - - - - - - - - GeoDatabase in development - - - - - - - - - - -									(10/06)	(10/06)

* Airborne imagery: PSW—Pacific Southwest Research Station, *FireMapper* system;
RIT—Rochester Institute of Technology, *WASP* system.

We excluded four mobilizations:

1. The TCEF Rx (prescribed burn) was at the very wettest extreme of prescribed conditions, resulting in insufficient combustion and energy to support further analysis (even though this was only one of two for which PSW airborne remote sensing data were acquired [Table 8]).

2. The I90 Complex deployments had two deployments with too small a spatial extent to exercise our analyses; fire on a third deployment was prematurely terminated by that year's "season ending" precipitation.

3. The Selway-Salmon WFU deployments experienced marginal fire behavior and insufficient energy release to warrant further analyses for this report. We did successfully deploy an airborne remote sensing system operated by our Rochester Institute of Technology (RIT) collaborator (the WASP system); this accomplishment contributed significantly to the RIT development program.

4. The Valley Road Complex experienced fire behavior and complexities which precluded safe insertion of our Teams into the operational environment.

These excluded mobilizations, while extremely beneficial as learning and exploratory activities, are not addressed further in this report; however, they will be examined later by individual sub-teams for subsequent "data mining."

The only mobilization for which airborne remote sensing data will be presented was the Cooney Ridge incident (Table 8), for which the Pacific Southwest (PSW—USDA Forest Service) system (FireMapper) successfully acquired and processed time-series thermal infrared imagery.

The Geodatabase is fully populated with all available data from the Cooney Ridge (one deployment) and Tripod Complex (two deployments) incidents.

VEGETATION, FUELS, AND SITE CHARACTERISTICS

Cooney Ridge—Summary

The Cooney deployment was located approximately 16 miles (26 km) southeast of Missoula, MT on privately owned timberland. Average elevation of the site was 4624 ft (1409 m). The slope was 30%, with a northeast aspect. The stand was dominated by subalpine fir (*Abies lasiocarpa*) and Douglas-fir (*Pseudotsuga menziesii*), with a small component of western larch (*Larix occidentalis*). The understory primarily consisted of ninebark (*Physocarpus malvaceus*) and snowberry (*Symphoricarpos albus*). The area burned on 9/3/2003 at approximately 1400. Scorch heights were greater than tree heights (+85 ft (26 m)). All trees on the plot were killed, except the one western larch. The fire consumed 82% of the dead and down woody fuel and 96% of the forest floor. Pre-burn and post-burn photos of the Cooney Ridge site are shown in Figure 31 and Figure 32, respectively.

Figure 31. Cooney site, pre-burn.

Figure 32. Cooney site, post-burn.

Dragon WFU—Summary

Dragon #1.—Dragon deployment #1 was located approximately 6 miles (10 km) north of the North Rim in Grand Canyon National Park. Average elevation of the site was 8180 ft (2494 m). The slope was 35%, with a north aspect. The stand was dominated by Engelmann spruce (*Picea engelmannii*). Aspen (*Populus tremuloides*) were scattered throughout the area, although most stems were declining and many were dead. The understory was sparse and primarily consisted of Engelmann spruce and white fir (*Abies concolor*) seedlings. The area burned on 7/17/2005 at approximately 1315. Scorch heights were greater than tree heights (+90 ft (27 m)) for the majority of the area, especially where the instruments were located. Fire intensity was lower on the eastern portion of the area, with scorch heights averaging 20-40 ft (6-12 m). The fire consumed 70% of the dead and down woody fuel and 54% of the forest floor. Pre-burn and post-burn photos of the Dragon #1 site are shown in Figure 33 and Figure 34, respectively.

Figure 33. Dragon #1 site, pre-burn.

Figure 34. Dragon #1 site, post-burn.

Dragon #2.— Dragon deployment #2 was located approximately 6 miles (10 km) north of the North Rim in Grand Canyon National Park. Average elevation of the site was 8280 ft (2524 m). The slope was 57%, with an east aspect. The stand was dominated by ponderosa pine (*Pinus ponderosa*), with a small component of Engelmann spruce and aspen. The understory was very sparse, mostly just ponderosa pine needle litter. The area burned on 7/18/2005 at approximately 1330. Scorch heights averaged 30-60 ft (9-18 m) for the majority of the area. Crown volume scorch was generally greater than 90% for all trees. The majority of trees survived the fire however. The fire consumed 36% of the dead and down woody fuel and 82% of the forest floor. Pre-burn and post-burn photos of the Dragon #2 site are shown in Figure 35 and Figure 36, respectively.

Figure 35. Dragon #2 site, pre-burn.

Figure 36. Dragon #2, post-burn.

Tripod Complex—Summary

Tripod #1.— Tripod deployment #1 was located approximately 11 miles (18 km) southwest of Conconully, WA on the Okanogan National Forest. Average elevation of the site was 4200 ft (1280 m). The slope was 46%, with an east aspect. The stand overstory was dominated by western larch and ponderosa pine, with a mid-story of Douglas fir. The understory primarily consisted of snowberry and lupine. The area burned on 8/24/2006 at approximately 1250. Scorch heights averaged 60 ft (18 m) for the majority of the area. All Douglas-fir trees were killed by the fire, but the western larch and ponderosa pine survived. The fire consumed 61% of the dead and down woody fuel and 45% of the forest floor. Pre-burn and post-burn photos of the Tripod #1 site are shown in Figure 37 and Figure 38, respectively.

Figure 37. Tripod #1 site, pre-burn.

Figure 38. Tripod #1 site, post-burn.

Tripod #2.— Tripod deployment #2 was located approximately 11 miles (18 km) southwest of Conconully, WA on the Okanogan National Forest. Average elevation of the site was 4330 ft (1320 m). The slope was 41%, with an east aspect. The stand overstory was dominated by western larch and ponderosa pine, with a mid-story of Douglas fir. The understory primarily consisted of snowberry and Douglas-fir saplings. The area burned on 8/24/2006 at approximately 1245. No post-burn data was collected due to several dangerous snags in the area.

Measurement and Observation Summary Tables—All Sites

All measured pre- and post-burn site data relating to vegetation and fuels, including derived values such as fuel consumption, are presented here for all sites in six common data tables: 1. Stand characteristics by site and deployment (Table 9); 2. Stand characteristics by species, site and deployment (Table 10); 3. Cover by life form by site and deployment (Table 11); 4. Fuel moistures by site and deployment (Table 12); 5. Fuel loadings and consumption, by site and deployment (Table 13); 6. Aggregated fuel loadings and consumption, by site and deployment (Table 14).

Table 9. Stand characteristics by site and deployment.

Incident	Deployment	Sampling Event	Live Trees	Basal Area	Avg. Live Crown Base Height	Avg. Height	Quadratic Mean Diameter	Saplings	Seedlings	Total Live Trees	Snags
			per acre (per ha)	sq.ft./acre (sq.m./ha)	ft (m)	ft (m)	in (m)	per acre (per ha)	per acre (per ha)	per acre (per ha)	per acre (per ha)
Cooney	1	Pre	70 (173)	30.6 (7)	6.7 (2)	59.4 (18.1)	9 (22.7)	110 (271.8)	3700 (9142.7)	3880 (9587.5)	0 (0)
		Post	10 (24.7)	7.1 (1.6)	14 (4.3)	85 (25.9)	11.4 (29)	0 (0)	600 (1482.6)	610 (1507.3)	60 (148.3)
		Difference	-60(-148.3)	-23.5 (-5.4)	7.3 (2.3)	25.6 (7.8)	2.4 (6.3)	-110 (-271.8)	-3100 (-7660.1)	-3270 (-8080.2)	60 (148.3)
Dragon	1	Pre	290 (716.6)	153.85 (35.3)	15.4 (4.7)	49 (15.0)	(25.35)	25 (61.8)	650 (1606.2)	965 (2384.6)	80 (197.7)
		Post	160 (395.4)	87.65 (20.1)	29.5 (9)	53.8 (16.4)	10.9 (27.6)	10 (24.7)	50 (123.6)	220 (543.6)	175 (432.4)
		Difference	-130(-321.2)	-66.2 (-15.2)	14.1 (4.4)	4.8 (1.4)	1.0 (2.25)	-15 (-37.1)	-600 (-1482.6)	-745 (-1840.95)	95 (234.7)
	2	Pre	180 (444.8)	178.5 (41.0)	14.2 (4.3)	52.4 (15.9)	14.1 (35.8)	6.7 (16.5)	33.3 (82.4)	220 (543.6)	3.3 (8.2)
		Post	140 (345.9)	165.3 (38.0)	34.0 (10.4)	54.0 (16.4)	14.8 (37.6)	6.7 (16.5)	33.3 (82.4)	180 (444.8)	46.7 (115.3)
		Difference	-40 (-98.8)	-13.2 (-3)	19.8 (6.1)	1.6 (0.5)	0.7(1.8)	0 (0)	0 (0)	-40 (-98.8)	43.3 (107.1)
Tripod	1	Pre	180 (444.8)	103.9 (23.8)	19 (5.8)	51.6 (15.7)	10.3 (26.1)	10 (24.7)	0 (0)	190 (469.5)	0 (0)
		Post	110 (271.8)	79.3 (18.2)	0 (0)	63.8 (19.4)	11.5 (29.2)	10 (24.7)	0 (0)	120 (296.5)	70 (173)
		Difference	-70(-173)	-24.6 (-5.6)	-19 (-5.8)	12.2 (3.7)	1.2 (3.1)	0 (0)	0 (0)	-70 (-173)	70 (173)
	2	Pre	130 (321.2)	137.7 (31.6)	16 (4.9)	63 (19.2)	13.9 (35.4)	150 (370.6)	0 (0)	280 (691.9)	0 (0)
		Post	----	----	----	----	----	----	----	----	----
		Difference	----	----	----	----	----	----	----	----	----

Table 10. Stand characteristics by species, site and deployment.

Incident	Deployment	Species	Sampling Event	Live Trees	Basal Area	Avg. Live Crown Base Height	Avg. Height	Quadratic Mean Diameter	Saplings	Seedlings	Total Live Trees	Snags
				per acre (per ha)	sq.ft./acre (sq.m./ha)	ft (m)	ft (m)	in (m)	per acre (per ha)	per acre (per ha)	per acre (per ha)	per acre (per ha)
Cooney	1	Subalpine fir	Pre	40 (98.8)	12.1 (2.8)	5.2 (1.6)	54 (16.5)	7.4 (18.9)	80 (197.7)	1400 (3459.4)	1520 (3755.9)	0 (0)
			Post	0 (0)	0 (0)	0 (0)	0 (0)	0 (0)	0 (0)	300 (741.3)	300 (741.3)	40 (98.8)
			Difference	-40 (-98.8)	-12.1 (-2.8)	-5.2 (-1.6)	-54 (-16.5)	-7.4 (-18.9)	-80 (-197.7)	-1100 (-2718.1)	-1220 (-3014.6)	40 (98.8)
		Western larch	Pre	10 (24.7)	7.1 (1.6)	14 (4.3)	85 (25.9)	11.4 (29)	0 (0)	0 (0)	10 (24.7)	0 (0)
			Post	10 (24.7)	7.1 (1.6)	0 (0)	85 (25.9)	11.4 (29)	0 (0)	0 (0)	10 (24.7)	0 (0)
			Difference	0 (0)	0 (0)	-14 (-4.3)	0 (0)	0 (0)	0 (0)	0 (0)	0 (0)	0 (0)
		Engelmann spruce	Pre	0 (0)	0 (0)	0 (0)	0 (0)	0 (0)	20 (49.4)	900 (2223.9)	920 (2273.3)	0 (0)
			Post	0 (0)	0 (0)	0 (0)	0 (0)	0 (0)	0 (0)	0 (0)	0 (0)	0 (0)
			Difference	0 (0)	0 (0)	0 (0)	0 (0)	0 (0)	-20 (-49.4)	-900 (-2223.9)	-920 (-2273.3)	0 (0)
		Douglas-fir	Pre	20 (49.4)	11.5 (2.6)	6 (1.8)	57.5 (17.5)	10.2 (26)	10 (24.7)	1400 (3459.4)	1430 (3533.5)	0 (0)
			Post	0 (0)	0 (0)	0 (0)	0 (0)	0 (0)	0 (0)	300 (741.3)	300 (741.3)	20 (49.4)
			Difference	-20 (-49.4)	-11.5 (-2.6)	-6 (-1.8)	-57.5 (-17.5)	-10.2 (-26)	-10 (-24.7)	-1100 (-2718.1)	-1130 (-2792.2)	20 (49.4)
Dragon	1	White fir	Pre	0 (0)	0 (0)	0 (0)	0 (0)	0 (0)	0 (0)	150 (370.7)	150 (370.7)	0 (0)
			Post	0 (0)	0 (0)	0 (0)	0 (0)	0 (0)	0 (0)	0 (0)	0 (0)	0 (0)
			Difference	0 (0)	0 (0)	0 (0)	0 (0)	0 (0)	0 (0)	-150 (-370.7)	-150 (-370.7)	0 (0)
		Engelmann spruce	Pre	215 (531.3)	131.1 (30.1)	10 (3.1)	49.2 (15)	10.8 (27.3)	15 (37.1)	450 (1112)	680 (1680.3)	15 (37.1)
			Post	125 (308.9)	74.2 (17.1)	27.9 (8.6)	53.9 (16.4)	11.1 (28.2)	0 (0)	50 (123.6)	175 (432.4)	100 (247.1)
			Difference	-90 (-222.4)	-56.9 (-13)	17.9 (5.5)	4.7 (1.4)	0.3 (0.9)	-15 (-37.1)	-400 (-988.4)	-505 (-1247.9)	85 (210)
		Aspen	Pre	75 (185.4)	22.8 (5.3)	40.5 (12.4)	49.3 (15.1)	7.4 (18.7)	10 (24.7)	50 (123.6)	135 (333.6)	65 (160.6)
			Post	35 (86.5)	13.5 (3.1)	18 (5.5)	25.3 (7.7)	4.2 (10.7)	10 (24.7)	0 (0)	45 (111.2)	75 (185.4)
			Difference	-40 (-98.9)	-9.3 (-2.2)	-22.5 (-6.9)	-24 (-7.4)	-3.2 (-8)	0 (0)	-50 (-123.6)	-90 (-222.4)	10 (24.8)
	2	Engelmann spruce	Pre	33.3 (82.4)	13.5 (3.1)	3.7 (1.1)	29.2 (8.9)	5.7 (14.4)	3.3 (8.2)	0 (0)	36.7 (90.6)	0 (0)
			Post	20 (49.4)	5.6 (1.3)	15.7 (4.8)	24.7 (7.5)	4.9 (12.4)	3.3 (8.2)	0 (0)	23.3 (57.6)	10 (24.7)
			Difference	-13.3 (-33)	-7.9 (-1.8)	12 (3.7)	-4.5 (-1.4)	-0.8 (-2)	0 (0)	0 (0)	-13.4 (-33)	10 (24.7)
		Ponderosa pine	Pre	143.3 (354.2)	164.4 (37.7)	15.9 (4.8)	53.9 (16.4)	14.7 (37.4)	0 (0)	0 (0)	143.3 (354.2)	0 (0)
			Post	120 (296.5)	159.7 (36.7)	34.6 (10.5)	56 (17.1)	15.5 (39.3)	0 (0)	0 (0)	120 (296.5)	30 (74.1)
			Difference	-23.3 (-57.7)	-4.7 (-1)	18.7 (5.7)	2.1 (0.7)	0.8 (1.9)	0 (0)	0 (0)	-23.3 (-57.7)	30 (74.1)
		Aspen	Pre	3.3 (8.2)	0.7 (0.2)	0 (0)	5.7 (1.7)	2 (5.2)	3.3 (8.2)	33.3 (82.4)	40 (98.8)	3.3 (8.2)
			Post	0 (0)	0 (0)	0 (0)	0 (0)	0 (0)	3.3 (8.2)	33.3 (82.4)	36.7 (90.6)	6.7 (16.5)
			Difference	-3.3 (-8.2)	-0.7 (-0.2)	0 (0)	-5.7 (-1.7)	-2 (-5.2)	0 (0)	0 (0)	-3.3 (-8.2)	3.4 (8.3)
Tripod	1	Western larch	Pre	60 (148.3)	38 (8.7)	24.1 (7.3)	68 (20.7)	10.8 (27.4)	0 (0)	0 (0)	60 (148.3)	0 (0)
			Post	60 (148.3)	38 (8.7)	0 (0)	68 (20.7)	10.8 (27.4)	0 (0)	0 (0)	60 (148.3)	0 (0)
			Difference	0 (0)	0 (0)	-24.1 (-7.3)	0 (0)	0 (0)	0 (0)	0 (0)	0 (0)	0 (0)
		Ponderosa pine	Pre	50 (123.6)	41.4 (9.5)	20.6 (6.3)	57.5 (17.5)	12.3 (31.3)	0 (0)	0 (0)	50 (123.6)	0 (0)
			Post	50 (123.6)	41.4 (9.5)	0 (0)	57.5 (17.5)	12.3 (31.3)	0 (0)	0 (0)	50 (123.6)	0 (0)
			Difference	0 (0)	0 (0)	-20.6 (-6.3)	0 (0)	0 (0)	0 (0)	0 (0)	0 (0)	0 (0)
		Douglas-fir	Pre	70 (173)	24.5 (5.6)	11.6 (3.5)	34.1 (10.4)	8 (20.4)	10 (24.7)	0 (0)	80 (197.7)	0 (0)
			Post	0 (0)	0 (0)	0 (0)	0 (0)	0 (0)	10 (24.7)	0 (0)	10 (24.7)	70 (173)
			Difference	-70 (-173)	-24.5 (-5.6)	-11.6 (-3.5)	-34.1 (-10.4)	-8 (-20.4)	0 (0)	0 (0)	-70 (-173)	70 (173)
	2	Western larch	Pre	30 (74.1)	36.2 (8.3)	27.3 (8.3)	97.7 (29.8)	14.9 (37.8)	0 (0)	0 (0)	30 (74.1)	0 (0)
			Post	----	----	----	----	----	----	----	----	----
			Difference	----	----	----	----	----	----	----	----	----
		Ponderosa pine	Pre	20 (49.4)	79 (18.1)	33.5 (10.2)	104 (31.7)	26.9 (68.3)	0 (0)	0 (0)	20 (49.4)	0 (0)
			Post	----	----	----	----	----	----	----	----	----
			Difference	----	----	----	----	----	----	----	----	----
		Douglas-fir	Pre	80 (197.7)	22.5 (5.2)	7.4 (2.2)	39.8 (12.1)	7.2 (18.3)	150 (370.6)	0 (0)	230 (568.3)	0 (0)
			Post	----	----	----	----	----	----	----	----	----
			Difference	----	----	----	----	----	----	----	----	----

Table 11. Cover by life form by site and deployment.

Incident	Deployment	Item	Status	Cover (%)			Height (ft)		
				Pre	Post	Difference	Pre	Post	Difference
Cooney	1	----	----	----	----	----	----	----	----
Dragon	1	Bare ground	NA	3.0	50.5	47.5	NA	NA	NA
		Forb	Live	0.0	0.0	0.0	0.6	0.3	-0.3
		Grass	Live	0.0	0.0	0.0	0.8	1.0	0.3
		Low shrub	Live	1.5	0.0	-1.5	2.0	0.0	-2.0
		Seedling	Live	6.5	0.0	-6.5	3.0	3.0	0.0
	2	Bare ground	NA	0.0	50.0	50.0	NA	NA	NA
		Forb	Live	0.0	0.0	0.0	0.8	0.3	-0.5
		Grass	Live	6.7	6.7	0.0	0.8	0.8	0.0
		Grass	Dead	4.3	3.3	-1.0	0.1	0.2	0.1
		Seedling	Live	0.0	0.0	0.0	1.5	0.5	-1.0
Tripod	1	Bare ground	NA	3.0	98.0	95.0	NA	NA	NA
		Forb	Live	0.5	0.0	-0.5	0.5	0.0	-0.5
		Grass	Live	20.0	0.0	-20.0	1	0.0	-1.0
		Grass	Dead	3.0	0.0	-3.0	0.5	0.0	-0.5
		Low shrub	Live	3.0	0.0	-3.0	1	0.0	-1.0
	2	Bare ground	NA	3.0	----	----	NA	----	----
		Grass	Live	0.0	----	----	0.5	----	----
		Low shrub	Live	0.0	----	----	0.5	----	----

Table 12. Fuel moistures by site and deployment.

Incident	Deployment	Fuel Moisture (%)					
		Litter	Duff	1 hour	10 hour	100 hour	1000 hour
Cooney	1	----	----	16	15	13	48
Dragon	1	8	13	7	9	13	28
	2	5	6	5	5	5	10
Tripod	1	13	9	13	8	8	----
	2	11	10	10	9	8	----

Table 13. Fuel loadings and consumption, by site and deployment.

Incident	Deployment	Sampling Event	1-hr	10-hr	100-hr	1000-hr Sound	1000-hr Rotten	Duff	Litter
			---Tons per Acre--- (Kilograms per Square Meter)						
Cooney	1	pre	0.07 (0.02)	2.31 (0.52)	0.76 (0.17)	3.55 (0.8)	3.2 (0.7)	0 (0)	16.5 (3.7)
		post	0.06 (0.01)	0.93 (0.21)	0.76 (0.17)	0 (0)	0 (0)	0 (0)	0.6 (0.1)
		difference	-0.01 (-0.01)	-1.38 (-0.31)	0 (0)	-3.55 (-0.8)	-3.2 (-0.7)	0 (0)	-15.9 (-3.6)
		consumption (%)	14	60	0	100	100	n/a	96
Dragon	1	pre	0.29 (0.07)	1.78 (0.4)	2.99 (0.68)	7.37 (1.65)	0.7 (0.15)	4.4 (1)	2.2 (0.5)
		post	0.065 (0.02)	0.31 (0.07)	0.37 (0.08)	3.05 (0.69)	0.15 (0.05)	2.75 (1.2)	0.3 (0.1)
		difference	-0.23 (-0.05)	-1.48 (-0.33)	-2.63 (-0.6)	-4.33 (-0.97)	-0.55 (-0.1)	-1.65 (0.2)	-1.9 (-0.4)
		consumption (%)	79	83	88	59	79	38	86
	2	pre	0.04 (0.01)	0.73 (0.16)	0.54 (0.12)	6.36 (1.43)	0.53 (0.1)	2.9 (0.63)	6.2 (1.4)
		post	0.01 (0)	0 (0)	0 (0)	5.22 (1.76)	0 (0)	1.23 (0.27)	0.37 (0.07)
		difference	-0.03 (-0.01)	-0.73 (-0.16)	-0.54 (-0.12)	-1.13 (0.3)	-0.53 (-0.1)	-1.67 (-0.37)	-5.83 (-1.33)
		consumption (%)	75	100	100	18	100	58	94
Tripod	1	pre	0.29 (0.06)	3.28 (0.74)	4.62 (1.04)	37.43 (8.39)	4.6 (1)	13.4 (3)	1.7 (0.4)
		post	0 (0)	0 (0)	0 (0)	19.19 (4.3)	0.6 (0.1)	8 (1.8)	0.3 (0.1)
		difference	-0.29 (-0.06)	-3.28 (-0.74)	-4.62 (-1.04)	-18.24 (-4.09)	-4 (-0.9)	-5.4 (-1.2)	-1.4 (-0.3)
		consumption (%)	100	100.00	100.00	49.00	87.00	40	82
	2	pre	0.31 (0.07)	1.54 (0.35)	2.9 (0.65)	15.3 (3.43)	0 (0)	22.9 (5.1)	2.8 (0.6)
		post	----	----	----	----	----	----	----
		difference	----	----	----	----	----	----	----
		consumption (%)	n/a	n/a	n/a	n/a	n/a	n/a	n/a

Table 14. Aggregated fuel loadings and consumption, by site and deployment.

Incident	Deployment	Sampling Event	Fines (1-100-hr)	Coarse (1000-hr)	Total Dead and Down Loading	Total Forest Floor Loading	Total Loading	Duff	Litter	Total Forest Floor
			---Tons per Acre--- (Kilograms per Square Meter)					---Depth--- Inches (cm)		
Cooney	1	pre	3.14 (0.7)	6.75 (1.5)	9.9 (2.2)	16.5 (3.7)	26.5 (5.9)	0 (0)	3.3 (8.4)	3.3 (8.4)
		post	1.75 (0.39)	0 (0)	1.8 (0.4)	0.6 (0.1)	2.4 (0.5)	0 (0)	0.1 (0.3)	0.1 (0.3)
		difference	-1.39 (-0.31)	-6.75 (-1.5)	-8.1 (-1.8)	-15.9 (-3.6)	-24.1 (-5.4)	0 (0)	-3.2 (-8.1)	-3.2 (-8.1)
		consumption (%)	44	100	82	96	91	n/a	97	97
Dragon	1	pre	5.06 (1.14)	8.07 (1.8)	13.15 (2.95)	6.6 (1.5)	19.75 (4.4)	0.4 (1.1)	0.4 (1.1)	0.9 (2.25)
		post	0.74 (0.17)	3.2 (0.74)	3.9 (0.9)	3.05 (1.3)	6.95 (1.6)	0.3 (1.4)	0.05 (0.3)	0.25 (0.65)
		difference	-4.33 (-0.97)	-4.88 (-1.07)	-9.25 (-2.05)	-3.55 (-0.2)	-12.8 (-2.8)	-0.1 (0.3)	-0.35 (-0.8)	-0.65 (-1.6)
		consumption (%)	86	60	70	54	65	0.25	88	72
	2	pre	1.31 (0.29)	6.89 (1.53)	8.2 (1.83)	9.1 (2.03)	17.3 (3.87)	0.3 (0.73)	1.23 (3.17)	1.57 (3.9)
		post	0.01 (0)	5.22 (1.76)	5.23 (1.17)	1.6 (0.34)	6.87 (1.53)	0.1 (0.3)	0.07 (0.2)	0.13 (0.37)
		difference	-1.3 (-0.29)	-1.66 (0.2)	-2.97 (-0.67)	-7.5 (-1.7)	-10.43 (-2.33)	-0.2 (-0.43)	-1.17 (-2.97)	-1.43 (-3.53)
		consumption (%)	99	24	36	82	60	67	95	91
Tripod	1	pre	8.19 (1.84)	42.03 (9.39)	50.3 (11.3)	15.1 (3.4)	65.3 (14.6)	1.3 (3.4)	0.3 (0.8)	1.7 (4.2)
		post	0 (0)	19.79 (4.4)	19.8 (4.4)	8.3 (1.9)	28 (6.3)	0.8 (2)	0 (0.1)	0.8 (2.2)
		difference	-8.19 (-1.84)	-22.24 (-4.99)	-30.5 (-6.9)	-6.8 (-1.5)	-37.3 (-8.3)	-0.5 (-1.4)	-0.3 (-0.7)	-0.9 (-2)
		consumption (%)	100.00	53	61.00	45	57	38	100	53
	2	pre	4.76 (1.07)	15.3 (3.43)	20.1 (4.5)	25.7 (5.7)	45.8 (10.3)	2.3 (5.8)	0.6 (1.4)	2.8 (7.2)
		post	----	----	----	----	----	----	----	----
		difference	----	----	----	----	----	----	----	----
		consumption (%)	n/a	n/a	n/a	n/a	n/a	n/a	n/a	n/a

OBSERVATIONS FROM THE AUTONOMOUS ENVIRONMENTAL SENTRY

Autonomous Environmental Sentry (AES) instruments were successfully installed on eight of the eleven deployments accomplished by the Rapid Response Team (Table 8). In this report we provide data and results from three of the eight: Cooney Ridge, Dragon #2, and Tripod #2. For those three deployments, five data elements were analyzed and are presented here (refer to methods section, *"3. Autonomous Environmental Sensor (AES),"* for details):

1. Air temperature (kinetic, from thermocouples)
2. Relative humidity
3. Wind speed
4. Wind direction
5. Radiant temperature/flux (down-looking broadband radiometer, reported as equivalent temperature)

The AES data acquisitions and analyses have not been integrated into the previous discussion in this report regarding the coupling of *in situ* instruments and oblique thermal imaging. However, the AES data will be evaluated for integration into subsequent analyses and reporting efforts relating to this Rapid Response Project. We present the AES data here to demonstrate this successful proof-of-concept.

Cooney Ridge: Data Summary Plots.— Relative humidity (RH) and ambient air temperature were measured at a height of 1.85 meters above the surface. Figure 39 illustrates the inverse relationship between RH and temperature; the approach of fire front, fire passage, and subsequent decay in combustion rates are clearly captured by the RH and temperature instruments.

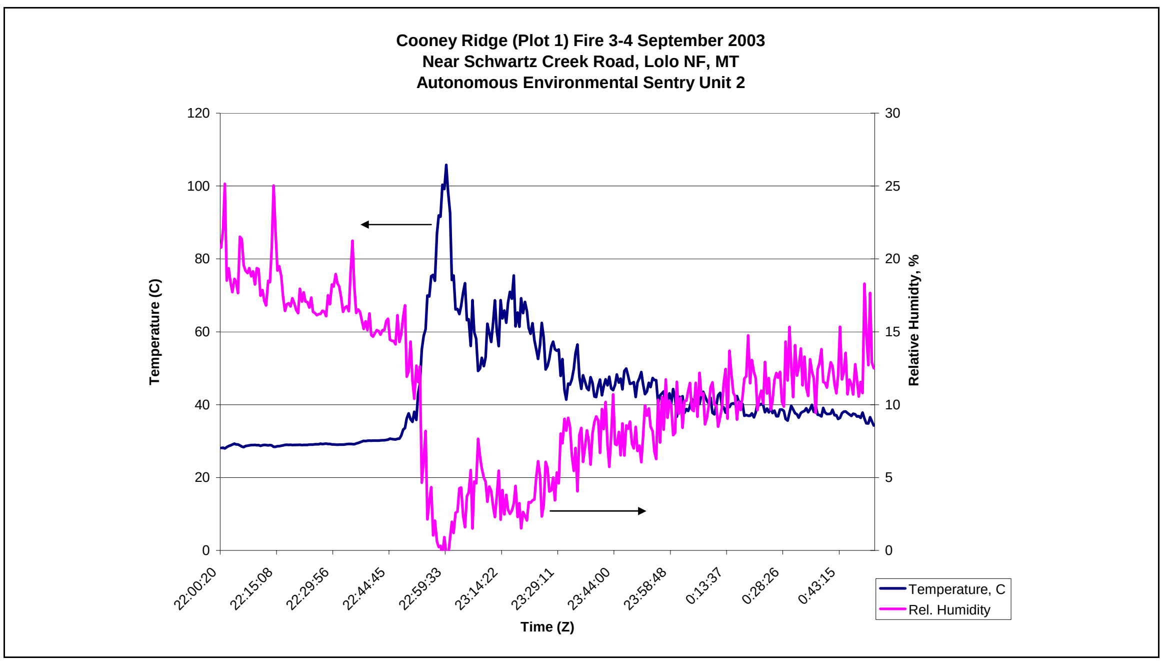

Figure 39. Relative humidity and air temperature plotted for the period of time around the main fire passage for the Cooney Ridge instrument deployment.

Wind direction and average wind speed were measured by the AES for the Cooney Ridge deployment (Figure 40). The wind direction sensor failed after the fire passage at 2300Z. Note that the wind speed increase lags the air temperautre increase (and fire passage--Figure 39). The data were averaged over a 30 second interval, which was also the sampling period for all of the data presented.

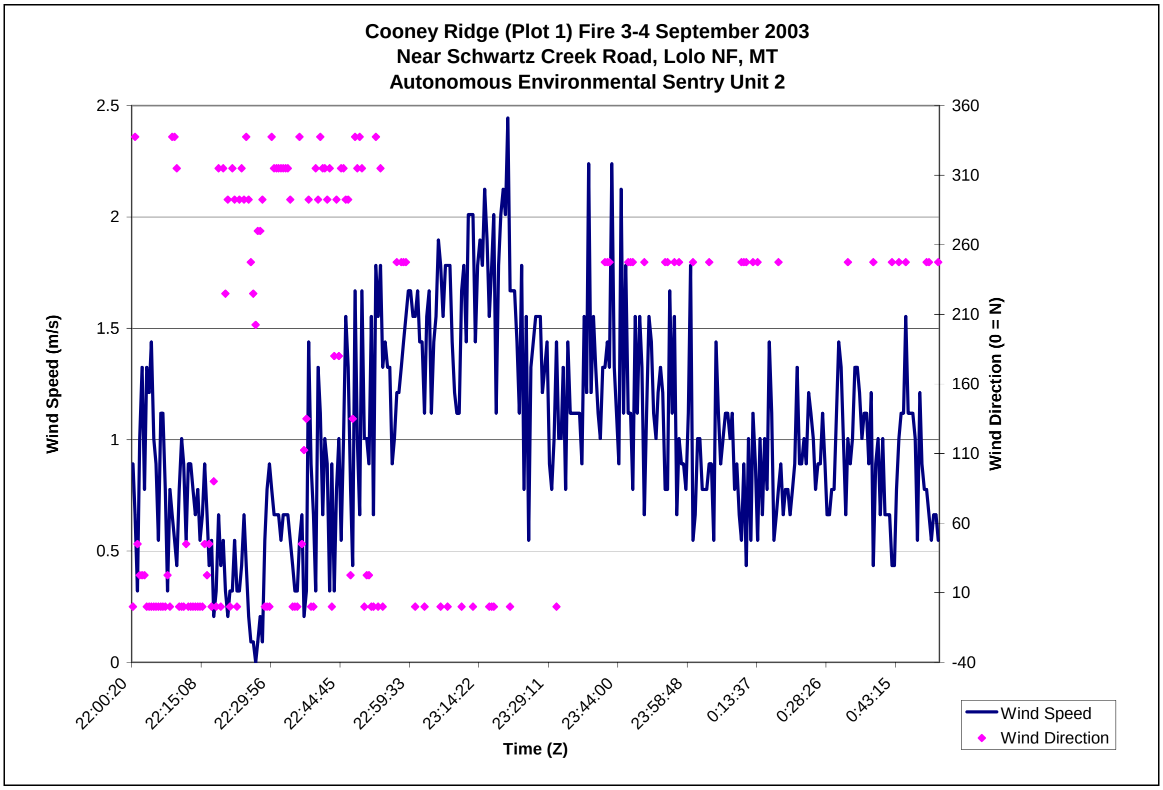

Figure 40. Average wind speed and direction plotted during the fire passage at the Cooney Ridge deployment. The wind direction sensor failed after the fire passage at 2300Z. Note that the wind speed increase lags the air temperature increase (and fire passage). The data were averaged over a 30 second interval, which was also the sampling period for all of the data presented.

A down-looking broad spectrum (1-10µm) thermal radiometer detected radiant flux from an approximately 2m radius area within the sampling plot at Cooney Ridge. The thermal infrared flux measured by this single-band radiometer is presented in Figure 41. The radiometer was calibrated using a blackbody reference source, and all measurements shown in Figure 41 were taken relative to the equivalent blackbody reference.

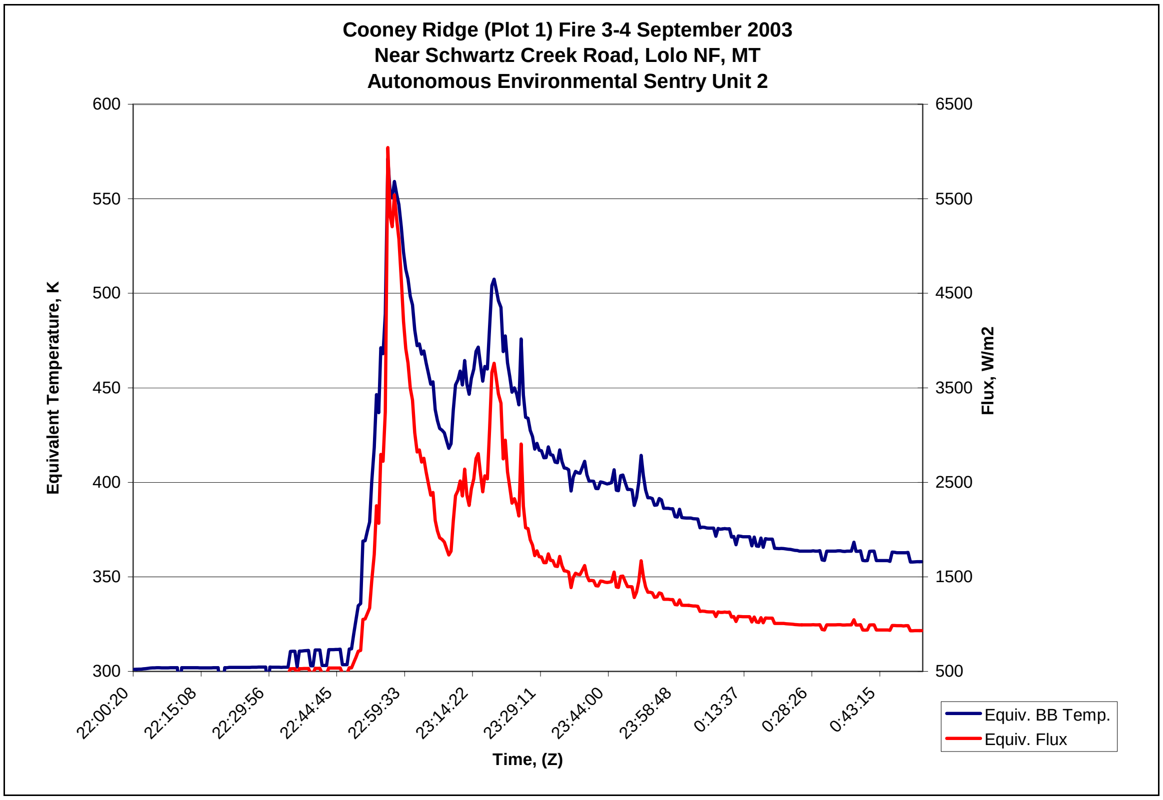

Figure 41. Infrared flux as measured at Cooney Ridge by a single band IR radiometer. The radiometer was calibrated using a blackbody reference source, and all measurements are taken elative to the equivalent blackbody reference.

Dragon #2: Data Summary Plots.— Relative humidity (RH) and ambient air temperature were measured at a height of 1.85 meters above the surface. Figure 42 illustrates the inverse relationship between RH and temperature; the approach of fire front, fire passage, and subsequent decay in combustion rates are clearly captured by the RH and temperature instruments.

Wind direction and average wind speed were measured by the AES for the Dragon #2 deployment (Figure 43). Note that the wind speed increase lags the air temperature increase (and fire passage--Figure 42). The data were averaged over a 30 second interval, which was also the sampling period for all of the data presented.

A down-looking, long-wave (6-13µm) thermal radiometer detected radiant flux from an approximately 2m radius area within the sampling plot at Dragon #2 (Note: this spectral bandpass [6-13µm] is different than measured at Cooney Ridge [1-10µm]). The thermal infrared flux measured by this single-band radiometer is presented in Figure 44. The radiometer was calibrated using a blackbody reference source, and all measurements shown in Figure 44 were taken relative to the equivalent blackbody reference.

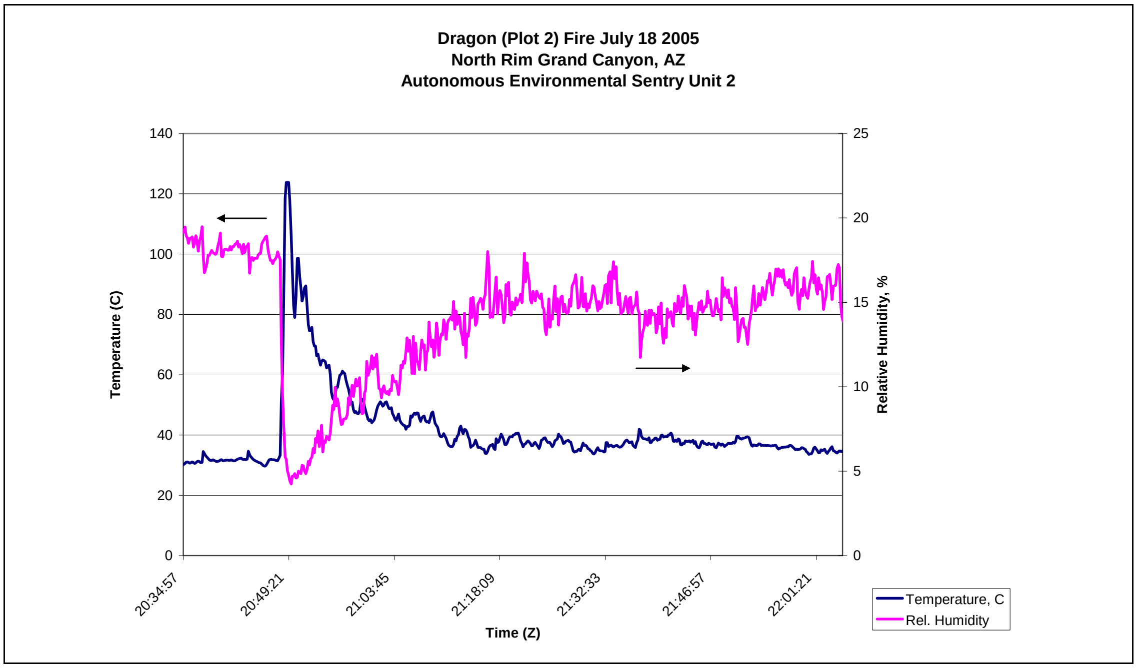

Figure 42. Relative humidity and air temperature plotted for the period of time around the main fire passage for the Dragon #2 instrument deployment.

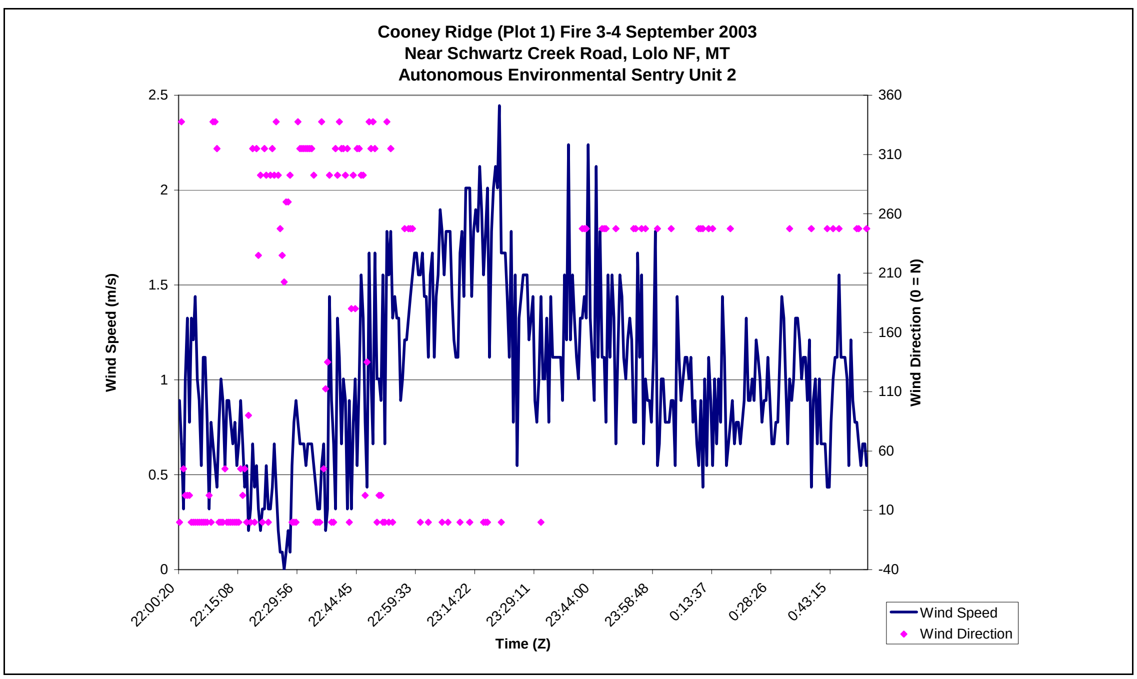

Figure 43. Average wind speed and direction plotted during the fire passage. The data were averaged over a 10 second interval, and the mode of the wind direction was also averaged over this period.

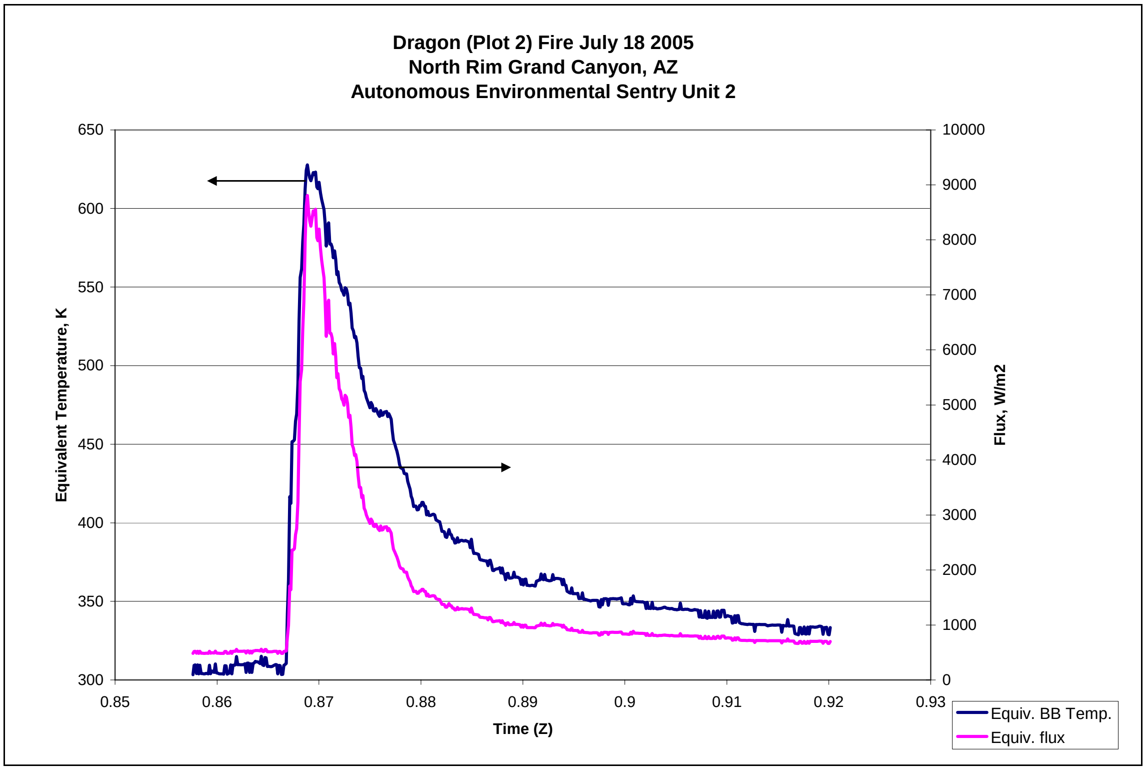

Figure 44. Infrared flux as measured at Dragon #2 by a single band IR radiometer. The radiometer was calibrated using a blackbody reference source, and all measurements are taken elative to the equivalent blackbody reference.

COUPLING AND INTEGRATION OF IN SITU INSTRUMENTS WITH GROUND-BASED THERMAL IMAGING SYSTEMS

The following describes the coupling of *in situ* instruments with ground-based thermal imaging systems during rapid response style measurements of wildland fires. Comparisons between total and radiant heat flux, and between hemispherical and narrow angle acceptance angles, were conducted with the *in situ* measurements. Horizontal accuracies of the georegistered thermal images are provided, and analyses of thermal sequences were performed on a per pixel as well as on an areal basis. Case studies of individual wildland fire events are presented as examples of how to interpret heat flux profiles measured from either sensor location, and distinct macroscopic features of the profiles are identified as a means of comparing cross-platform measurements. The potential for estimating first-order fire effects was examined by comparing the total radiant energy measured over the duration of the fire to the total fuel consumed obtained through pre- and post-burn fuel surveys. Finally, the advantages and disadvantages of each measurement method are addressed with recommendations for proper field applications in the future.

Successfully Coupled Sensor and Imager Installations

Over the course of five field campaigns, ten study plots were instrumented with *in situ* radiometers and observed with at least one thermal imaging system located at an oblique, ground based vantage point (Table 15). Distances from the sensors to the nearest vehicle drop point ranged from a few meters to 1.7 kilometers. Where possible the vantage point was situated above the plot to optimize the observation angle, however satisfactory viewing geometries were also achieved with the TIR cameras stationed below the study site. Topographical depressions were often exploited to accommodate small differences in elevation between the *in situ* and remote camera locations, and perfectly flat terrain was the only spatial constraint that prevented concurrent deployment methodologies.

Table 15. Summary of Rapid Response Sensor Installations

Incident Name	Location	Deploy ID	Date	Camera Coordinates	Horizontal Distance Between Cameras and Study Site	ΔElevation (El_{sensor} - El_{plot})	Duration (hh:mm:ss)	Sampling Frequency Midwave Camera	Sampling Frequency Longwave Camera
Cooney Ridge	Lolo NF, MT	1	03-Sep-03	N 46.70348° W 113.78525°	785 m	176 m	1:29:53	2 fpm	na
Dragon WFU Complex	Grand Canyon NP, AZ	1	17-Jul-05	N 36.24405° W 112.10106°	190 m	29 m	3:21:46	4 fpm	4 fpm
		2	18-Jul-05		280 m	-12 m	1:56:30	4 fpm	4 fpm & 12 fpm
I-90 Complex	Lolo NF, MT	1	11-Aug-05	N 47.01068° W 114.57170°	31 m	-9 m	0:33:45	4 fpm	na
		2	11-Aug-05		86 m	-14 m	1:12:12	4 fpm	na
		3	12-Aug-05	N 47.03255° W 114.57720°	1221 m	-138 m	1:02:00	4fpm	na
Selway-Salmon WFU Complex	Bitterroot NF, MT	1	01-Sep-05	N 45.70442° W 114.71628°	742 m	-151 m	1:10:11	12 fpm	12 fpm
		2	01-Sep-05		725 m	-129 m	3:24:47	12 fpm	12 fpm
Tripod Complex	Okanogan-Wenatchee NF, WA	1	24-Aug-06	N 48.47917° W 119.80886°	1786 m	-117 m	2:09:27	2 fpm	12 fpm
		2	24-Aug-06		1812 m	-126 m	2:09:27	2 fpm	12 fpm

Interpretations of *in-situ* heat flux instrument (FBP) profiles.— Since insolation never exceeded the minimum heat flux required to initiate data acquisition, all trigger events were the direct result of the orientation of the hemispherical radiometer with respect to location and intensity of the fire. Instrument packages facing the oncoming front were generally triggered (1) by an event outside of the study site, and (2) prior to the instrument packages facing away from the oncoming front. Time lags between an initial, radiant heat pulse and the peak heat flux measured while the fire was within the plot perimeter ranged from 75 seconds to 24 minutes. These temporal differences were not used to ascertain rates of spread, however, since distance and direction could not be resolved.

Instantaneous ratios between total and radiant heat flux measurements were used to partition heat transfer mechanisms. Separating the total heat flux into a radiant fraction, and hence a combined convective and conductive fraction, facilitated the interpretation of fire behavior and quantified the role of each mode of heat transfer during a particular combustion process. Plots of partitioned energy for Dragon #1 and Dragon #2 are illustrated in Figure 45. For example, the data set collected during the Dragon Wildland Fire Use (WFU) Fire on 17 July 2005 (Dragon #1) captured an individual torching tree followed by a high intensity surface fire (Figure 45a). The following interpretations apply to Fire Behavior Package # 2 aligned facing down slope toward the fire front approaching from below the study site:

- Approximately 3 minutes after the trigger event, a slight perturbation (almost imperceptible in Figure 45a) in the ambient air temperature, concurrent with a fluctuation in the total heat flux, not the radiant heat flux, indicated the development of fire-induced, upslope winds.
- At 3 ½ minutes, heat transfer was dominated by radiative exchange as a solitary tree torched outside the study plot. The radiant heat flux profile shows this event lasted approximately 2 minutes, after which the fireline became firmly established immediately below the plot.
- Contemporaneous oscillations in the total and radiant heat flux profiles between 4 ½ an 8 minutes verify that (1) the fire front was within the FOV of the radiometer, and (2) radiative emission from the flaming front was not entirely attenuated by the intervening, unburned vegetation.
- The division of heat transfer between 4 ½ an 8 minutes suggest that fuels in the plot were primarily dried and pre-heated through convection.
- The moderate flare-up at 8 minutes occurred adjacent to the plot.
- At 8 ½ minutes, the radiant contribution to the total heat transfer increased as the flaming front reached the study site, and by 10 ½ minutes the plot is fully involved.
- An abrupt decrease in the radiant fraction at 11 ½ minutes suggests that either (1) the flaming front progressed beyond the FOV of the hemispherical radiometer, or (2) the flames extinguished due to the consumption of available fine fuels.
- At 11 ½ minutes, and lasting approximately 51 minutes thereafter, the continual decay of heat flux across the sensor was attributed to the post-frontal combustion, and subsequent burn-out, of coarse woody debris, duff, and litter.

Calculating the temporal integral of each profile with an assumed, constant heat flux over the sample interval yielded a total energy density of 21.8 MJ/m^2, and a radiant energy density of 5.3 MJ/m^2. Ratios between total and radiant energy densities can only be used to characterize the division of heat transfer across a unique, differential element of area in space, and cannot be used to estimate the fraction of total energy liberated in form of radiation during the combustion of biomass. Time-integrated fractions of incoming radiant energy density to total energy density ranged from 24% to 80% depending on the attitude of the sensor package and the nature of the fire environment itself.

Concurrent heat fluxes measured by the hemispherical and narrow angle radiometers were also different. The absolute magnitude of the heat flux profile not only depended on the kinetic temperature of the fire, but also the radiative properties of the emitting object, as well as the thermal distribution within the field of view.

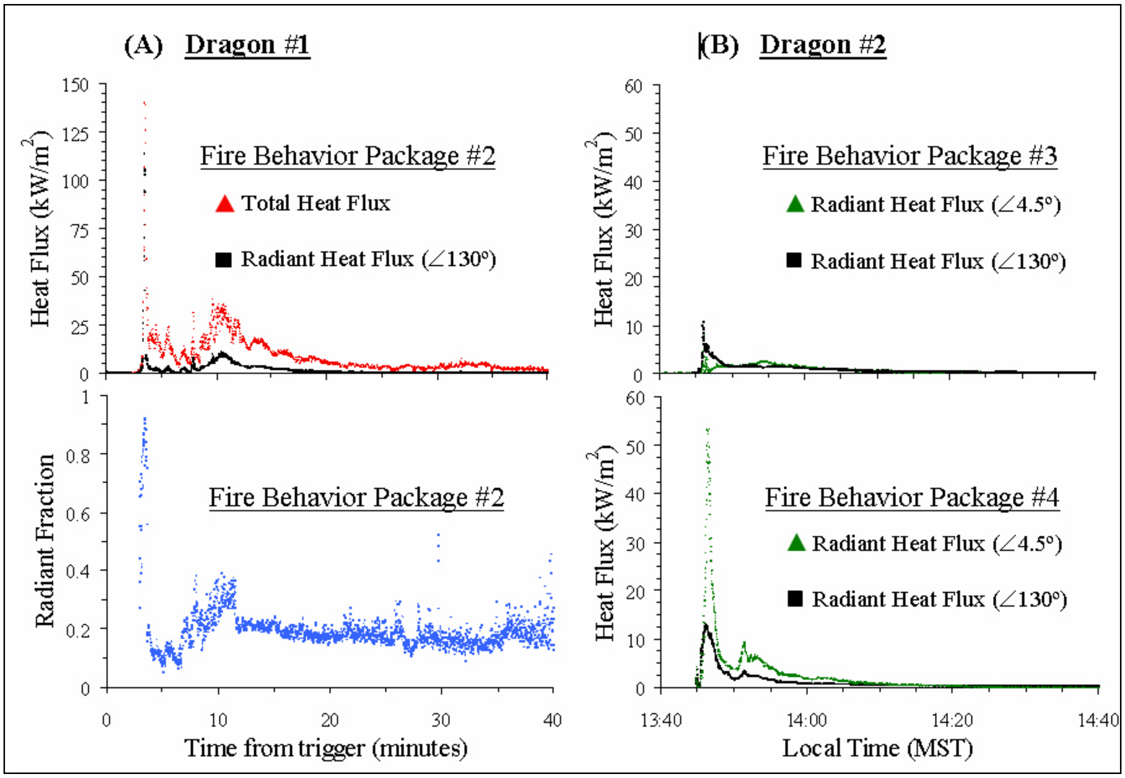

Figure 45. (a) Collocated, temporal profiles of total and radiant heat flux measured by a hemispherical radiometer (top) during the Dragon WFU Fire on 17 July 2005 (Dragon #1). Radiant fractions (bottom) were calculated by dividing the radiant heat flux by the total heat flux. Noise at the beginning of the profile of radiant fractions has been truncated. (b) Radiant heat flux profiles measured by a narrow angle and hemispherical radiometer during the Dragon WFU on 18 July 2005 (Dragon #2). Both fire behavior packages were oriented towards plot center. Package # 3 (top) was facing the oncoming front while package # 4 (bottom) was facing away from the oncoming front.

The emissivity of a solid is influenced by surface roughness, and by chemical reactions occurring on the surface, both of which change over time during char formation. In general, where measurements are unavailable, the surface emissivity of a combusting fuel particle is obtained from ancillary data sets based on species and condition or, more than often, assumed to be perfect (Urbas and Parker 1993, Dietenberger 1999). Flame emissivities are dependent on the concentration, size distribution, and refractive index of soot particles, as well as the depth of the flame. Emissivity increases with flame depth, and although emissivity is assumed 1 for sufficiently thick flames (Robinson 1991), the critical path length required for flames in a wildland fire to achieve blackbody emission is often disputed, varying from about one meter to three meters. At any given distance, the FOV of the NAR subtends an area approximately 0.1% of the hemispherical radiometer. For a pair of sensors collocated 1 m above the ground, aligned parallel with the ground, FOV's of ∠130° and ∠4.5° intersect the ground plane at horizontal distances of 0.9 m and 14.5 m from the detector, respectively. In this arrangement, the hemispherical radiometer is responsive to surface emission from exposed fuel particles as well as volumetric emission from flames, whereas the NAR is generally responsive to only the flames. If aligned looking across the slope, or upslope, however, the thermal signal of the NAR also includes emissive contributions from ground and surface fuels.

During the Dragon WFU Fire on 18 July 2005 (Dragon #2), two fire behavior packages oriented towards plot center recorded low to moderate surface fire behavior (Figure 45b). Peaks in radiant heat flux and time-integrated radiant energy densities measured by the opposing hemispherical radiometers were relatively comparable (i.e. 10.8 vs. 13.1 kW/m^2 and 2.8 vs 3.7 MJ/m^2). In contrast, peaks in radiant heat flux and time-integrated radiant energy densities measured by the opposing narrow angle radiometers were considerably different (i.e. 11.3 vs. 53.5 kW/m^2 and 2.5 vs 7.6 MJ/m^2). Since coincident peaks and equivalent durations reaffirm observations of the same fire behavior within the plot, differences in the absolute magnitude of the profiles can be attributed to the spatial distribution of emitting objects within the plot, and their relation to the orientation of an individual detector. Furthermore, if large fuel particles are assumed stationary and combustion processes on the surface are assumed homogeneous, or at least similar when viewed from different angles, then these differences can be specifically attributed to the location of the flames within the plot. Flames closer to the detector presumably occupy a greater portion of the FOV, and therefore induce a greater signal.

Interpretations of heat flux profiles on a per pixel basis.— Point trends of radiant heat flux were generated from time series of midwave and longwave pixel brightness temperatures (Figure 46). Band-to-band coregistration was not performed, therefore no horizontal accuracy assessment is provided. Compared to investigating isolated pixels, subsetting the imagery to the plot area alleviates differences in the spatial resolutions of each optical system, and minimizes the effects of errors in absolute georegistration. Thermal signals associated with ground cells indiscriminately included within in the area of interest, however, were either (1) completely obscured by tree stems, (2) partially attenuated by the participating canopy cover, or (3) undetected above a certain threshold due to sensor saturation. As a result, individual pixels were hand selected for this analysis to ensure a clear line of site, and an accurate brightness temperature measurement. An analysis of areal calculations is presented in the Section C.

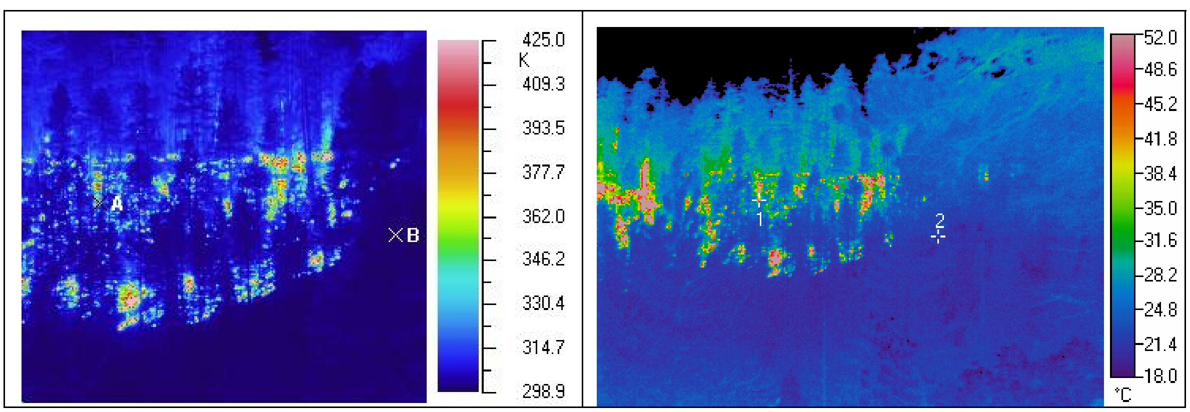

Figure 46. Midwave (left) and longwave (right) thermal images collected concurrently at 15:16:00 MDT during the Dragon WFU Fire on 18 July 2005. Temporal profiles of radiant heat flux were generated for pixels labeled “A” and “1,” which identify an unobstructed ground cell within the study site, and for pixels labeled “B” and “2,” which identify an unobstructed ground cell outside of the plot that was used for background characterization.

Since sequences of imagery were manually initiated at the earliest opportunity, all temporal profiles of radiant heat flux had leading edges prior to the arrival of the fire front. Like fire behavior packages, temporal profiles measured by the TIR cameras indicated the approach, residence, and passage of the fire front with residual post-frontal combustion (Figure 41a). On occasion observations intended to measure the radiance emitted from a ground cell within the plot were confounded by fire activity outside of the plot. Events occurring downslope, such as a torching tree or a sudden increase in fireline intensity, produced vertical sheets of flame, lofting embers, and superheated gases, vapors, and aerosols that interrupted the line of site. Features otherwise misinterpreted as fire behavior within the plot also include artifacts due to measurement techniques. Although calibration of the midwave sensor extended below each dynamic range, non-linear relationships between DN and bandpass radiance were exaggerated at the limits of detector sensitivity, and it was further necessary to extrapolate prediction equations below a minimum blackbody setpoint of 373 K (2.8 kW/m^2). Therefore abrupt variations in the midwave profile due to a change in dynamic range are most consequential when the true radiometric temperature exists within the specification of one range, but considerably outside the other. Subtle discontinuities also occur when either camera is repositioned even minutely. This causes a break in the viewing geometry and a slight misalignment between pixels. These episodes were spurious, and also concurrent with a dynamic range change as the camera was handled.

Synchronization of the midwave and longwave response to fire behavior depended on the nature of the event, and the sampling frequency. For example, the transitory torching tree at 13:38:15 local time was sampled no more than 4 times between crown fire initiation and extinction (Figure 47a). Though peaks in heat flux measured by the midwave and longwave cameras were coincident during this event, the thermal signal was noticeably aliased. At 13:45 local time, progression of the fire front into a ground cell was first detected by the midwave sensor. Here, if the pixels significantly overlapped, the smaller IFOV was occupied by a greater fraction of fire, and the rate of increase of radiant energy in the midwave band was greater for a given increase in temperature. Peaks in radiant heat flux were concurrent at 13:47:30 when both the midwave and longwave pixels were nearly resolved by the surface fire. Though the absolute magnitudes of the peaks differ, the relative rates of thermal decay measured by each sensor are quite similar (Figure 47b). After the passage of the flaming front, the ground cell itself does not simply dissipate heat through conduction, convection, and radiation, but rather combustion reactions continue to produce heat. The decay profile, therefore, is an aggregate of the post-frontal consumption of all fuels within the pixel. The time-integrated radiant energy densities measured by the midwave and longwave thermal imaging systems were 16.6 and 4.7 MJ/m^2, respectively.

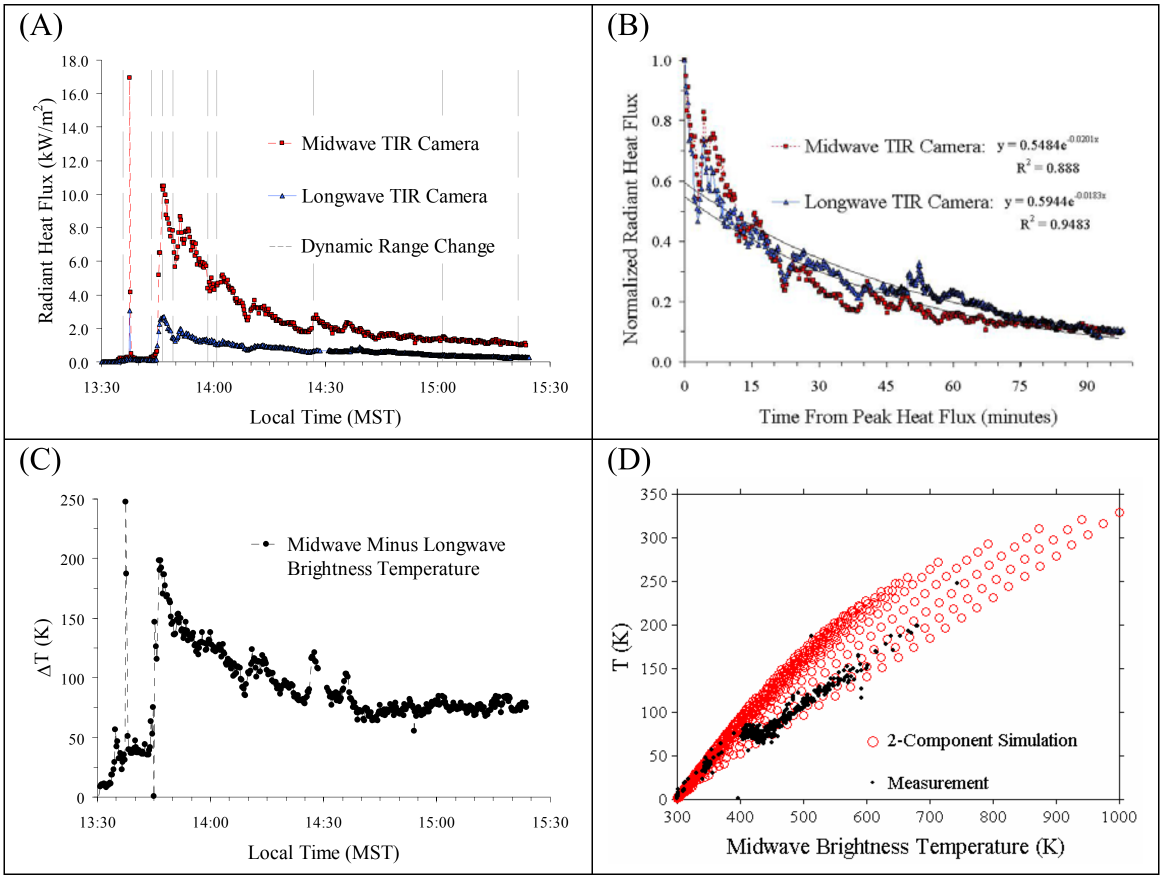

Figure 47. Plots of data from the ground-based TIR cameras during the Dragon WFU Fire on 18 July 2005 : Temporal profiles of radiant heat flux (**a**). The midwave profile corresponds to pixel location “A,” and the longwave profile corresponds to pixel location “1” in Figure 46. Dynamic range changes are associated with the midwave camera only. Normalized radiant heat flux profiles after the local maxima at 13:46:00 MDT (**b**). The midwave profile is normalized to 10.49 kW/m^2, and the longwave profile is normalized to 2.69 kW/m^2. Difference between midwave and longwave brightness temperatures (**c**). Theoretical difference between midwave and longwave brightness temperature for a 2-component simulation (**d**).

Since Stefan Boltzmann’s Law was applied to both the midwave and longwave imagery, instantaneous differences in radiant heat flux were due to differences in measured pixel brightness temperatures (Figure 47c). In turn, differences in measured brightness temperatures were due to the distinct spatial resolution and spectral response function of each sensor. To verify the magnitude of the temperature differences, a two-component radiative heat transfer simulation was performed. Homogeneous fire temperatures, T_f, ranged from 325 K to 1000 K, and occupied up to 100% of the midwave and 40% the longwave pixel, $p_{f,mid}$ and $p_{f,long}$ respectively. The remaining fraction of each pixel, p_b, was assigned an isothermal background temperature, T_b, of 300 K. Both the fire and the background were assumed to radiate like a blackbody. The bandpass radiance across each detector was calculated and converted to brightness temperature. Although a two component representation greatly oversimplifies the continuous thermal distribution within a pixel, the boundary of the simulation contains most observations (Figure 47d). Outliers were associated with rapid changes in fire behavior and therefore subject to bias in the precise synchronization between radiometric measurements.

Interpretations of heat flux profiles on an areal pixel basis.— Three sequences of thermal imagery corresponding to four distinct deployments were georegistered and analyzed in a customized processing chain. One sequence was analyzed from each of the two Dragon WFU deployments, and a single sequence containing both Tripod deployments in the field of view was analyzed (Table 16). Horizontal accuracy assessments revealed that the RMSE statistic increased as the distance between the TIR camera and the target increased (Table 16). Since ground control points were established within the vicinity of plot center, the accuracy of each georegistered sequence is considered valid for only the immediate area surrounding plot center. Although the accuracy of the georegistation was not examined beyond the study plot it is assumed that the reliability of the mapping transform degrades with distance from plot center and the complexity of the terrain. Furthermore the RMSE error statistic has yet to be related to an error in line-of-site distance; therefore the resulting error in pixel area, and consequently FRP and FRE, due to an error in georegistration remains unquantified.

Table 16. Summary of georegistration of three sequences of midwave thermal imagery.

Incident Name	Date	Deploy I.D.	Plot I.D.	Horizontal Distance Between Camera and Plot	Number of Plots w/in FOV	Number of GCP's	Horizontal Accurracy Statistic (NSSDA)	Number of Thermal Pixels in Study Plot	Study Area Projected onto FPA
Dragon WFU Fire	17-Jul-05	1	395	190 m	1	3	7.63 m	7897	221.4 m^2
	18-Jul-05	2	397 & 399	280 m	2	4	8.33 m	4740	307.0 m^2
Tripod Complex	24-Aug-06	1	972	1786 m	2	5	30.65 m	30	95.8 m^2
		2	973	1812 m				32	105.2 m^2

Two examples of matrices of line-of-sight (LOS) distance illustrate the output of the georegistration procedure (Figure 48). Both high and low oblique scenarios were encountered, but neither the horizon nor any other topographical feature, as defined by the site selection criteria, interrupted the vector between the camera and the study plot. In general, pre- and post burn surveys were conducted within on study plot per deployment, however three plots were sampled during the second deployment of the DragonWFU Fire – two of which were within the field of view of the thermal imaging system. Here, the union of the two plots was used to define the study domain and to subset the imagery. Again, in general, one deployment was captured with one sequence of thermal images. Exceptions included the Selway-Salmon WFU Complex and the Tripod Complex, where two deployments were captured with a single viewing geometry.

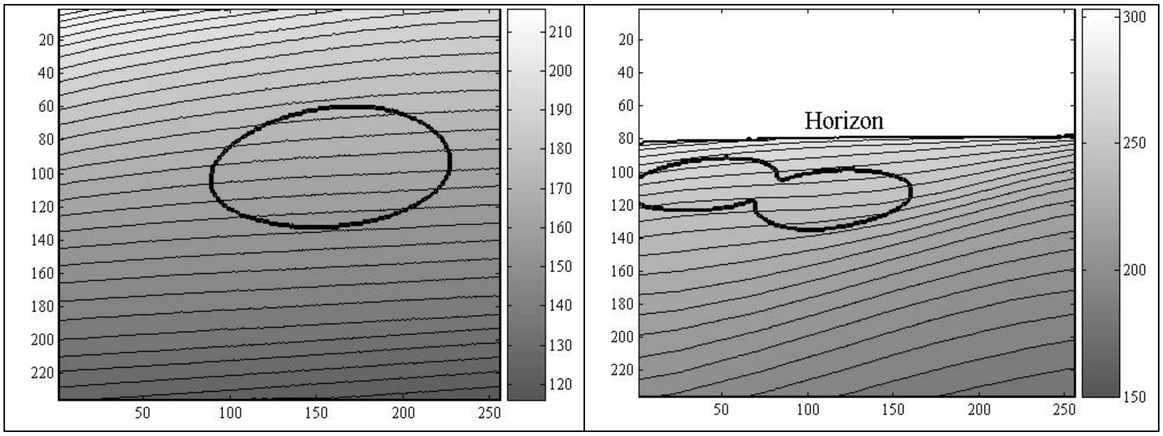

Figure 48. Matrices of line-of-site distance corresponding to the 236 × 256 focal plane array of the mid-wave thermal imaging system. At left is Plot 395 of Deployment # 1, and at right are Plots 397 and 399 of Deployment # 2 of the Dragon WFU Fire. Contours of constant LOS distance are drawn at 30 m intervals.

As described using Eq. [5], the area subtended by, and parallel to, an individual detector increased with the square of the LOS distance. Therefore the number of pixels representing the study plot in the oblique imagery decreased with an increase in LOS distance as well as with an increase in the observation angle. The total number of pixels analyzed within the study domain for any one deployment ranged from 30 to 7897 corresponding to projected areas of 95.8 and 221.4 m^2, respectively. Fewer numbers of thermal pixels composing the study plot resulted in more discrete area calculations. Differences between the actual tenth-acre surface area (404.7 m^2) and the cross-sectional area projected onto the FPA were due to the observation angle which inherently accounts for both the slope and aspect of the ground plane. More oblique viewing geometries had greater the observation angles (i.e., the observation angle approached $\angle 90°$) and resulted in less area of the study plot projected onto the focal plane array.

The effects of the absolute and relative detection criteria were most pronounced in the determination of instantaneous and time-integrated fire area projected onto the FPA (Figure 49 and Table 17). Although the mid-wave bandpass is more appropriate for calculating total radiative power since these wavelengths more closely correspond to the peak in the Planck curve at such temperatures, the limited dynamic range of the sensor prevented an accurate brightness temperature measurement of all fire pixels spanning thermal distributions of hundreds of Kelvin. Thus for a fixed viewing geometry the apparent discontinuity in the profile of instantaneous fire area are attributed to manual changes in dynamic range selection during data acquisition. Unfortunately the maximum sequential difference in instantaneous fire area within a given range cannot be compared to that occurring during a dynamic range change due to erratic, and often extraneous, fire behavior. Torching trees below and within the study plot caused extreme fluctuations in fire area not directly associated with the ground or surface fire progressing through the study plot. The dynamic range of the TIR camera was changed less frequently at the end of the observational period during smoldering combustion when the fire's area and thermal distribution were temporally less variable.

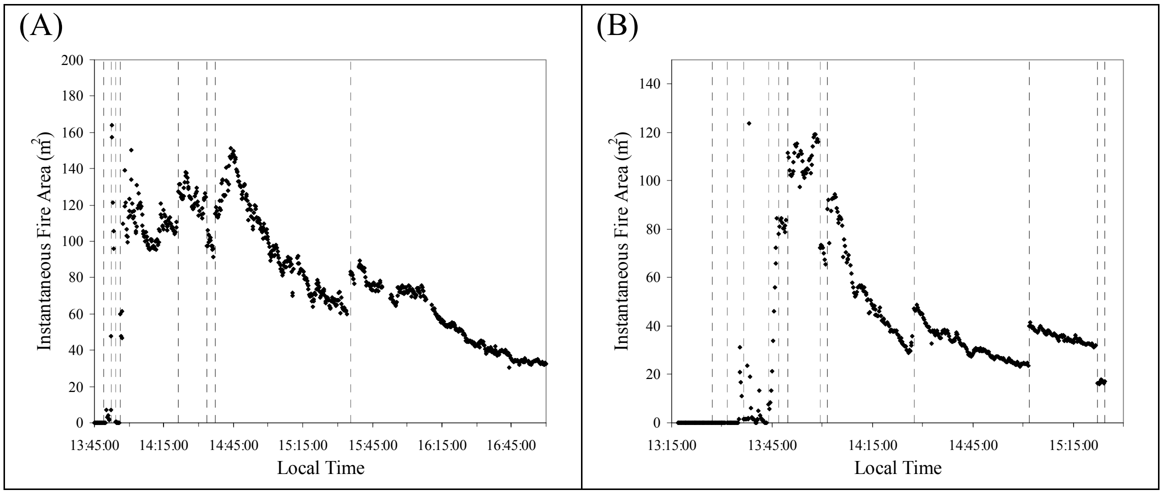

Figure 49. Temporal profiles of instantaneous fire area within the study plot. At left (**a**) is Plot 395 of Deployment # 1; at right (**b**) are Plots 397 and 399 of Deployment # 2 of the Dragon WFU Fire. Dashed lines represent changes in the dynamic range setting of the camera during data acquisition.

Table 17. Time-integrated results summarized by incident, deployment, and detection criteria.

				Fire Radiative Energy (Time-integrated Fire Area)			
Incident Name	Date	Deploy I.D.	Plot I.D.	Absolute Threshold	1st Relative Filter	2nd Relative Filter	3rd Relative Filter
Dragon WFU Fire	17-Jul-05	1	395	1.60 GJ ($240.2\ m^2hr$)	1.60 GJ ($240.6\ m^2hr$)	1.60 GJ ($243.3\ m^2hr$)	1.62 GJ ($253.5\ m^2hr$)
	18-Jul-05	2	397 & 399	0.29 GJ ($61.5\ m^2hr$)	0.29 GJ ($65.5\ m^2hr$)	0.30 GJ ($71.6\ m^2hr$)	0.32 GJ ($81.4\ m^2hr$)
Tripod Complex	24-Aug-06	1	972	1.21 GJ ($213.5\ m^2hr$)	1.22 GJ ($215.2\ m^2hr$)	1.22 GJ ($215.2\ m^2hr$)	1.22 GJ ($215.2\ m^2hr$)
		2	973	1.75 GJ ($185.7\ m^2hr$)	1.75 GJ ($185.7\ m^2hr$)	1.75 GJ ($185.7\ m^2hr$)	1.75 GJ ($187.0\ m^2hr$)

The effects of the detection algorithm, vis-à-vis a change in dynamic range, are less consequential in the calculation of *FRP* and consequently *FRE* (Figure 50 and Table 18). The detection algorithm is, by design, sensitive to cooler brightness temperatures, and with the exception of extreme viewing geometries, these pixels generally carry an equivalent weight in the calculation of instantaneous fire area. Once subjected to a fourth order power law, however, the magnitude of a measurement of *FRP* is strongly influenced by pixels having the greatest brightness temperatures. Therefore, cooler, ambiguous fire pixels have less significant contributions to spatially integrated values of *FRP* than to instantaneous fire area.

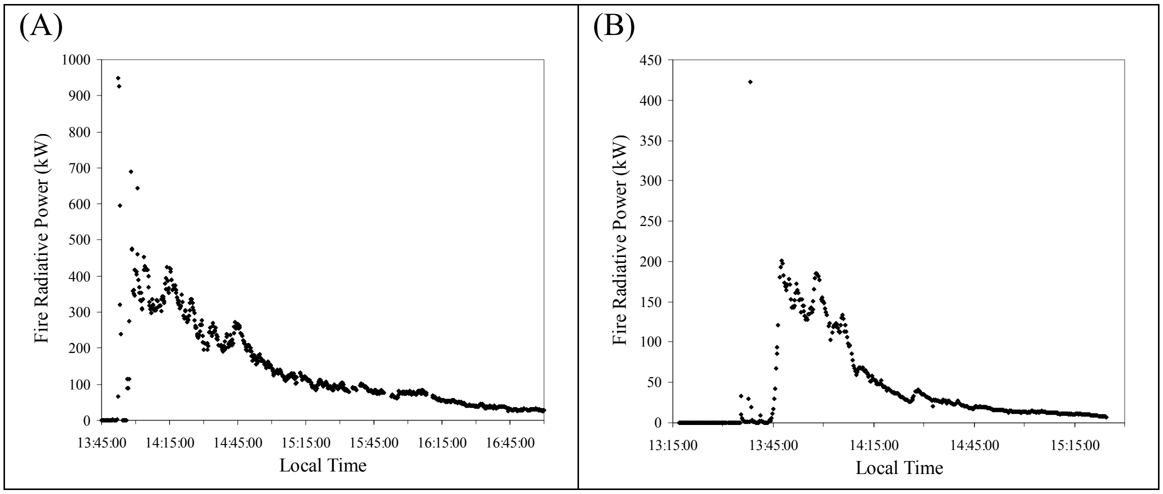

Figure 50. Temporal profiles of fire radiative power. At left (**a**) is Plot 395 of Deployment # 1, and at right (**b**) are Plots 397 and 399 of Deployment # 2 of the Dragon WFU Fire.

Table 18. Heat yields measured by hemispherical radiometers and the midwave thermal imager.

Deploy I.D.	Total Fuel Consumed (Kg/m^2)	Fire Behavior Package (F.B.P.) F.B.P I.D.	Total Energy Density (MJ/m^2)	Measured Total Heat Yield (MJ/Kg)	Radiant Energy Density (MJ/m^2)	Measured Radiant Heat Yield (MJ/Kg)	Midwave Thermal Imager Radiant Energy Density (MJ/m^2)	Measured Radiant Heat Yield (MJ/Kg)
1	5.7	2 4	21.79 5.77	3.8 1.0	5.28 4.18	0.9 .7	7.32	1.3
2	2.5	3 4	5.68 5.37	2.3 2.1	3.20 4.26	1.3 1.7	1.04	0.4
1	8.3	2 4	8.48 5.11	1.0 0.6	6.88 3.75	0.8 0.5	12.73	1.5
2	--	1 3	12.65 22.04	--	8.51 15.48	--	16.63	--

Since the total rate of emission of radiative energy depends on the heat flux as well as the fire area, proper interpretations of *FRP* rely on the proper interpretation of fire area. Dividing the *FRP* presented in Figure 50 by the instantaneous fire area presented in Figure 49 yields the average radiant heat flux over all fire pixels. Only by calculating the radiant heat flux emitted over all fire pixels can an increase, or decrease, in the total radiant heat transfer rate be decomposed into either an increase, or decrease, in fire area or fire intensity.

Comparisons between radiant energy densities and total fuel consumption.— The measured fuel consumption values obtained by the site characterization team (refer to the *Results* section "*Vegetation, Fuels, and Site Characterization,*" Tables 13 and 14) can be used to assess fuel consumption estimates based on FRE. Time-integrated results of FRE and fire area for each deployment, along with total fuel consumption, are presented in Figure 51. Assuming a heat content of 18.0 MJ/Kg, the fraction of energy liberated in the form of radiation (and detected by the sensor) ranged from 2.4 % to 7.3 %. Although values for the radiant heat yield, and thus the radiant fraction, were on the same order of magnitude as those obtained with the same thermal imager under laboratory conditions, a different detection algorithm and a different method of calculating FRE were used. After re-processing the images using the MIR radiance method, calculations of FRE for Dragon deployments 1 & 2 and Tripod deployments 1 & 2 (analysis of Tripod #1 and #2 were combined) were lower than values calculated using Stefan Boltzmann's Law by 65%, 48%, 33%, and 94% of those, respectively. These results suggest that high oblique thermal imagery underestimates both the true radiative energy released during combustion as well as the radiant heat yield. More importantly, this suggests radiant heat yields measured in the field are less than those obtained in the laboratory. If measurements of FRE and fuel consumption are considered accurate in the laboratory, and estimates of fuel consumption are considered accurate in the field, then differences in heat yield are attributed to the attenuation of the thermal signal emitted from a landscape fire. Participating media in an oblique field deployment included (1) tree boles and stems within and below the plot, (2) branches and needles within the canopy, and (3) the intervening atmosphere and smoke plume.

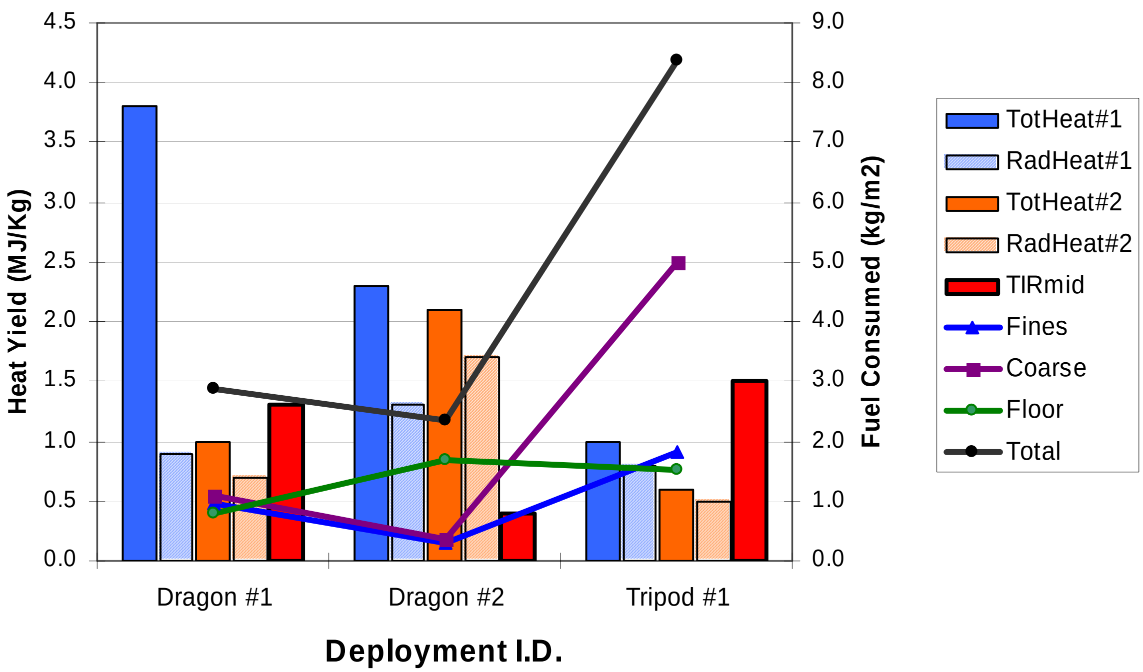

Figure 51. Graphical representation of heat yields (from Table 18) and field-measured fuel consumption (excerpted from table 14). Data from two *in situ* fire behavior flux packages and from the oblique thermal IR camera are plotted as bars: bars shown in blue are from the 1st flux package; bars shown as orange are from the 2nd flux package. Fuel consumption is plotted by the lines associated with the second Y-axis (right side); note that the units are different. Juxtaposition of heat yield and fuel consumption is shown for relative, rather than absolute comparative purposes.

Several observations and relationships are revealed in Figure 51:

- The ratio of total-to-radiant heat yield decreases with decreases in absolute value of heat yields; the relationship is shown consistently for both flux packages plotted in Figure 51.
- The ratio of total-to-radiant heat yield for the Dragon #1 deployment is much greater than for the other two deployments shown in Figure 51. This suggests much elevated convective heat transfer in proximity of flux package #1 on the Dragon #1 deployment, relative to the other package and deployments.
- Neither total nor radiant heat yields measured by the two flux packages are necessarily similar between the two packages. When two packages are deployed, they are at either edge of the site, and the viewing geometry of each is directed towards plot center. Therefore, each package is exposed to fire energy from different areas within the plot.
- Total and radiant heat yield measured by both packages on Dragon #2 exceeded the radiant heat yield measured by the oblique thermal IR camera. A possible explanation was presented in previous paragraphs related to attenuation of the fire-to-sensor path by tree boles, canopy, atmosphere, and plume.
- Differences between the three deployments in heat yield measured by the thermal IR camera for are related to respective differences in fuel consumption. This relationship, although not quantified for this report, appears to exist; whereas, relationships between the thermal IR and flux package heat yields do not.

Beyond the delivery of this final report, we will analyze and exploit data from other deployments to explore the relationships illustrated in Figure 51.

MODIS (Fire Detection and Mapping—From Pixels to Perimeters

During the timeframe of this project, in a shared development effort with JFSP project 01-1-5-03, perimeter aggregation techniques were investigated. The fires involved were all large fires, comparable in size (and sometimes identical to) the incidents chosen for this project. While the full details are in the final report for project 01-1-5-03, results may be summarized as follows:

1. Satellite fire detections excel at determining the current location of the fire perimeter, but cannot discern the fraction of area within the perimeter which is burned. As shown in Figure 52, gaps are produced when the fire makes a run between MODIS overpasses/observations.
2. A new “burned area” algorithm (developed by Rong Rong Li at NASA, modified and validated by J. Meghan Salmon of the Fire Chemistry Unit, Missoula Fire Sciences Laboratory) excels at discerning burned from unburned area, but is prone to errors of commission. As shown in Figure 53, burned area detections appropriately fill in the gaps in the interior of the Rodeo fire.

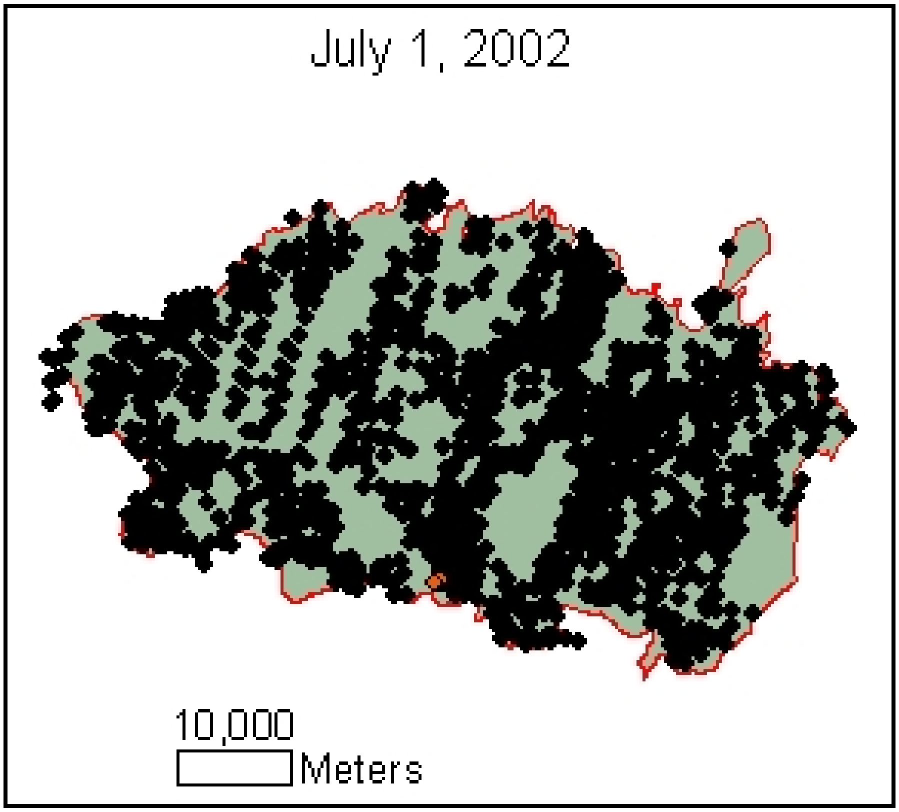

Figure 52. MODIS fire detections over the Rodeo fire (Arizona, 2002).

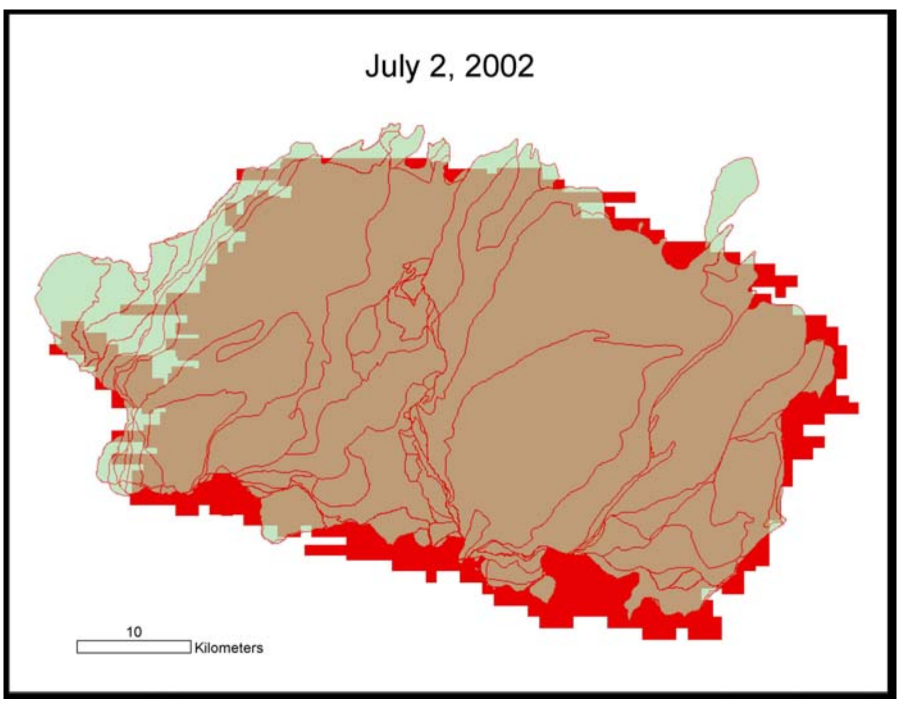

Figure 53. MODIS Burned Area Detections over the Rodeo fire (Arizona, 2002).

3. Perimeters derived from a combination of these two satellite sources provide the most reliable estimate of fire area. Figure 54 illustrates the application of this algorithm to the I-90 fire in Montana, on which the other elements of this rapid response team deployed.

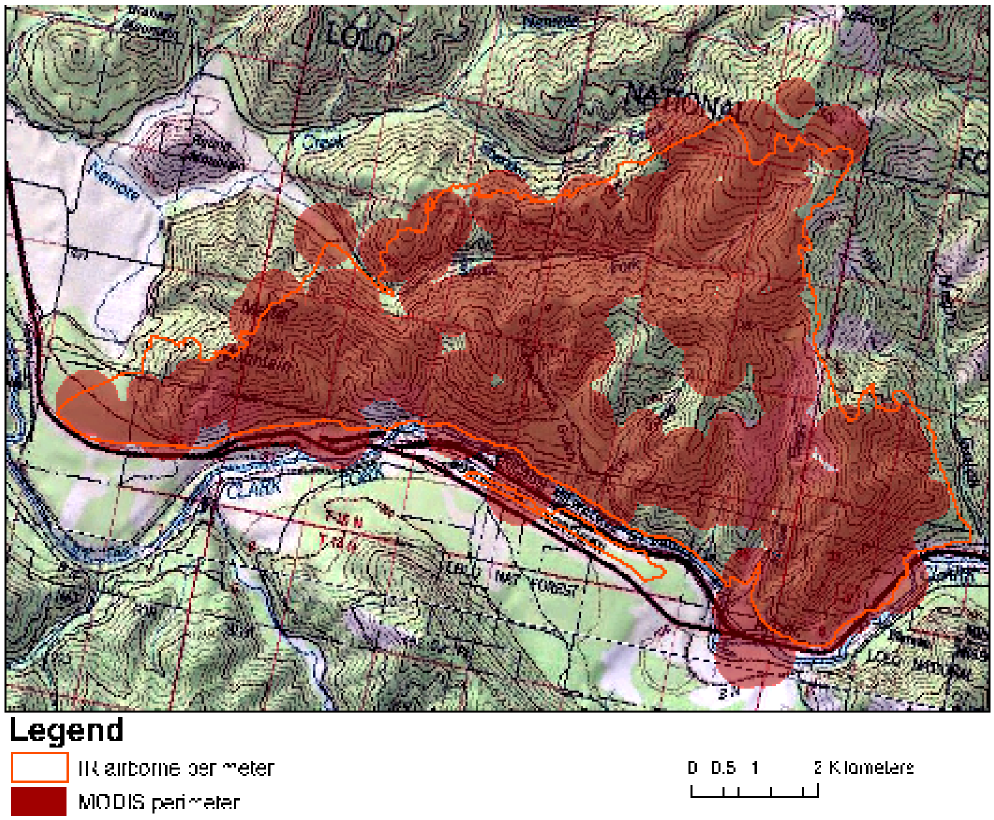

Figure 54. A combination of MODIS Fire and Burned Area Detections produce the most reliable estimate of area burned on the I-90 fire (Montana, 2005.)

FINDINGS AND RECOMMENDATIONS

Site, Vegetation, and Fuels Characterization

Sampling time averaged 45-60 minutes per plot with a crew of three people. This crew size is highly recommended in order to complete the level II or III sampling intensities in this timeframe. Reducing the crew size to two people can greatly increase sample time. The crew leader and one crew member can complete the tree and cover plots and take the photopoints, while the third person completes the fuels plot. The crew leader should collect tree plot data, as data collection procedures can change due to time constraints during sampling. Once all data are collected, all three people can collect fuel moisture samples. This design assumes that there is a fourth person dedicated as the lookout for the crewmembers—the lookout's only job should be watching for snags and other hazards and fire behavior!

Crew training and cohesiveness is of utmost importance in order to complete data collection in a timely, accurate, and safe manner. While every crewmember should be able to perform all tasks, it is best to assign crewmembers to collect either tree or fuel data. This allows for maximum efficiency throughout the field season. Be as systematic as possible while collecting data. This helps ensure that all data are collected in the quickest time. Awareness of the other crewmembers is important and reduces data collection time. For example, the fuels person can hang flagging on a nearby tree to denote the tree plot boundary for the tree crew when establishing the fuel transect.

The FIREMON protocol recommends establishing at least three (and up to seven) fuel transects, installed in a hexagon shape around plot center. Instead, we choose to establish two transects extending from plot center at right angles to each other. This method allowed one person to quickly establish each transect and made relocation easier. We recommend placing at least 3 pin flags along the transect to aid in relocation.

IN SITU AND GROUND-BASED OBLIQUE THERMAL INFRARED RADIOMETRY

Advantages and disadvantages of each measurement method range in terms from operational implementation to the statistical analysis of radiometric data. Although one person can calibrate all instruments simultaneously, two persons each are required to safely install the *in situ* sensors and ground-based TIR cameras on the landscape. Fire behavior packages must be programmed prior to acquisition, but are otherwise autonomous, thereby freeing two additional personnel as resources during the burning period. The TIR cameras, however, are labor intensive, and demand two technical specialists. Encouragingly, the TIR cameras exhibit operational utility by providing real-time information critical to conducting experiments under contingent conditions.

From an experimental design perspective, energy release rates obtained from *in situ* measurements are inherently limited to a point sampling scheme based upon the arrangement of individual instruments within the study area. In contrast, thermal infrared images offer spatially explicit measurements of radiative heat flux, but are inevitably restricted by the viewshed and other non-topographic obstructions. There are several important caveats when using oblique thermal imagery to quantify radiant energy emitted from an area of interest. They are described as follows:

Fire behavior

Combustion of available fuels above the ground plane (i.e. canopy fuels) contributes to the measured radiative energy, but fuel consumption in the canopy cannot be quantified using Brown's planar intersect method. Furthermore, pixels in the thermal image containing torching activity are strictly mapped to a ground location due to the method of georegistration. This mapping error necessarily overestimates the line-of-sight distance between the sensor and the source of radiative emission. These errors of commission can be mitigated (or avoided) by limiting observations of fire behavior to ground and surface fuels. The inclusion of crowning activity in the FRP profile could be mitigated prior to field deployment by selecting a site less conducive to crown fire transition. If images of torching trees interrupt the line-of-site between the sensor and the study plot, then measurements of FRP could be selectively removed from the profile on a per pixel basis. Such exclusions were not attempted during the post-processing of the Dragon or Tripod datasets; these operation appear to be quite labor intensive.

Detection algorithm and background measurement

The limitations and consequences of the detection algorithm developed for the ground-based, oblique thermal IR camera used in this demonstration project should be considered in refining future versions of the deployment and analytical protocols. Methods for quantifying range-dependent absolute threshold should be explored. Since this type of threshold also depends upon the pixel resolution achieved during each unique deployment, a universal method for identifying fire pixels regardless of dynamic range or viewing geometry may be more appropriate. If the instantaneous fire area does not need to be determined, and only measurements of FRP are of interest, then the implementation of a detection algorithm could be avoided by sampling a representative area in the thermal image outside of the fire perimeter to quantify the background contribution. Fire radiative power could then be calculated for all pixels within the study plot. Theoretically the FRP associated with non-fire pixels would be zero, but in reality the FRP of a non-fire pixel is expected to be small enough that it would not significantly impact the spatially integrated value of FRP. This technique obviously relies on the efficacy of using a background outside of the plot to represent the background within the plot, and that a representative number of pixels outside of the study plot are available to be subset.

Area

Relationships between FRE and total fuel consumption must be quantified for the same experimental unit. Here, the study plot has a geographic center from which radiative energy and fuel consumption are measured within a given radius. Calculations of FRP were based upon the area within 11 meters of plot center projected onto the focal plane array. Instead, calculations of FRP could have been performed using the true ground area, or using a different radius to define the boundary of the study plot.

The fractional area projected onto the FPA with respect to the true ground area depends on the viewing geometry (i.e., aspect, slope, and attitude of the sensor). Therefore calculations of FRP using the true ground area associated with each thermal pixel would: (1) correspond to the true ground area sampled during field surveys of fuel consumption; and (2) eliminate viewing geometry as a confounding variable. Retrieval of the true ground area can be accomplished in two ways: first, the projected area could be divided by the cosine of the observation angle; and second, the number of raster elements in the DEM subtended by a single pixel could be summed and simply multiplied the spatial resolution of the DEM. Both methods require georegistration. The former method is strongly sensitive to the observation angle as it approaches a purely oblique perspective at $\angle 90°$, and the second method returns discrete values. Calculating FRP using the true ground area rather than the projected area would yield an increase in the estimate of radiative energy emitted from the plot, and consequently a decrease in the ratio of FRE to total fuel consumption.

A radius of 11 meters (m) was selected to subset the thermal imagery since all categories of fuels were surveyed within this core area. However, transects for coarse woody debris extended to 22 m to ensure an adequate number of fuel particle intersections. The torus between 11 m and 22 m surrounding plot center thus strongly affects the contribution of coarse woody consumption to total estimates of fuel consumption. Furthermore it is the coarse woody debris, together with the duff and litter layers, that dominate glowing and smoldering combustion after the passage of the flaming front. Such toroidal interactions could be examined in the future by subsetting the thermal imagery with an increased radius of 22 m. Finally, although a union method was used when analyzing two adjacent plots within the field of view of the sensor, a convex hull could also be implemented.

Method of calculating FRP

All measurements of FRP relied on the extrapolation of measurements of mid-wave bandpass radiance to hemispherical power emitted over all wavelengths. For a perfectly emitting blackbody, the kinetic temperatures associated with solid and gaseous combustion of biomass (i.e., between 600 and 1000 K) produce peaks in the Plank function that overlap the spectral response function of the mid-wave sensor (i.e., between 5μm and 3μm, respectively). It is the sub-pixel thermal distribution and blackbody assumptions, however, that hinder the true calculation of FRP from an agglomerated brightness temperature. The deployment of a secondary, longwave thermal imaging system offers enhanced spectral coverage and the opportunity to implement split-window algorithms. However, due to differences in optical design bet3ween the two cameras, coeregistration is only possible if camera models have been developed for the optics of the respective cameras. It is therefore suggested that existing methods of calculating FRP be applied, and new methods be investigated. For example both the MIR radiance method and the MODIS MOD 14 semi-empirical approach account for thermal heterogeneity within the pixel. It is recommended that these algorithms be applied to the ground-based thermal imagery, and results compared to that predicted using Stefan Boltzmann's Law. The assumptions and limitations of these methods should also be considered with respect to the spatial context and spectral resolution of the observation.

Signal attenuation and reflection

Prior to irradiance of sensor, interactions occur between the emitted radiation from the fire and the tree stems, crown foliage, and atmosphere (energy-atmosphere and energy-matter interactions). Although boles of trees can catch fire and emit thermal radiation, the cross sectional area calculated by multiplying the diameter at breast height by the length of the stem serves to reduce the ground area exposed to the sensor. Radiative energy emitted by the ground or surface fire directly behind the tree would be absorbed by the bark located on the backside of the tree or otherwise reflected away from the line of sight. Similarly, emitted radiation from outside the plot could be reflected by a bole inside the plot facing the camera, thereby inducing a radiometric signal not associated with combustion within the plot. Although conifer needles also have widths much larger than thermal wavelengths, their number density and spatial distribution within the canopy demands that the attenuation of the thermal signal be described by scattering, absorption, and hence the combined extinction, over the entire path length. Similarly emitted radiation from outside the plot could be scattered into the line of sight by a crown within the study plot thereby inducing a radiometric signal not associated with combustion within the plot. Once the radiation escapes the canopy, however, participating media in the atmosphere have dimensions on the same scale as thermal wavelengths, therefore scattering and absorption efficiencies are best described using Mie theory. Here the composition of the trace gasses, vapors, and particulate matter must be either known or assumed in order to model total extinction in thermal wavelengths. Nevertheless, the interaction between light and matter in a forested environment must be further investigated to quantify errors on measurements of fire radiative power.

Temporal profiles of heat flux sensed at either instrument location are consistent with field observations of a propagating wildland fire. Each profile is unique, and as such must be uniquely interpreted. Artifacts in the data due to extraneous fire behavior, or measurement techniques, must be carefully identified. After which, it is suggested that the following macroscopic features be used to interpret fire behavior at the plot level: (1) the time between an initial heat pulse and the maximum heat flux, (2) the absolute magnitude of the peak in heat flux, (3) the rate and duration of thermal decay, (4) the time-integrated energy density. These metrics can be applied to the temporal profiles of both the *in situ* and ground based TIR imagery, however comparisons between the two measurement methods appear to be vague.

Applications for *in situ* and oblique TIR cameras

The location and attitude of a sensor, as presented in Figure 22, strongly influences the magnitude and direction of incoming energy flux, and hence the potential for estimating first-order fire effects. The placement of the in situ instruments make them most appropriate for (1) measuring the micro-environment within the combustion zone, (2) quantifying the heat flux sensed at a particular differential element of area in space, (3) validating and calibrating fire behavior models, (4) studying pre-heating and ignition of fuel ahead of the fire front, and (5) relating heat flux to bole damage & tree mortality. In contrast, ground-based TIR cameras are more appropriate for (1) measuring the entire radiative energy emitted from combustion zone, (2) estimating fuel consumption and smoke production, (3) quantifying the profile of the heat pulse input into the soil, and (4) mapping fire spread rate and pattern. Though coupling the *in situ* measurements with the TIR images offers the most complete characterization of a wildland fire, the objectives of an experiment will in part determine the method best suited for the measurement.

AIRBORNE THERMAL IMAGERY—LESSONS LEARNED AND FUTURE WORK

A comprehensive discussion of the details relating to the airborne thermal imagery acquired by the PSW airborne FireMapper platform are provided under separate cover by Dr. Phillip Riggan. However, several questions were formulated on the basis of our independent exploratory analyses of imagery from the Cooney Ridge incident:

- Can ground-based thermal infrared images in a mid-wave infrared wavelength be used to validate or enhance airborne thermal infrared imagery acquired in the long-wave infrared bandpass?

- How does the timing of the image acquisition affect the ultimate temperature values?
- How does distance from the heat source affect the ultimate temperature values?
- How does angle of acquisition affect the ultimate temperature values?
- How does pixel resolution affect the ultimate temperature values?
- How does projecting an oblique image into an orthographic projection affect the ultimate temperature values?
- Can thermal imagery be used to determine fuel consumption?

MODIS Fire Detection and Mapping—Lessons Learned

The inclusion of an inflexible satellite schedule into a rapid response program can benefit from several lessons learned during this project.

1. If a polar orbiter is to participate in a multi-scale investigation, its schedule and characteristics need to drive the other components.
    a. As a rule of thumb, the collection of good data over a fixed site at a low nadir angle will only occur every other day. This gives the rapid response team a "planning cycle" on the day prior to collection.
    b. Safety concerns, current and expected fire behavior, and site access could be used during the planning cycle to identify promising deployment sites for the following day.
2. The ground-based thermal imager needs to operate continuously between the time the in-situ instruments are burned over and the time of the satellite observation. All pains should be taken to minimize this interval.
3. The aircraft data is compared with the high-resolution ground imager and coarse MODIS imagery. As such, it is best used to capture a thermal image of a large area (which includes the small area observed by the ground imager) simultaneous with the satellite overpass.
4. To maximize chances of success, experiments such as this one should be conceived as a chain of instruments. Each link in the chain must bridge the gap between the spatio-temporal coverage of the adjacent links. The ground imager bridges the gap between in-situ measurement and aircraft measurements as the aircraft bridges the gap between the ground imager and the satellite. Each link should have a set of simultaneous measurements of the same phenomena.

LITERATURE CITED

Andrews, P. L. (1986). Behave: fire behavior prediction system and fuel modeling system-burn subsystem, part 1. USDA For. Ser. Gen. Tech. Rep. INT-194.

Brown, J.K., Oberheu, R.D., and Johnston, C.M. 1982. Handbook for inventorying surface fuels and biomass in the interior west. Gen. Tech. Rep. INT-129, U.S. Department of Agriculture, Forest Service, Intermountain Forest and Range Experiment Station, Odgen, UT.

Butler, B. W., J. Cohen, D. J. Latham, R. D. Schuette, P. Sopko, K. S. Shannon, D. Jimenez, and L. S. Bradshaw (2004). Measurements of radiant emissive power and temperatures in crown fires. *Can. J. For. Res.* 34: 1577-1587.

Dietenberger, M. (1999). Effect of backing board on the heat release rate of wood. Product Safety Corporation. International Conference on Fire Safety, Columbus, OH. Product Safety Corporation, Sissonville, WV. 28:62-73.

Finney, M. A. (1998). FARSITE: Fire Area Simulator – model development and evaluation. USDA Forest Service, Res. Pap. RM-RP-4. Rocky Mountain Research Station, Ogden, UT. 47 pp.

Freeborn, P. H., B. L. Nordgren, W. M. Hao, R. H. Wakimoto, and L. P. Queen (2004). Ground-based thermal observations of the Black Mountain 2 Fire in west-central Montana, 2003. Proceedings of the Tenth Forest Service Remote Sensing Applications Conference, edited by J. D. Greer, Salt Lake City, UT, 5-9 April.

Incropera, F. P., and DeWitt, D. P.1996. *Fundamentals of Heat and Mass Transfer*, fourth edition. John Wiley & Sons, New York. 886 pp.

Kaufman, Y. J., C. O. Justice, L. P. Flynn, J. D. Kendall, E. M. Prins, L. Giglio, L., D. E. Ward, W. P. Menzel, and A. W. Setzer (1998). Potential global fire monitoring from EOS-MODIS. *J. Geophys. Res., 103*(D24), 32215-32238.

Lutes, D.C., Keane, R.E., Caratti, J.F., Key, C.H., Benson, N.C., Sutherland, S., and Gangi, L.J. 2006. FIREMON: The fire effects monitoring and inventory system. Gen. Tech. Rep. RMRS-GTR-164-CD, U.S. Department of Agriculture, Forest Service, Rocky Mountain Research Station, Fort Collins, CO.

Robinson, J. M. (1991). Fire from space: global evaluation using infrared remote sensing. *International Journal of Remote Sensing*. 12(1):3-24.

Urbas, J., and W.J. Parker (1993). Surface temperature measurements on burning wood specimens in the cone calorimeter and the effect of grain orientation. *Fire and Materials*. 17:205-208.

Wooster, M. J., B Zhukov, and D. Oertel (2003). Fire radiative energy for quantitative study of biomass burning from the BIRD experimental satellite and comparison to MODIS fire products, *Remote Sens. Environ., 86*, 83-107.

APPENDICES

A—Project Deliverables Cross-Walk Table

B—Operations Plan for Field Campaigns

C—Job Hazard Analysis for Field Campaigns

D—Cover and Contents List from *Dragon WFU Rapid Response Closeout Package*

E—Grand Canyon News Release: "*Fire Research Scientists Use Dragon Fire for Experiments,*" *By Tom Schafer, Fire Information Officer*

F—Example "Orders of the Day" for Rapid Response Team—Dragon WFU

G—Photo Gallery

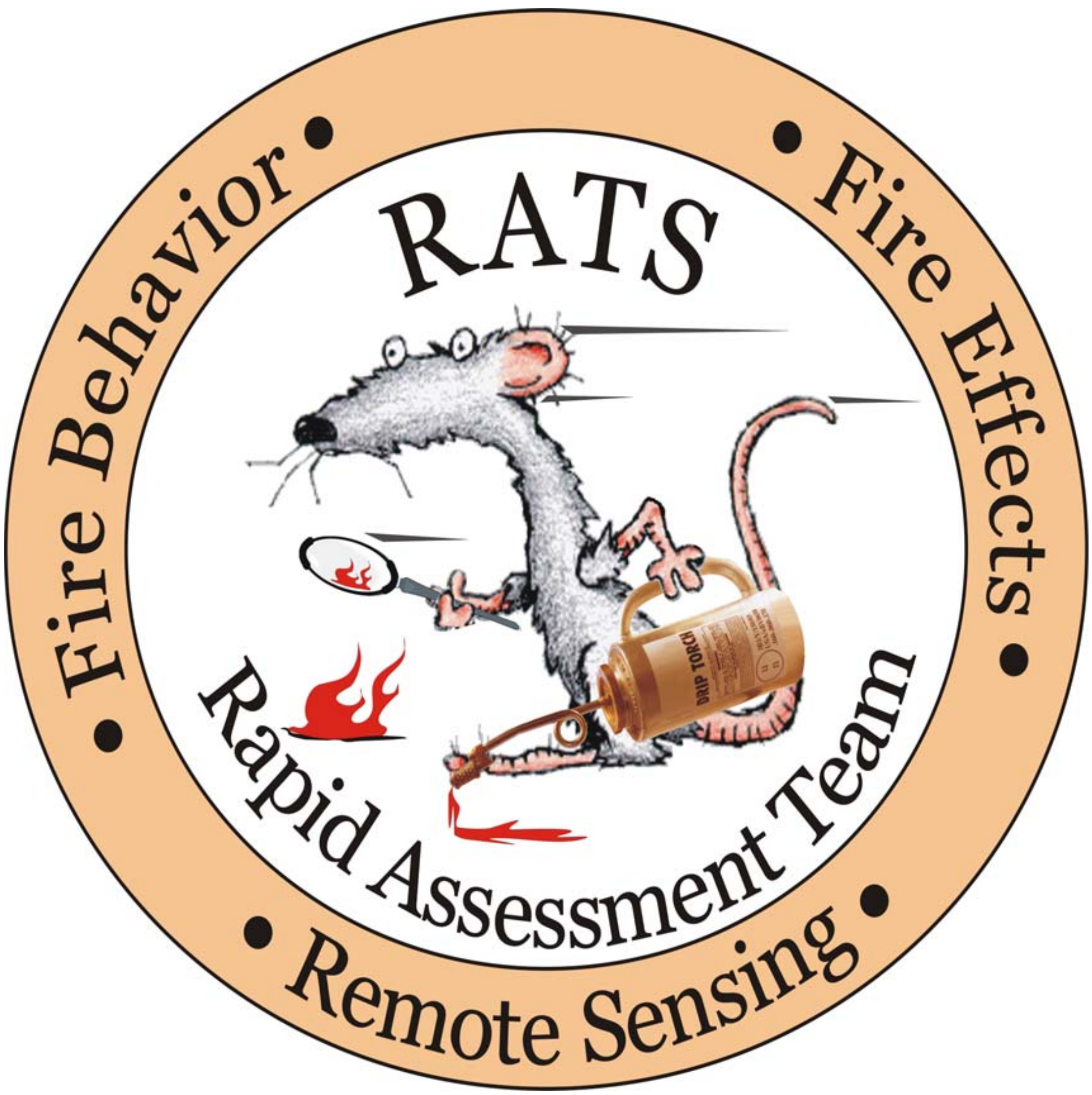

Appendix A

Project Deliverables Cross-Walk Table

Appendix B

Operations Plan for Field Campaigns

Appendix C

Job Hazard Analysis for Field Campaigns

Appendix D

Cover and Contents List:

Dragon WFU Rapid Response Closeout Package

Appendix E

Grand Canyon News Release:

"Fire Research Scientists Use Dragon Fire for Experiments"

By Tom Schafer, Fire Information Officer

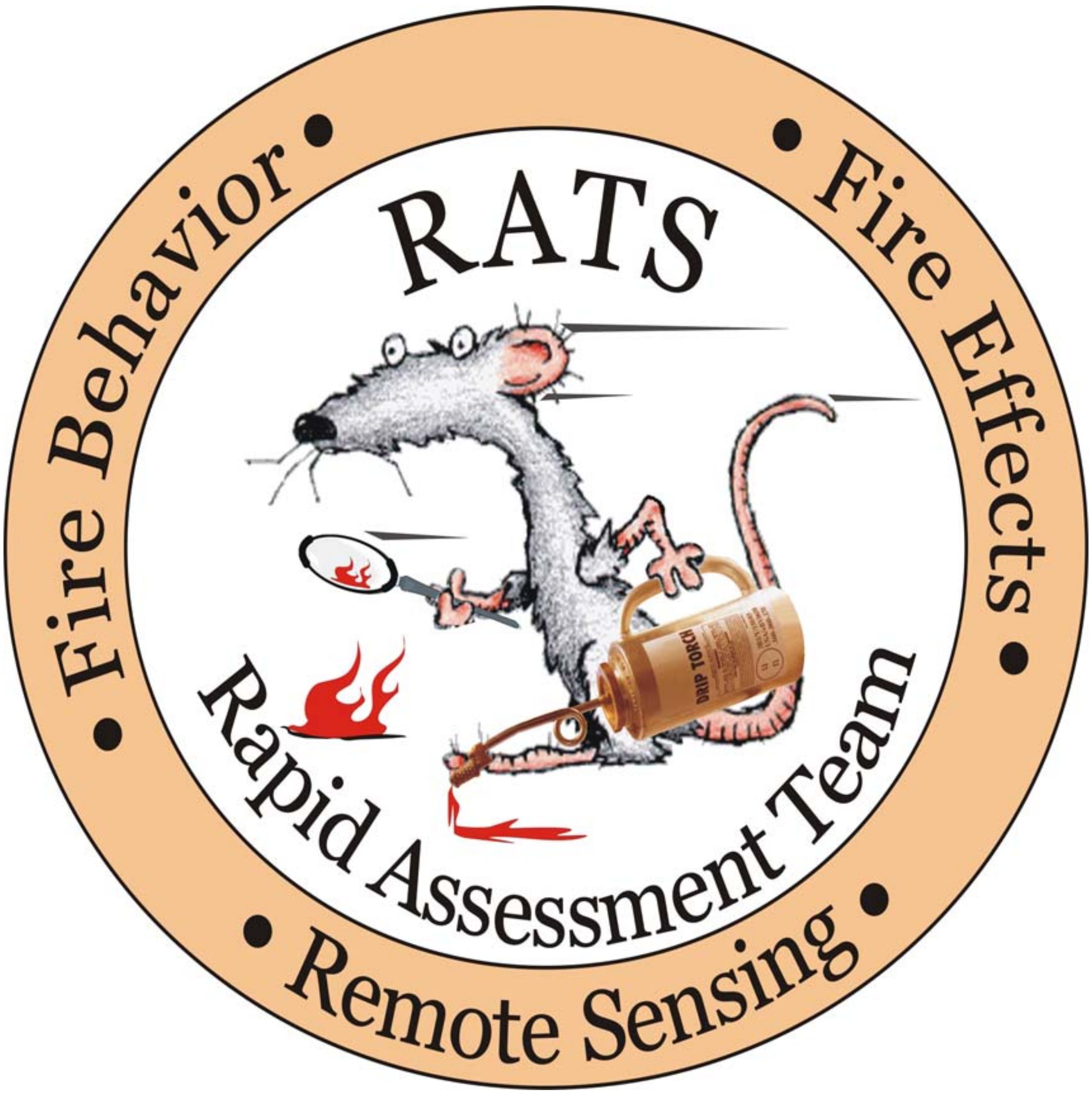

Appendix F

Example "Orders of the Day"

Rapid Response Team—Dragon WFU

Appendix G

Photo gallery